The Topography of '660'km Discontinuity Beneath Kurile and Izu-Bonin Regions

ハオ, ガン

The Topography of '660'km Discontinuity Beneath Kurile and Izu-Bonin Regions

Department of Earth and Planetary Science

Graduate School of Science

Kyushu University

Hao Gang

February,2021

Contents

1 Abstract

According to the 1-D seismic velocity model, both P and S velocity suddenly increase at the depths of 410 and 660 km in the upper mantle, called the 410 and 660 km discontinuities. The latter one is recognized to be the boundary of the post-spinel phase transition that occurs in the mantle. The Northwest Pacific subduction region is an ideal place to study the topography of the 660 km discontinuity as the cold lithosphere subducts into the hot mantle and generates a lateral cold temperature anomaly which gives rise to a depth variation of the phase boundary of post-spinel transformation with negative Clapeyron slope. In this study short-period ($\sim$1s) seismic data from North America, Europe, South Asia and Australia seismic networks are analyzed in order to investigate the near-source side 'S660P' conversion phase which starts as a down going S wave, partially converts to a down-going P wave at the '660 km discontinuity' beneath the source and arrives up to $\sim$60s after the direct P wave for intermediate-depth and deep earthquakes in the Kuril-Kamchatka to Sea of Okhotsk subduction zone and Izu-Bonin subduction zone. Seismic tomography showed that the Pacific slab stagnates on the 660km discontinuity in Southern Kuril. According to the results of our study, the 660 km discontinuity has descended to about 675 km depth beneath the deepest earthquakes. This boundary topography corresponds to a $-300\,^{\circ}$C temperature anomaly in the vicinity of the slab if the Clapeyron slope of the post spinel transformation is assumed to be -2.5 MPa/K. For Northern Kuril, tomographic models suggest that the slab passes through the 660 km discontinuity and penetrates into the lower mantle. Our observation showed that the discontinuity depressed to about 690 km depth directly under the deepest events with the width of the depression about 150km. For a Clapeyron slope of -2.5 MPa/K, the corresponding temperature anomaly near the center of the slab is $-600\,^{\circ}$C. Observations for the Izu-Bonin region showed that the 660 discontinuity descended to about 685 and 690 km depths at $\sim$ 100 to 200km away from the deepest events towards the trench-ward direction in the northern and southern parts, respectively. For a Clapeyron slope of -2.5 MPa/K, the result suggests
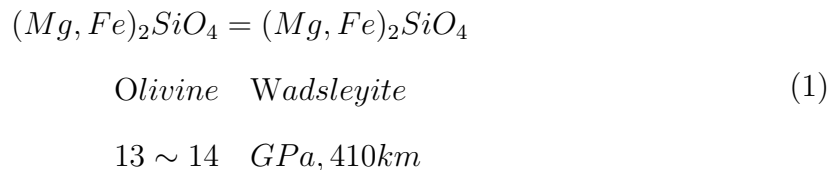
a temperature anomaly of $500\,°C$ to $600\,°C$ in the vicinity of the slab. Observations for shallower earthquakes in both regions showed that the 660 km discontinuity rises about 10~20km in ordinary mantle away from the slab by ~ 500km in the trench-ward direction .
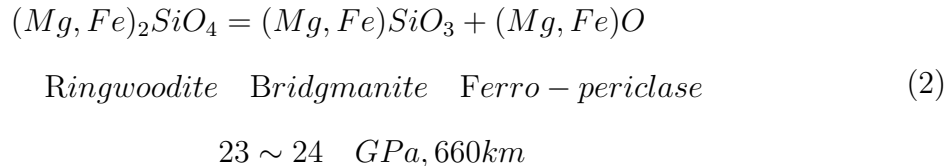
2 Introduction

2.1 Discontinuities and Phase Transitions in the Upper Mantle

The global one-dimensional seismic models such as PREM (Dziewonski & Anderson, 1981); IASP91 (B. Kennett & Engdahl, 1991) and AK135 (B. L. Kennett, Engdahl, & Buland, 1995) reveal the features of seismic wave velocities that relate to the mineralogical and chemical structure in the earth's interior. Figure 1 shows that there are two main discontinuities in the upper mantle at the depths near 410 and 660 km. Seismological approaches include the use of SH-polarized mantle reverberations (Revenaugh & Jordan, 1987) (Revenaugh & Jordan, 1989) and the stacking of global long-period data (Shearer, 1990), which are used to investigate the characteristics of the discontinuities. As going deeper, seismic wave velocities increase almost monotonically with depth until near the core-mantle boundary. (Lay, Williams, & Garnero, 1998) summarize the reports of the presence of the D" layer in many areas, with a ∼1.5 to 3% velocity discontinuities for both compression and shear waves at the depth of 150 to 300 km above the CMB. Plausible explanations about the origin of the upper mantle discontinuities (at 410 km and 660 km depths) are that they arise from pressure-induced solid-solid phase transformations in the peridotitic mantle rocks.

Earlier high-pressure experiments in the 1960 s (Ringwood & Major, 1966) and subsequent studies in 1980s (Ito & Takahashi, 1989) ; (Katsura & Ito, 1989) ; (Wood, 1989) showed that as the pressure increases, a series of phase transitions occur at the olivine component of peridotite as shown in equations (1) and (2).

$$(Mg, Fe)_2 SiO_4 = (Mg, Fe)_2 SiO_4$$
$$\text{O}livine \quad \text{W}adsleyite \tag{1}$$
$$13 \sim 14 \quad GPa, 410km$$

$$(Mg,Fe)_2SiO_4 = (Mg,Fe)SiO_3 + (Mg,Fe)O$$

$$\text{R}ingwoodite \quad \text{B}ridgmanite \quad \text{F}erro-periclase \tag{2}$$

$$23 \sim 24 \quad GPa, 660km$$

Olivine transforms to Wadsleyite, $(Mg,Fe)_2SiO_4$, at the pressure of about 13.5GPa, and the post-spinel transition occurs at the pressure of $\sim$23 to 24 GPa where ringwoodite ultimately breaks down to form perovskite, $(Mg,Fe)SiO_3$ (called bridgmanite), plus wustite, (Mg,Fe)O. These transformations are sensitive to both mantle composition and temperature (Bina & Helffrich, 1994) which clearly correlate with two major global upper mantle seismic discontinuities and delineate the mantle transition zone (MTZ).that arise from solid-solid phase transitions in the mineral olivine. The exothermic transformation of olivine to wadsleyite occurs at the depth near 410km and generates the 410km discontinuity, whereas the endothermic transformation of ringwoodite to bridgmanite occurs at the depth near 660km and forms the 660km discontinuity.

2.2 Depth Perturbation of Upper Mantle Discontinuities

As the phase boundaries are both sensitive to mantle temperature and composition, their depths are perturbated by lateral changes in thermal properties nearby the subducting slab where the colder lithosphere material descends into hotter mantle. The change in the discontinuities' depths are determined by the Clapeyron slope of the phase transitions which are defined as dP/dT. It indicates that the phase transition boundary changes in pressure or equivalent to depth for a given change in temperature. The 410 km discontinuity becomes shallower for a cold mantle anomaly as the positive Clapeyron slope of the corresponding phase change, while at the 660 km discontinuity, the discontinuity depth should be larger inside or around the subducting slab due to the negative Clapeyron slope of the post spinel transformation. These changes in depth determined by the value of the slope, as a result, cause a thicker MTZ (i.e., the 410 km discontinuity becomes shallower while the 660 discontinuity deeper) around subduct-

ing slab with lower temperature anomalies, or thinner MTZ (the 410 km discontinuity becomes deeper while the 660 km discontinuity shallower) near the mantle plume with higher temperature anomalies (Houser & Williams, 2010).

Quantitative studies of the Clapeyron slope have been conducted mainly through three kinds of approaches: high-pressure high-temperature experiment (Hirose, 2002) (Ghosh et al., 2013); thermodynamic calcuration (Bina & Helffrich, 1994); and the first principle calculation. The reported range of the Clapeyron slope of the post-spinel transition is large as shown in the Figure 2: -3.0 MPa/K (Ito & Takahashi, 1989) (Irifune et al., 1998), -2.0 to -0.4 MPa/K (Katsura et al., 2004), -1.3 MPa/K (Fei et al., 2004), -0.8 to -0.2 MPa/K (K. D. Litasov, Ohtani, Sano, Suzuki, & Funakoshi, 2005a) (K. Litasov, Ohtani, Sano, Suzuki, & Funakoshi, 2005b). These studies proposed various results inconsistent with each other. However, the distribution of the post-spinel transition Clapeyron slope is concentrated in the interval of -2.5 to -3.0 MPa/K. As the changes in pressure with depth in the earth interior is well understood, for example, at the coldest core of subducting slab with a temperature anomaly about 500 K usually inferred from geodynamic models (Simmons, Forte, & Grand, 2009), the temperature anomaly can be translated to 30km change in depth for the Clapeyron slope value of -2.5M Pa/K.

2.3 Previous Studies

Seismological approaches play an important role of obtaining the characteristics of mantle discontinuities. They include several purposes such as discovering their existence, determining whether they are global or local in extent, observing their topography, and quantifying their sharpness and jump in both P and S velocity (BINA, 1991). (Shearer, 1990) (Shearer & Masters, 1992) (Shearer, 1993) revealed the global presence of 410, 520 and 660km discontinuities and measured their global and regional topography by stacking the long-period ($\sim$25s) underside surface reflection phases PP/SS and their precursors PdP/SdS. (Flanagan & Shearer, 1998) and (Shearer & Flanagan,

1999) revealed that the 660km discontinuity have a jump in velocity between 4% to 6% . The SdS data revealed that the 660 discontinuity is located around the average depth of 655~660 km at worldwide scale, while the observed depth variations are up to 40km suggesting a correlation between regional depressions of the 660km discontinuity and the subduction zones specifically at Northwest Pacific. The most clearly coverage of long-period data at the Northwest Pacific showed a depression about 15 degree (~1700km) wide and with a depth variation up to 20km beneath the Kurile-Kamchatka subduction zone. The depression corresponds to a 200 to 400K temperature anomaly if the Clapeyron slope ranges from -2 to -4 MPa/K, which is the range proposed by laboratory measurements mentioned above. More recent global mapping of the 410 and 660km discontinuity topography and the transition zone thickness using SS precursors (Houser, Masters, Shearer, & Laske, 2008) (Houser & Williams, 2010) proved the topographies of the 410 and 660 km discontinuities are anti-correlated due consistent with the opposite signs of their Clapeyron slopes at the phase transition boundaries. Houser (Houser, 2016) showed that the 660 km discontinuity is depressed at Philippine Sea and is raised near South Kurile with the amplitude about 20 km and 10km, respectively, whereas the 410 km discontinuity is depressed at the Pacific regions where the mantle is warmer than average.

Even though analyzing globally recorded long-period PP/SS precursors is in favor of mapping the discontinuities in large scale, regional short-period seismic arrays comprising hundreds of instruments have advantages in revealing small-scale (~100km) structure and supplements the long-period results that is insufficient in understanding the properties of the upper mantle discontinuities due to their poor spatial resolution (~1000km). In the 1980s, Barley, Hudson, and Douglas (Barley et al., 1982) and Bock and Ha (Bock & Ha, 1984) found some unknown phases (called the 'X' phase) with an arrival time later than direct P waves about 25 to 30 s for the Izu-Bonin subduction zone and 20 to 50 s for the Tonga subduction zone by using the earthquakes occurred in these regions and short-period seismic data recorded by Warramunga Seismic Array (WRA), which is the short-period small-scale (less than 30 instruments) in Australia.

The X phase is not predicted by any standard global seismic models and has a similar ray-path to P, with a slowness slightly smaller than direct P wave. It was interpreted as a S-to-P conversion at a discontinuity below the hypocenters at the source side in the subduction zone at these regions.

In a more recent study about the S-to-P conversion (Collier, Helffrich, & Wood, 2001), short-period regional seismic networks located in UK (United Kingdom network) and US (UW: University of Washington network) are used to observe the topography of discontinuities beneath Northwest Pacific. These arrays have a larger aperture and more receivers than WRA. Earthquakes that occurred in Kurile, Japan and Izu-Bonin excited down-going S waves which were conversed to P waves at the specific interface, are used to obtain the depth of discontinuities in the vicinity of the sources. The data coverage in Izu-Bonin is denser than Kurile, showing that the 660km discontinuity depressed 50~60km under the deepest events. Wicks and Richards (Wicks & Richards, 1993) analyzed 73 earthquakes that occurred at the Izu-Bonin region with hypocentral depths between 250 and 550km. They used data recorded by WRA array in Australia. They claim that 660 km discontinuity is found to be depressed by 40 to 50km beneath the coldest central part of slab, suggesting a 1000±200 ℃ low temperature abnormal which consistent with a Clapeyron slope with value of -2.8 MPa/K. However, the conversion points they detected are apparently not located in the "coldest portion" of the the Pacific slab according to the recent tompgraphy studies (Fukao & Obayashi, 2013) and the shape of the Wadati Benioff zone in (Okino, Ando, Kaneshima, & Hirahara, 1989) . Therefore their inerence is questionable. Wicks and Richards (Wicks & Richards, 1993) also analyzed 65 deep earthquakes at Izu-Bonin and adjacent areas recorded by arrays in Germany, West US, India and Turkmenistan to identify the 660 km discontinuity by using the near-source S-to-P conversion. They suggested that the 660km discontinuity may be depressed beneath the deepest earthquakes up to a depth of 740km. For a Clapeyron slope of of post spinel transformation of -2.8 MPa/K, this depression means a maximum temperature difference of ~1100 K between coldest part of slab and surrounding mantle. Such a cold temperature anomaly seems unrealistic

given the plausible thermal structure of the subducted Pacific slab, so that the properties of the 660 km disconinity in relation to the post spinel transformation remain enigmatic.

2.4   Purpose of Our Research

A subduction zone is an ideal place to investigate regional topography of the 660km discontinuity as the slab generates a lateral temperature anomaly and causes a change in the discontinuity depth. Among the circum Pacific subduction zones Izu-Bonin, Mariana and Tonga-Fiji are better investigated by using regional short-period approaches than Kurile, for which the behaviour of the 660 km discontinuity associated with the Pacific slab has not been clearly imaged by a previous study by (Collier et al., 2001). This is mainly because the deep seismicity at the subduction zone is not very high. Therefore we analyzed hundreds of events that occurred in Kurile during more than 30 years from 1980s to 2020s in order to supplement the information about regional fine-scale topography of the 660 beneath Kurile. In addition, we collected newer data for the Izu-Bonin region, which has become available owing to the progress in the deployment of high quality broadband seismic networs in the US and Europe since about 2000, and attempt to compare to results in the perevous studies before 2000s. Previous researches about short period S-to-P conversion mentioned above mainly used deep earthquake with focal depths between about 300 to 500km but rarely included intermediate depth earthquakes with a shallower focal depth from about 100 to 200km. Therefore, our dataset not only includes the deeper events which are in favor of obtaining information about the discontinuity straight beneath the slab, but also includes a certain number of intermediate depth events that have the ability of exploring the topography of the 660km discontinuity away from the slab toward seaside.
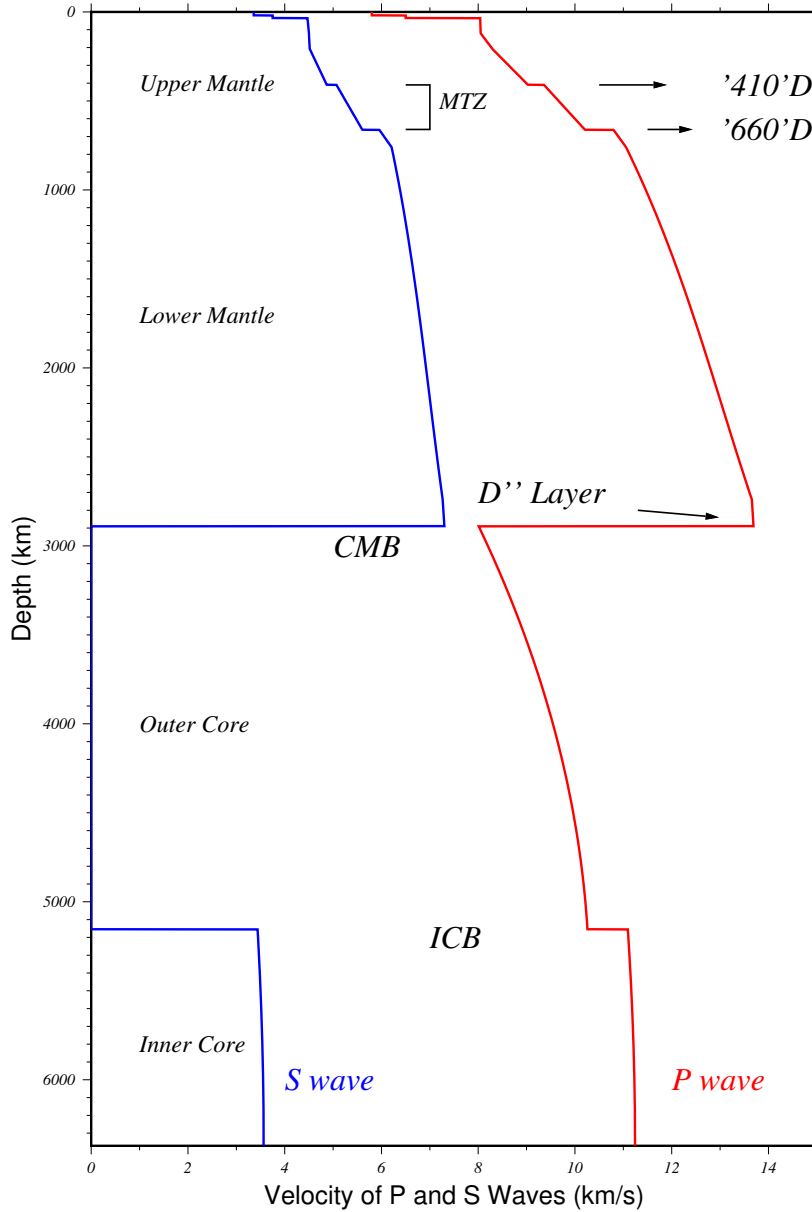
Figure 1: The seismic wave velocity model: IASP91 [Kennett and Engdahl,1991] shows the two main discontinuities in the upper mantle at the depth of 410 and 660km which sketch the range of the mantle transition zone (MTZ). As going deeper, the DD' layer with a $1.5 \sim 3$ % velocity discontinuities 150~300km above the CMB.
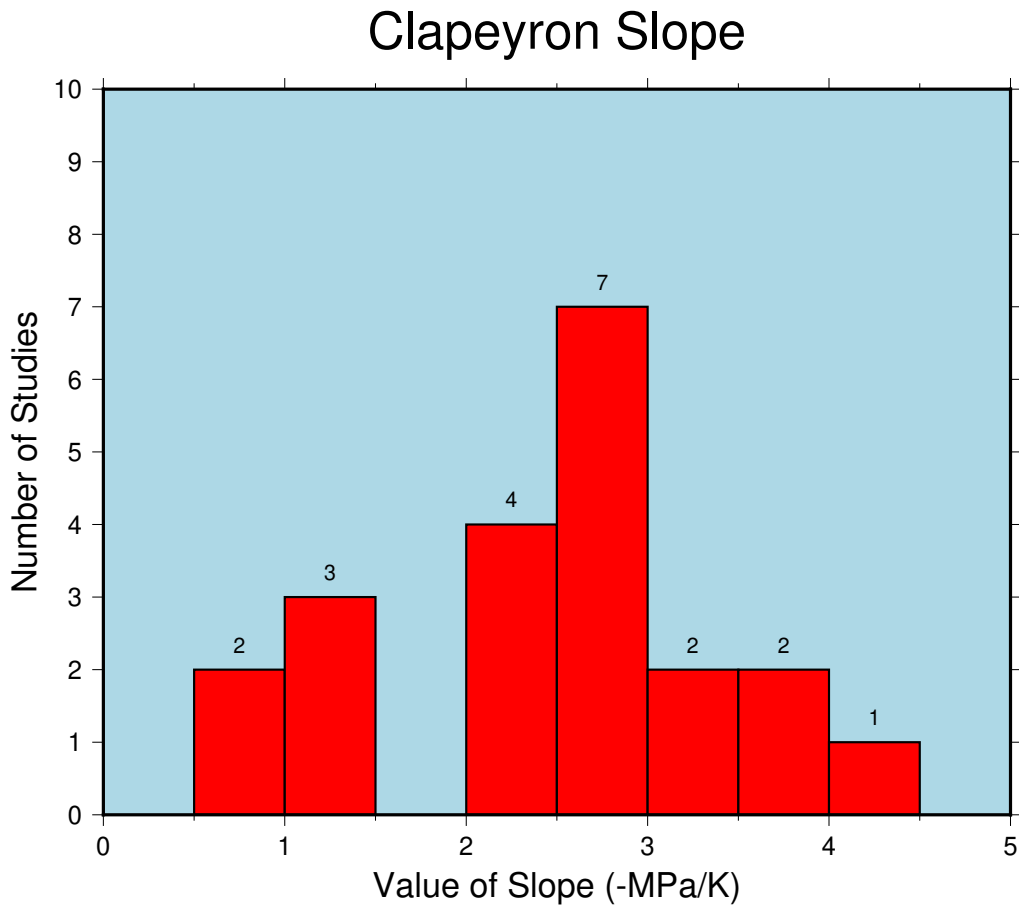
Figure 2: Values of Clapeyron slope obtained by previous works mainly include three approaches: high-temperature high-pressure experiment; thermodynamics and first-principle calculations. The distribution of the previous results shows that the most reasonable values of the Clapeyron slope within the interval from 2.5∼3 MPa/K.

3 Data and Methodology

3.1 Seismic Data and Arrays

We analyzed a total of over 200 intermediate and deep events whose focal depths are within a range from 100 to 650km with magnitudes higher than Mw 5.6, which occurred in the Kuril-Kamchatka and Izu-Bonin subduction zones since 1984 (Table 1, 2) and were recorded by worldwide seismic networks. We investigate the topography of the 660km discontinuity beneath the earthquakes. Events shallower than 50km are not included in the data set as their records usually have powerful near-surface reverberation at the mantle above the sources leading to low signal-to-noise ratios for investigating the S660P phases. Both short-period and broad-band channel's data are used in our study. Broad-band channel data are mainly of the following arrays: AK (Alaska regional network); BK (Berkeley digital seismic Network BDSN); CI (Southern California seismic Network); US-Array (Regional and TA); GR (German regional seismic Network); GEOFON projects (GFZ, Potsdam); TSAR (Thai Seismic Array Project,2015 2017). Short-period data from UW array (Pacific Northwest Seismic network, University of Washington) are also included.

Data of these arrays are available from the data center of Incorporated Research Institutions for Seismology (IRIS). The number of broad-band stations in Europe and Alaska increased gradually since 2000 and is on the order of 50 to 70 broad-band before 2005, while the AK Network expanded and became denser after 2010, containing a few hundred stations distributed throughout Alaska region. US Array (TA) is a transportable network of ~400 broad-band seismographs, which migrated from west to east in the United States. Since the broad-band network had poor coverage in the 1980s and 1990s, short-period data mainly from UW array are used in our study as additional, which composed of ~140 stations from 1982 to 1996.

Figure 3 shows the locations of the sources and networks used in our study. Few S660P phases were observed through all networks in Australia region, which may be due to sparsely distributed stations across the overall continent. Studies of scattering waves

from a scatterer tend to be coherently observed at relatively small array (∼1000km across) (Kaneshima, 2016) (Kaneshima, 2019), which may be the case for short period S660P, too . Therefore, in the case of a large network such as US Array (TA); Southern California (BK & CI) array and network in Alaska region (not only AK array, but also combine with US Regional Networks), we divided them into smaller parts that do not overlap with each other, with an aperture about 8 degrees typically consisting of 100 to 200 stations. Smaller arrays that are not larger than 10 degrees such as UW array, network in German and Thai are not divided. The aperture and amount of channels should not be reduced in order to gain a high enough quality of stack and high enough resolution of slowness (0.05∼0.1s/deg), which enable to determine the topography of the 660 km discontinuity as fine as possible.

Figure 4 shows schematic picture of the source-side geometry, earthquakes with depths that can vary in a range from 100 to 650 km, and receivers that can be located at both trench ward (to European array) and sea ward (to Alaska and US array). Upgoing underside reflected (pP) and down-going refracted phases(S660P) are shown in the figure. The ray path of refracted phases which are directed to Europe are almost within the slab while those directed to Alaska and US leave away from the slab and interact with the discontinuity at "ordinary" mantle, which means that a significantly cold subducting or hot upwelling material do not exist unless directly beneath the slab. As the focal depth becomes shallower, the S-to-P conversion point gradually departs from the slab. Therefore, it is possible to investigate the 660-km discontinuity not only directly beneath but also away from the Kurile-Okhotsk subduction zone both at trench-ward and ocean-ward direction.

For events that occurred in the Kurile-Okhotsk region, the epicentral distances are about 72 to 78° to Europe, ∼30 to 40° to Alaska, ∼56 to 86° to the arrays located in the US, ∼55° to Thailand, and ∼75° to Australia. On the other hand, for earthquakes in the Izu-Bonin region, those recorded by the arrays in the Western US and Alaska the typical epicental distances are about 80°, whereas those recorded by the European seismic networks are at distances between ∼75 and 90°. Arrays are chosen to have a

distance basically no more than 95 degrees since signal-to-noise ratio of P coda will be significantly decreased because diffracted waves arrive there. Figure 5 shows the hypocenters of earthquakes with magnitude higher than Mw=5.5 for the Kurile and Izu-Bonin regions. Shallower events with focal depth less than 150km are represented by yellow and green solid circles, whih are generally located near the Kamchatka and Izu-Bonin trenches. On the other hand, as the subducting Pacific Plate descends deeper toward Eurasian and as Phillippine Plate toward west, the focal depths of the events associated with the subductions also increase up to 500 to 600km as expressed in blue pink and red circles. Histograms in Figure 6 show the distribution of focal depth in respective regions. By comparing the distributions of the two regions, we can find that the Kurile region has more events with a depth between 100 and 150km, which are favorable to study the topography of the 660km discontinuity away from the slab, whereas Izu-Bonin has more deeper ones with depts between 300 and 600km.

We selected the records for which with relatively high signal-to-noise ratio arrivals of direct P wave can be seen clearly. We pick the P arrival as reference for travel time and waveform alignment. Short-period data are filtered with a band-pass filter with a corner frequencies 0.2 Hz and 1.5 Hz while broad-band data are band-pass filtered between 0.1 and 2.0 Hz since the nature of waveform are not changed too much by the filtering.

3.2 Investigates the '660' Discontinuity by using S-to-P Conversion

(Barley et al., 1982) and (Bock & Ha, 1984) as mentioned in the previous chapter found some unknown phases (has been called the 'X' phase) with arrival-times later than direct P waves by about 25 to 30 s for the Izu-Bonin subduction zone by using the earthquakes in these regions and short-period data recorded by WRA. The X phase is adequately interpreted as a S-to-P conversion at the source side in the Izu-Bonin subduction zone.
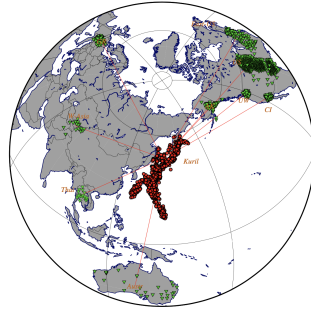
(a)
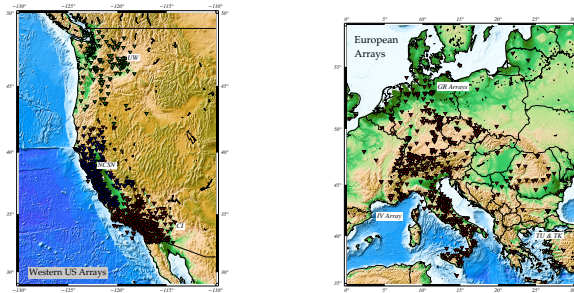
(b)
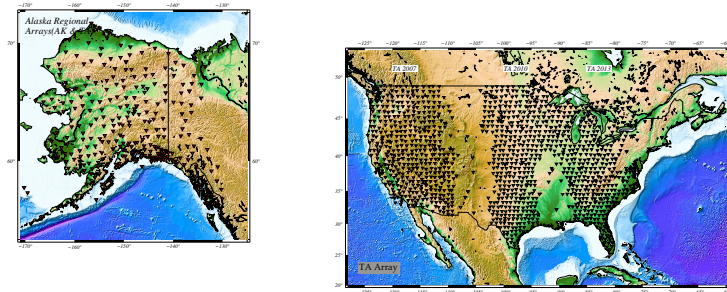
(c)

Figure 3: (a)The earthquakes and arrays are represented by red circles and green triangles respectively. The red lines show the typically great circle path between event and receivers in our study. (b)Details of the receivers in the arrays located on the west coast of the United States (left) which include the UW, BK, CI, NCSN and those in Europe (right) generally include arrays in German and Italy and Turkey. (c)Details of AK and TA arrays.
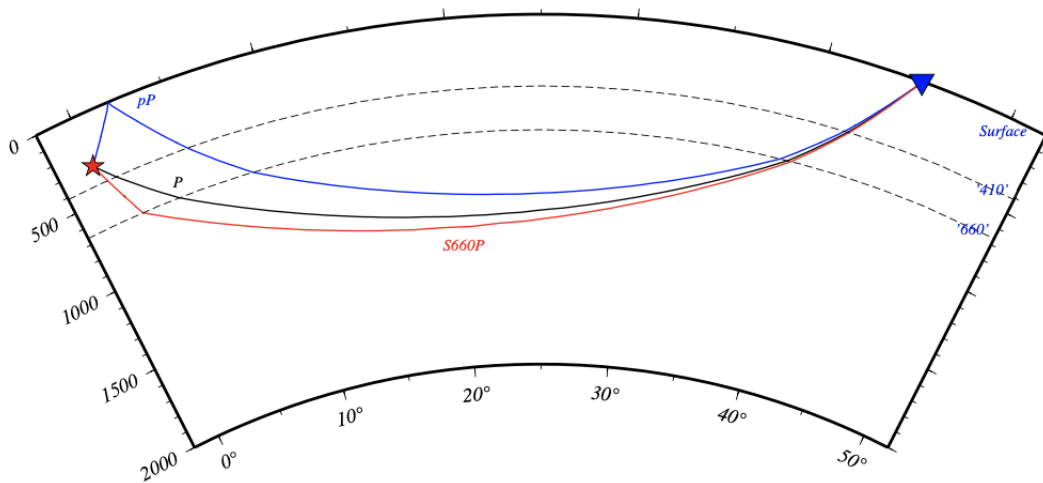
Figure 4: Ray-path of P, pP, S660P in the mantle. Difference between the black and red one is from source to 660km discontinuity and approximately same from discontinuity to receiver.

For the Kuril-Okhotsk region our purpose is to investigate the structure of the 660 km discontinuity by using the events that occur in subducting slab and compare with the results from the previous studies of long period SS precursors. Although the long period SS precursors are ideal tools for investigating large scale topography of the 660 discontinuity (Shearer, 1991) (Shearer, 1993) (Shearer & Masters, 1992) (Houser & Williams, 2010), regional scale structure for the Kuril-Okhotsk subduction zone is too fine for the SS precursor technique to distinguish for its spatial resolution (Houser et al., 2008) (Helffrich, 2000). On the other hand the receiver function method that also has been used for investigating the detail of the 660 discontinuity (Gurrola, Minster, & Owens, 1994) (Shen, Solomon, Bjarnason, & Wolfe, 1998) (Niu, Levander, Ham, & Obayashi, 2005) is not appropriate to adopt in this region as its few seismic network coverage.

Therefore the near-source interaction SdP is chosen in our study, which is favorable for investigating the discontinuity to a scale ∼100 to 200 km comparable to the slab thickness including the degree of depression and/or uplift. Short period S-to-P conver-

17
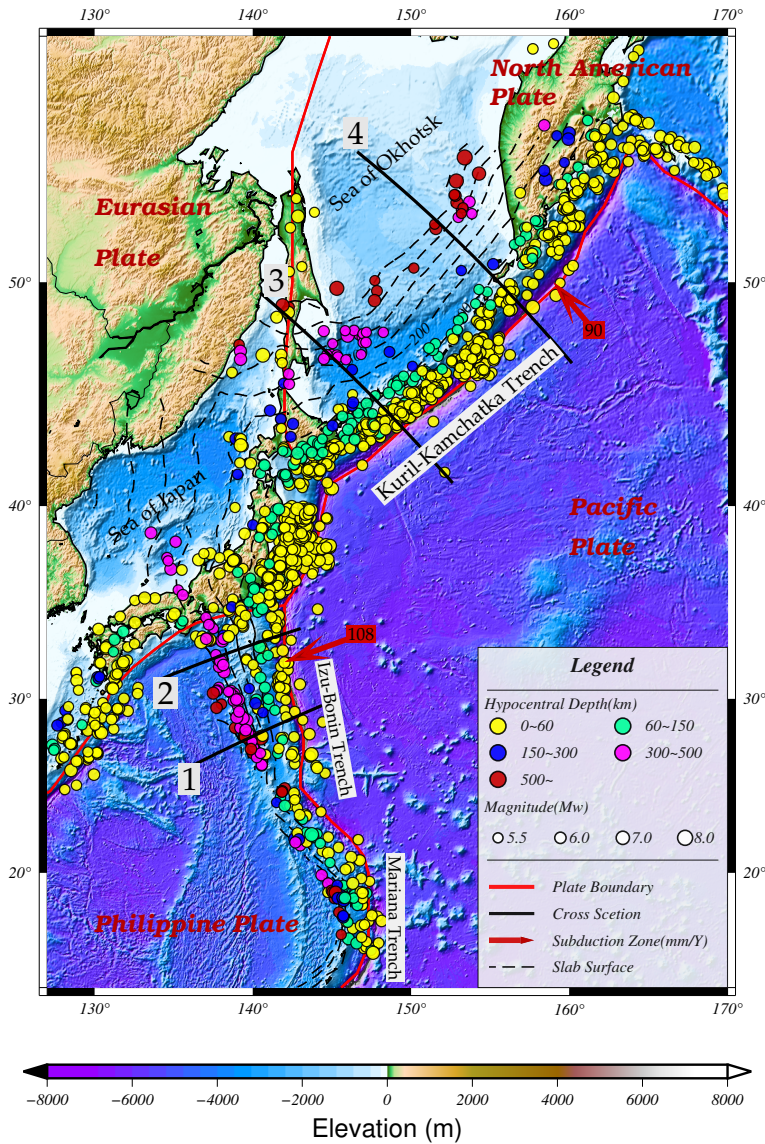
Figure 5: Features of depth and location of earthquakes at the Kurile and Izu-Bonin regions from 1985 to 2020. Colors and size of circles show the depth and magnitude of the earthquakes respectively. Shallower ones generally in the vicinity of the plate boundary while deeper ones appear along the direction of the subduction (red arrows). The topography of the Northwest Pacific is represented by the background colors.
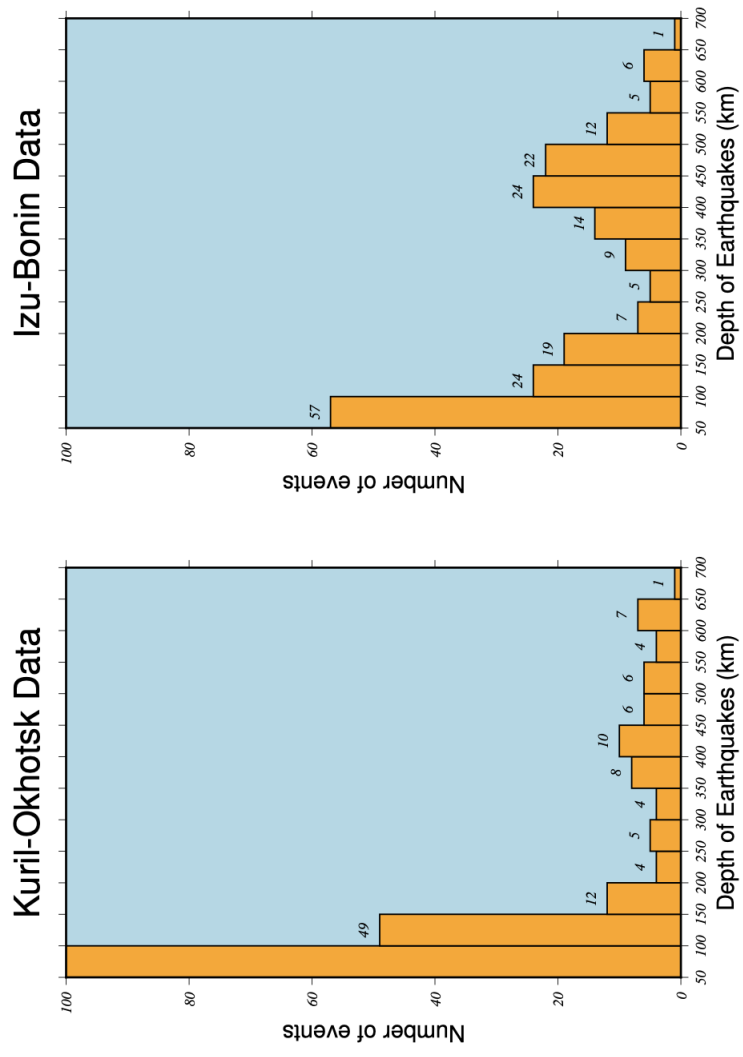
Figure 6: Distribution of focal depth in Kurile and Izu-Bonin regions. Kurile region has more events with a depth between 100∼150 km while Izu-Bonin region has more deeper events with depth between 300∼600 km.

sion wave has a narrow Fresnel zone compared to near-receiver conversion (P660s) used in the receiver function technique or long period underside reflected phases(S660S). Correspondingly smaller scale structure of the discontinuity should be visible. There are two main limitations of the S-to-P conversion phase: (1) it is typically weaker than the noisy level generated by near-surface reverberations and powerful arrivals such as pP, which do limit our choice of events (events with depth shallower than ∼50km cannot not be used) and investigative methods, i.e., a dense array needs to be chosen with ∼100 to 200 stations and relatively small aperture typically less than 10 degree and the non-linear slant stack should be used to make it from background, (2) S-to-P converted waves can be observed only intermittently for an event-array pair with a favorable focal mechanism.

We measured the depths of the 660 km discontinuity beneath the Kuril-Kamchatka and Izu-Bonin trenches by using the analyses of P coda to detect S660P, which is a wave that leaves from an earthquake, propagates as down-going S wave (shear wave), converts to P wave (compressional wave) at the 660 km discontinuity, and follows the path similar to the direct P wave. The delay between S660P and P depends systematically upon the focal depth (Richards & Wicks Jr, 1990). Source-side geometry of the ray paths of S660P (Figure 4) indicates that the S660P phase arrives later than P wave with a delay time in a range of ∼5 to 60s in our study. As it travels in the mantle between the foci and the discontinuity as a slower S wave than P, deeper events give smaller delays. With the knowledge of focal depth and seismic wave velocities, the relative delay time between P and S660P can be calculated and used to detect the phase. We then use the measured delay in travel times between direct P wave as reference and S660P to determine the apparent conversion depth. We use the IASP91 for the reference velocity model (B. Kennett & Engdahl, 1991), which is modified for changes in the depth of the '660 km discontinuity' by assuming the same velocity gradient both above and below the discontinuity. The apparent conversion depth of S660P is then regarded as the 660' km discontinuity. This phase usually has a low amplitude, so that it cannot be seen in the individual records. We adopt the N-th root slant stack to enhance its signals

proposed by (Kanasewich, Hemmings, & Alpaslan, 1973).

The Si-to-P method suppresses uncertainty caused by earthquake location and origin time of stations. Uncertainty caused by unusual structure in the mantle near the 660 km discontinuity and the structure near receiver also are suppressed by using the S660P-P traveltime delay instead of absolute time. Because of these advantages this method has been widely used to investigate the regional features of '660' discontinuity in Izu-Bonin (Castle & Creager, 1998) (Collier & Helffrich, 1997) (Wicks & Richards, 1993), and Tonga-Fiji (Richards & Wicks Jr, 1990) (Niu & Kawakatsu, 1995) (Kaneshima, Kubo, & Yoshioka, 2012).

3.3   Array Analysis: Nth-Root Slantstack

Figure 7 shows an example of record section of seismograms and results of slant stacking for a deep event that has a focal depth of nearly 460km recorded by an array located at the US. It is difficult to identify or pick later phases that are produced by S-to-P conversion at the the 660 discontinuity in P coda at individual records as their phases are very weak, often only a few percent of direct P and very close to the background noisy level caused by near-receiver reverberations and some other noise. The most widely used technique to distinguish this low amplitude S660P phase from the P wave coda is to stack the data from the array containing a large number of receivers as mentioned above. Therefore, the N-th root slant-stack algorithm (Kanasewich et al., 1973) is adopted in our study. By stacking the individual trace, coherent signals such as converted phases generated by near-source structure (SdP, PdP) are significantly enhanced while the background noise is suppressed. Shallow events (<50km) are not chosen since they are always contaminated by near-surface reverberation while intermediate and deep events typically show relatively quiet P coda.

Our data processing mainly includes the following steps:

(1) First, the events whose seismograms have favorable signal-to-noise ratio are selected. The traces for which arrivals of direct P waves cannot be seen clearly (noisy

traces) are removed and a band-pass filter is applied on high-quality traces with corner frequencies of 0.1 Hz and 2.0 Hz, and 0.2 and 1.5 Hz for broad-band and short-period data, respectively. The amplitude of P is basically ∼2 times or more than its coda wave. For each trace, the arrival time of P wave is picked for aligning all the traces to it as reference time as well as the amplitude which is used to normalize the amplitude as a standard. This means that the direct P wave occurs at time zero with an amplitude of 1.0, which excludes the uncertainty caused by the differences in origin time and in amplitude between different receivers.

(2) Second, for each incoming wave with a ray parameter p (also called slowness) that arrives at the j-th station at time i, its amplitude is represented by A_{ij}. The time lag between this station and center of array (τ_j) can be expressed as $d_j * p$ by using the epicentral distance difference of j-th station and array center, d_j. The aperture enclosed with specific epicentral distance and azimuth, rather than a real station) is defined. For the case of the array contains K stations, the N-th root slant-stack for a specified slowness p is given by

$$R_i(p) = S_i(p) \left| S_i(p) \right|^{N-1} , \tag{3}$$

where

$$S_i(p) = \frac{1}{K} \sum_{j=1}^{K} sign(A_{i+\tau_j,j}) \left| A_{i+\tau_j,j} \right|^{\frac{1}{N}} \tag{4}$$

For each event, we stack by using a time window up to 180s after P and non-linear Nth-root algorithm with N=4 is chosen, which is a favorable value to include later phases and to facilitate their identification despite distorting the waveforms.

An example of time verse slowness picture of the stacked amplitudes (called vespagram) is shown in Figure 7. Horizontal and vertical axes represent the difference to P wave in arrival time and slowness respectively. Color scale from red to blue represents the polarity and intensity of the phases. A point on the vespagram represents the sum along a line representing the slowness p through a seismic section and is plotted at the

time at a reference distance and at the slowness across the array.

This method robustly enhances coherent signals, which are caused by the structure common to all receivers, such as near-source discontinuity (660-D), while reducing incoherent signals, such as high-amplitude but uncorrelated energy caused by reverberations under the receiver arrays. This is the reason that stacking helps improve the signal-to-noise ratio. And it is widely used to enhance weak arrivals in P coda by (Niu & Kawakatsu, 1995) (Niu & Kawakatsu, 1997) (Kaneshima & Helffrich, 1998) (Collier et al., 2001).

3.4   Hypocenter Depth Redetermination

The time delay between S660P and P is only moderately sensitive to the epicentral distance but is very sensitive to the hypocenter depth. A Kuril event of 460km depth, f or example, recorded by the CI array near the west coast of the US with epicentral distance 63°, a difference in epicentral distance of 0.5 degree (∼60km) translates to almost ∼1s of variation in S660P-P delay, while the difference of only ∼10km in hypocentral depth gives rise to the same amount of the change in S660P-P delay time, which means ∼0.1s in S660P-P delay corresponding to ∼1km depth change. Therefore, accurate investigations of local topography of '660' discontinuity are possible only if the hypocentral depths are well determined.

The ISC-EHB bulletin provides the dataset with depth constraints based on the combination of the EHB algorithm (Engdahl, van der Hilst, & Buland, 1998) and some other catalogue such as USGS broadband depth and GCMT solution, which covers the years 1964-2016 and typically characterized by a standard error with ∼5km (level 1), ∼5 to 15km (level 2), and >15km (level 3), depending on the data quality. Although a small part of the events used in our study are classified in the catalogue as high accuracy in depth, there are also many events that have a standard error greater than 15km. In this study we obtained accurate estimates of hypocentral depth by using the time interval between P and the depth phase pP, which propagate as upward P wave,
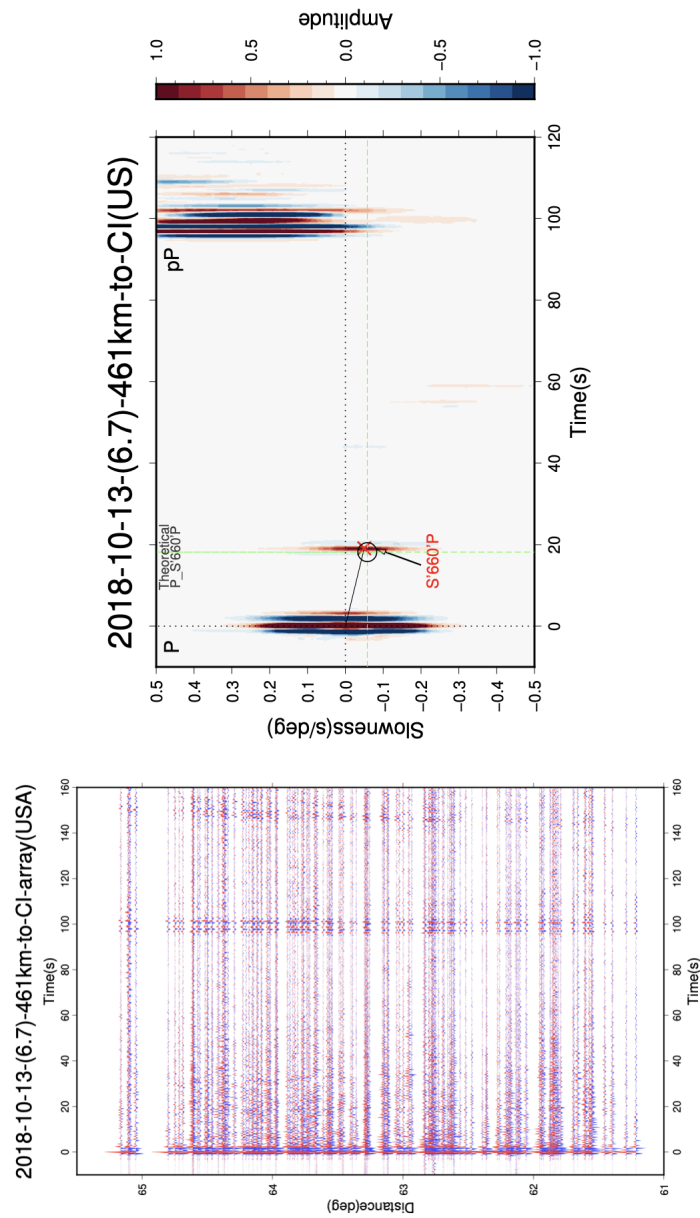
Figure 7: Example of Non-linear Slant Stack. (left) Record section of broad-band vertical component (BHZ) CI networks of a Kurile event as shown in its label. Vertical axis show the epicentral distance and horizontal axis shows the relative arrival time to direct P as we align all the traces to P arrival time. (right) The Vespagram the non-linear slant stack by using N=4. Vertical and horizontal axis shows the relative slowness and time to P phase, means that P has a slowness of 0 s/deg and arrive at 0 s. Later phases such as pP and S660P appear at the upper and lower part as their slowness greater or less than P, their relative time from P based on our travel time calculation.

reflected by surface then arrive at the receiver, and enhanced by slant stacking by using the same array data. Since pP are almost always can be observed clearly within a ∼150s time window after direct P for deep events, they provide a powerful method to redetermine the depth, which can be utilized in our study. By using this strategy, we calculated hypocentral depths typically with a standard error of ∼2 to 6 km, which is similar to the catalogue of ISC-EHB level-1 (∼5km).

3.5   Calculation of Travel-Time and Identification of Later Phases

(1) Travel-Time calculation

In order to use the delay time between the P and S660P, we calculate get their accurate travel time by using the standardcalculation method proposed by (Julian & Anderson, 1968):

We divided the earth into n spherical shells, and for each layer the seismic wave velocity is defined by analytic function of radius r in radial coordinate and twosome other parameters a_i, and b_i :as

$v = a_i r^{b_i}$ when $r_i \leq r \leq r_{i+1}$ for $i = 1, 2, 3, \ldots, n$.

Then we define the angular distance D(r,a,b,p) and travel time T(r,a,b,p) from a specific radius r to the surface for a ray path with a conventional slowness p as:

$$D(r, a, b, p) = \frac{1}{1-b} \cos^{-1} \frac{ap}{r^{(1-b)}} \tag{5}$$

$$T(r, a, b, p) = \frac{1}{1-b} \sqrt{(\frac{r^{1-b}}{a})^2 - p^2} \tag{6}$$

The total angular distance and travel time for a ray from surface to surface is the integral of all the layers it passed:

$$Delta = 2\{D(r_{j+1}, a_j, b_j, p) + \sum_{i=j+1}^{n} [D(r_{i+1}, a_i, b_i, p) - D(r_i, a_i, b_i, p)]\} \tag{7}$$

25

$$Time = 2\{T(r_{j+1}, a_j, b_j, p) + \sum_{i=j+1}^{n} [T(r_{i+1}, a_i, b_i, p) - T(r_i, a_i, b_i, p)]\} \qquad (8)$$

Where j is the index of the layer at the ray bottom. For a ray of the event which do not occur at earth surface, the contribution of the layers from the foci to surface are subtracted from the integral.

(2) Identification of later phases

It is a crucial part to distinguish later phases including S660P and others in P coda on the vespagram, since the measured S660P-P time delay is used to determine the apparent S-to-P conversion depth which is regarded as the depth of the 660 km discontinuity. In this study, we detect weak phases corresponding to S660P based on their slowness and travel time according to the following process.

Firstly, the slowness is an important standard to judge the scattering phases. In principle, waves interact with discontinuities or scatters above (below) the source has positive (negative) slowness relative to direct P wave. According to the source side geometry (Figure 4), S660P has the negative slowness relative to P, thus the waveform of S660P will appear in the bottom half of the vespagram, plot of stacked amplitude on the time versus slowness space (Figure 7) since we choose the P as the reference phase (i.e., arrival time and slowness of P is zero). The slowness resolution of the array depends on its aperture and, typically about 0.06~0.1s/°, for the sizes of the arrays we use. We identify arrivals with the difference between observed and theoretical slowness less than the resolution. Slowness difference between P and S660P varies with focal depth, shallow events have a larger difference up to about -0.16s/° for a focal depth ~130km, while for a deeper events this difference is about -0.01~-0.08s/° (Figure 8).

Secondly, an S660P appears later than P on the record section because it propagates as a slower S wave between source to discontinuity, for each event, we calculate the theoretical time delay between them via the knowledge of the redetermined focal depth and epicentral distance by using theoretical arrival time of S660P phase for the IASP91 Vp and Vs models (B. Kennett & Engdahl, 1991). The amplitude should be taken

into account althouh the S660P is a weak phase in P coda. In our study, we adopt the Nth-root(N=4) slant stack enhance the low-amplitude coherent phases. The arrivals of S660P phases that are found in our study have amplitudes about $\sim$0.05 to 0.3 (which of P is 1.0) on the linearly stacked (N=1) seismograms. Therefore some of relatively large-amplitude waves are not be identified as S660P when masked by powerful depth phase pP which has a much larger amplitude about 0.6 0.9 for shallower events. For deeper event examples shown in Figure 8, up-going reflection s/p410P phases are occasionally observed in our study, which with low amplitude only about 1% of P, 20 30% of S660P in linear stack (not greater than 60% in N=4).
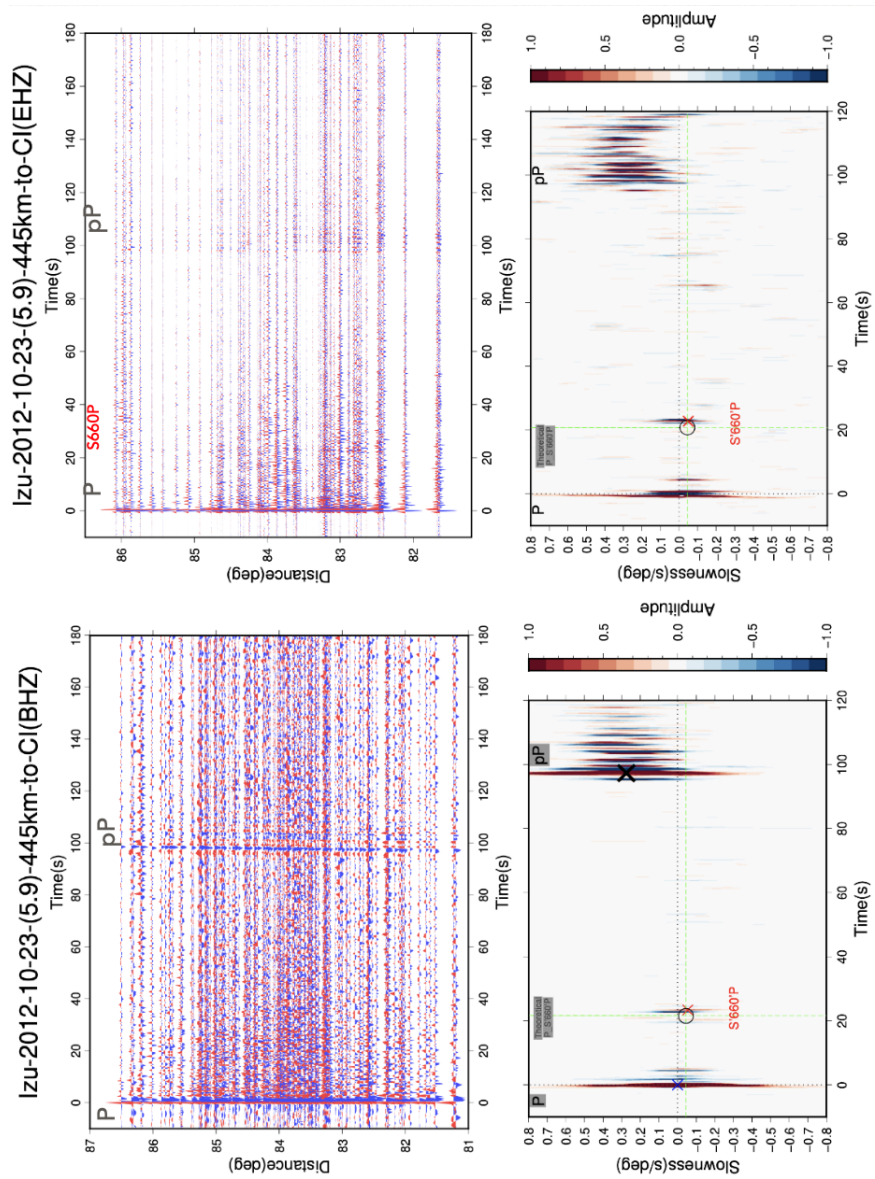
Figure 8: Later Phases Identification. Record sections (upper) and vespagrams (lower) of same event which recorded by different kinds of seismograms, black circle and red cross show the theoretical and observed travel time respectively. As the slowness resolution is about 0.05 s/deg, later phases with slowness ±0.05 from theoretical value are reasonable to be considered as S660P.

4 Results

4.1 Kurile Region

Figure 9 shows the overall features of the 660 km discontinuity in the Kurile-Okhotsk region, including the structure of the subducting slab, the distribution of earthquakes and conversion points. Black thin lines show the geometry of the slab (Hayes, Wald, & Johnson, 2012), with the direction of subduction from SE to NW. Earthquakes for which the S660P is observed are expressed in a form of a beach ball, while the other ones shown by small black circles. Dense clusters of shallower events are concentrated near the Kuril island arc, and focal depths gradually become deeper toward the inland direction at the Sea of Okhotsk area. We divided the region into two sub-regions for which we show cross-sections that are approximately perpendicular to the strike of the trench are drawn. Southern and Northern parts are chosen with the centers near Sakhalin-Hokkaido Islands and Kamchatka Peninsula, respectively. This division is adequate since the subducting angle and configuration of the Wadati-Benioff zone as well as recently tomography studies illustrate significantly different situations in subducting between the two sub-regions. The observed S660P conversion points are shown with colors, shallower ones with cool colors typically beneath the Kuril arc, shallower than ∼400 km, whereas deeper ones with warm colors almost beneath the slab subducting through the MTZ reaching a depth near ∼700 km. Circles and squares mark represent the conversion phases observed for different source-receiver combinations.

For each sub-region, we made a cross-section to investigate the topography of the 660 km discontinuity superimposed on both P and S-wave tomography models. P-wave models are better to delineate the shape of subducting slabs in the upper-mantle, while elastic anomalies closely related to S-to-P conversion would be those in S speed. In this study several recently tomography models are used are used to infer the shape of subducting slab and to correct the velocity anomaly in the upper mantle: GAP-P4 (Obayashi et al., 2013) (Fukao & Obayashi, 2013), UU-P07 (Amaru, 2007), HMSL-S/P06 (Houser et al., 2008), TX2019-slab-S/P (Lu, Grand, Lai, & Garnero, 2019).

The southern section (AA', Figure 10a) is centered at 45°N,147.5°E (0° at horizontal axis). Red hollow circles and green squares represent events and conversion points respectively. The configuration of the Wadati-Benioff zone shows a dipping angle about 45° with the deepest earthquakes distributed nearly horizontaly at 600 km depth, which is consistent with an idea of a slab stagnating above the 660 km discontinuity but partially penetrating across it into lower mantle (at the horizontal location near -5°) based on the tomography studies mentioned above. The deepest depth of the discontinuity is observed near the horizontal location at -3°with a depth of about 685km. The depression of the discontinuity appears ∼180 to 220km (∼1.5°) wide, which is nearly but not strictly beneath the deepest earthquakes. As moving toward landside, we do not clearly see if the 660 km discontinuity being depressed or returning to the global mean depth, since the lack of observed conversion points at the horizontal range from -4° to -6°except one near -7° limits our image of the discontinuity beneath the part where the slab is deflected horizontally. At seaward, the 660 km discontinuity tends to become shallower with an average depth of 660 to 665 km at the horizontal range from -1.5° to +1.5°. It gradually uplifts to 645 km depth away from the slab (at ∼0° to 2°). According to tomography models, the depression appears to be located at high-velocity anomaly with an amplitude of about +1.0% in both GAP-P4 and UU-P07, while about +1.5% in TX2019-S. The uplift generally appears to be located in a low-velocity anomaly away from the slab with an amplitude of -0.8% to -1.2% for P models and about +0.5% for S models.

For the northern section (BB', Figure 10b) with a center at the horizontal location of (0° corresponding to 51°N,154°E) the representation of the symbols is the same as those in section AA'. The deepest events are located near 640±20 km, indicating that the slab through the 660 km discontinuity penetrates into the uppermost lower mantle. We observed an apparent depression which is narrower but deeper than the AA' section with a width of about 1.2° (∼130km) and an amplitude of about 35km. The depth of the 660 km discontinuity is depressed up to ∼695km directly beneath the deepest events near -2.5°. The depth of the discontinuity gradually becomes shallower to a depth of

30

660 670km near -1.5°. As moving to seaward, the 660 discontinuity uplifts to the depth near 650 km nearby the center and with a depth of about 660 km in ordinary mantle at ∼2°. Tomography models show a depression that is located at a place with a slightly weaker high-velocity anomaly of about +1.0%, which represents the colder slab. On the other hand, the uplift corresponds to low-velocity anomaly away from the slab.

We also made the cross section along the line almost parallel to the trench (section CC' Figure 11). The blue parts does not strictly indicate the shape of the slab but roughly shows the cold subducted lithospheric material with relatively faster seismic wave velocities. In this section, the slab descends in a 'distorted' way bending horizontally near the location 0°and the observation of some deep earthquakes with focal depth near 600 km at the central and northern parts are consistent with this feature. As the mantle temperature can affect the depth of the post-spinel phase boundary, the 660km discontinuity in this region can change along the direction that is approximately parallel to the arc.

We note that the conversion points observed by using S660P emitted from shallower earthquakes (with a focal depth of ∼100 to 200km) are located father away from the slab than those observed by using deeper ones in the lateral direction, which means that the S660P wave propagates longer distance as a slower S wave for the shallower events than deeper events. The upper mantle seismic velocity heterogeneity, especially in S wave can influence the results of the S660P delay for the shallower events, since S waves have a larger travel time anomaly than P in the same distance.

4.2   Izu-Bonin Region

Figures 12 and 13 show the tectonic features and earthquake distribution of the Izu-Bonin region. The studied area of our research is enlarged in Figure 13. Dotted lines show the geometry of the slab Hayes et al. (Hayes et al., 2012), which shows a subducting direction from NW to SW. Earthquakes for which S660P are and aren't observed are expressed in a form of a beach ball and small black circles respectively, as in the case
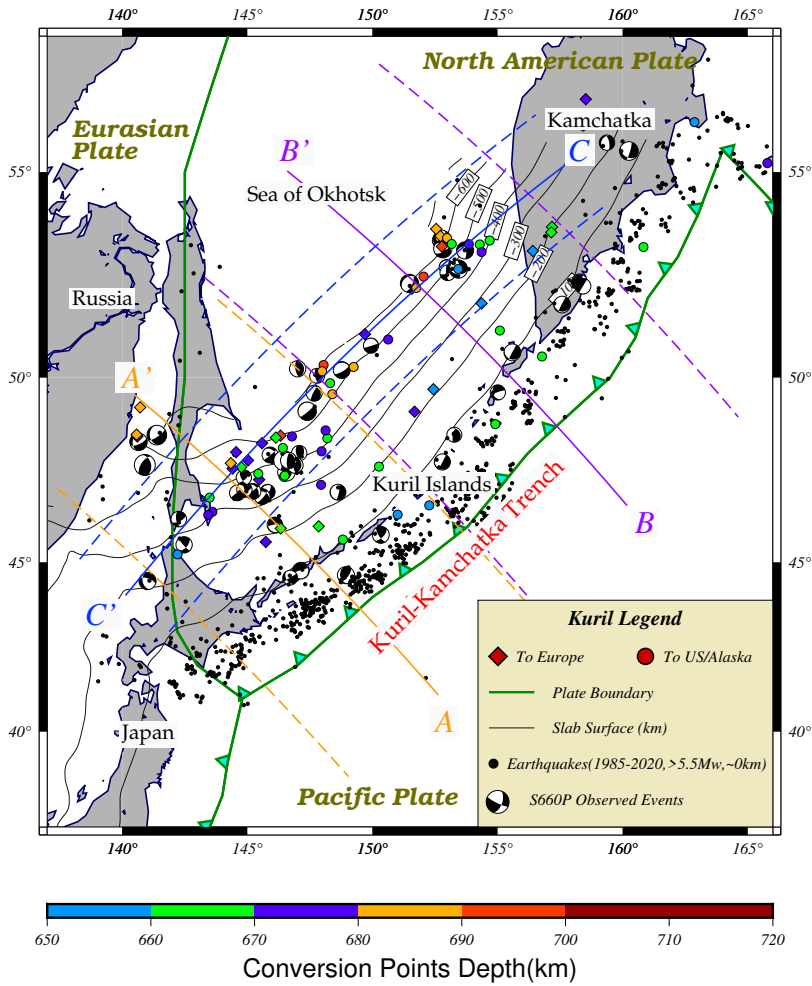
Figure 9: The overall features of Kurile Region. Black thin lines show the contour of the slab, green thick line with arrows show the plate boundaries and subducting direction, orange purple and blue lines indicate the range of the cross-sections. Events which S660P are observed represented by beach balls and others by small black points. Conversion points of S-to-P at the 660 km discontinuity expressed by quadrilaterals and circles as shown in legend.
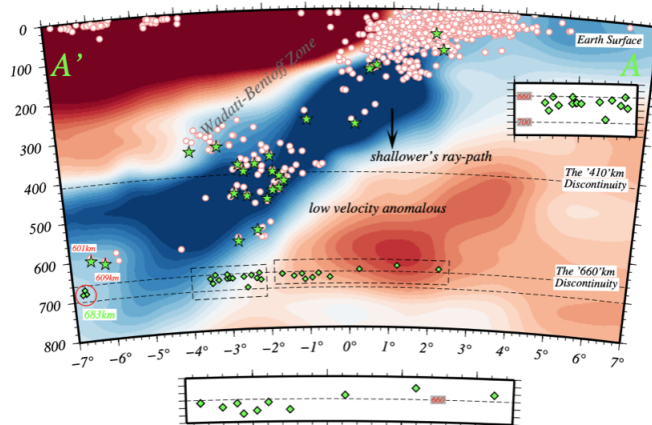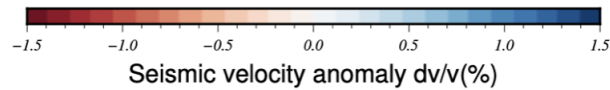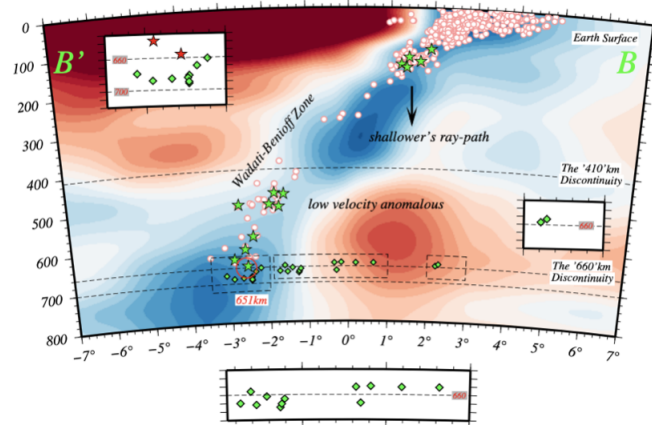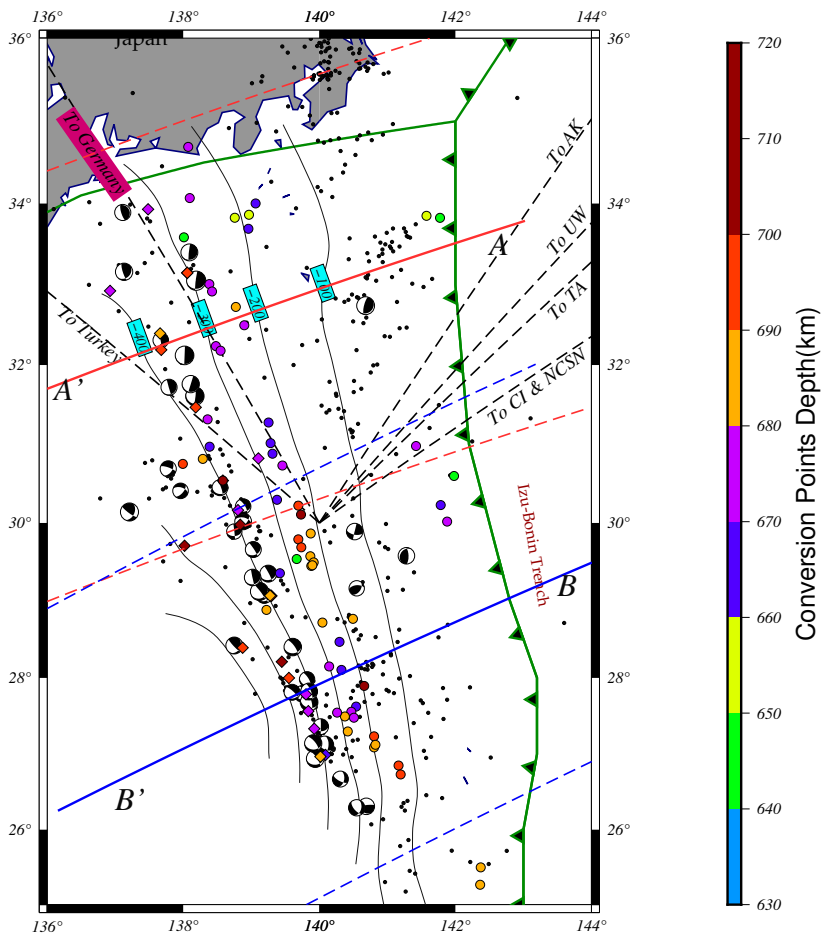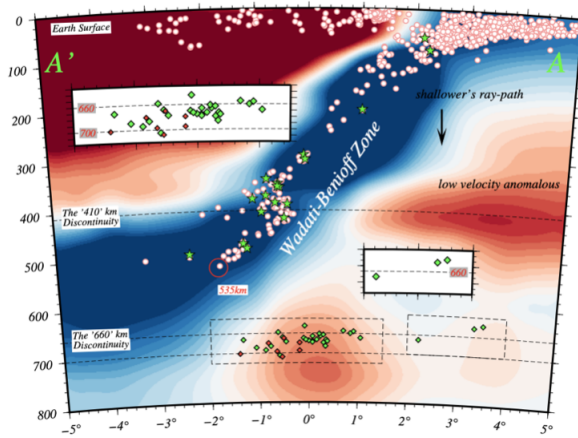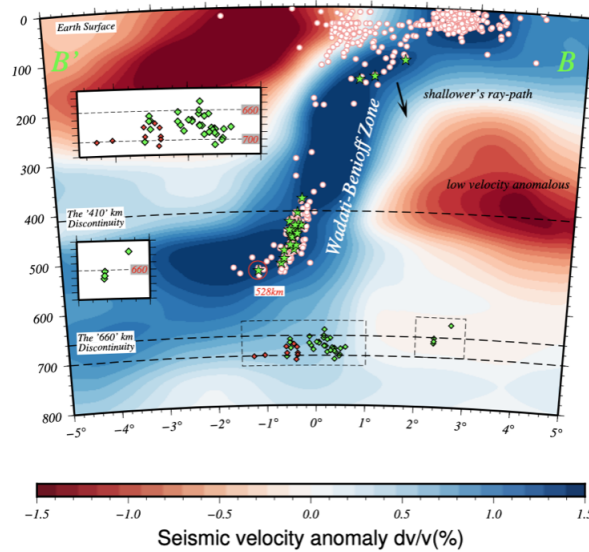
Figure 10: Cross Sections AA' (upper) and BB' (lower) of Kurile Region. Blue and red background colors correspond to high and low-speed anomalies through the tomography models. Red circles represent the earthquakes and those S660P are observed ones are shown by green stars. S-to-P conversion points are shown by green squares, areas surrounded by dotted lines are expanded in the insert figures with same coordinates.
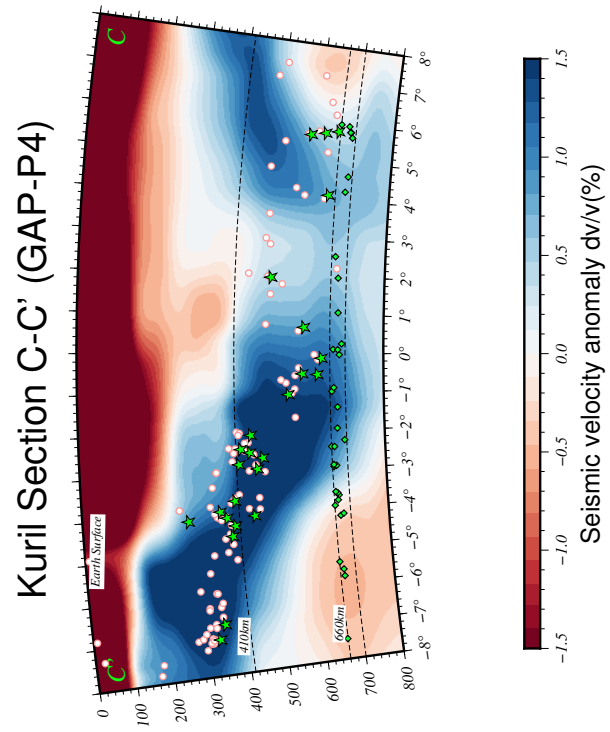
Figure 11: Cross Sections CC' of Kurile Region, elements in the figure are same as figure 10.

of Kurile. A dense cluster of shallower events is seen near the Izu-Bonin trench, and the focal depths gradually become deeper toward the subducting direction. We divided the research area into two sub regions for which cross-sections that are approximately perpendicular to the trench with the centers at the northern and southern parts of this region are drawn. The observed S660P conversion points are shown with colors, shallower ones with cool colors typically beneath the Izu Bonin arc, whereas deeper ones with warm colors almost beneath the slab. Circles and squares represent the conversion phases observed by different source-receiver combination.

4.3 Tomographic Correction

Lateral heterogeneity in seismic velocities in the upper mantle can affect the estimates of the conversion depths derived from the delay times of S660P. Such effects are negligible for deep events because of short lengths of S wave paths before reaching the conversion points. The effects, however, can be significant for intermediate depth earthquake. One way to evaluate such effects would be to utilize recent tomography models providing the distributions of P and S wave speeds. Since relative magnitudes of the P and S wave speed anomalies are required for the correction, we define a parameter R as S-toP heterogeneity, which represents the ratios of velocity anomaly between S and P waves in the upper mantle by the following form:

$$\frac{\delta V_s}{V_s} = R\frac{\delta V_p}{V_p}; \quad R_{\frac{V_s}{V_p}} = constant \tag{9}$$

Figure 15 shows the velocity anomalies as a function of depth for the regions for the Kuril region away from the slab in the upper mantle, for the lateral range from 0° to 2° for AA' and from 0.5° to 2.5° for BB', where the 660 km discontinuity is identified by shallower events. Solid and dashed lines represent the P and S models respectively. The used models are mentioned above. The value of R changes within a range between 0.6 and 1.6 for AA' and between 0.8 and 2.0 for BB' for the depth range from 100km to 660 km. We especially focus on the depth from 300 to 600km, where P and S velocity

35
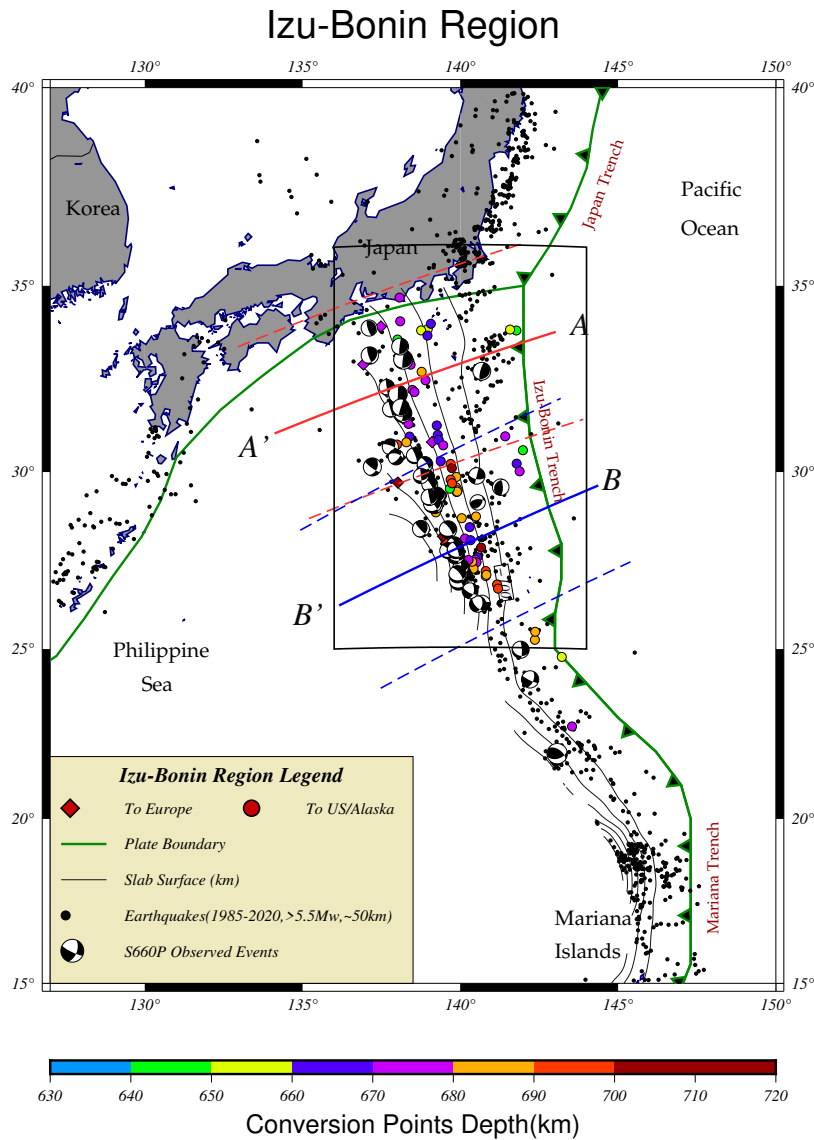
Izu-Bonin Region

Figure 12: The overall features of Izu-Bonin Region. Black thin lines and green thick lines with arrows show the the contour of the slab and plate boundaries, orange purple and blue lines indicate the range of the cross-sections, research area in our study is enclosed by the black square. Events which S660P are observed represented by beach balls and others by small black points. Conversion points of S-to-P at the 660 km discontinuity expressed by quadrilaterals and circles as shown in legend.

Figure 13: Enlarged map of the area which enclosed by black square in figure 12.

Figure 14: Cross Sections AA' (upper) and BB' (lower) of Izu-Bonin Region. Blue and red background colors correspond to high and low-speed anomalies through the tomography models. Red circles represent the earthquakes and those S660P are observed ones are shown by green stars. S-to-P conversion points are shown by green squares, areas surrounded by dotted lines are expanded in the insert figures with same coordinates.

anomalies typically show opposite signs, which can significantly affect the S660P time delay after P by such amounts that can be translated to the depth change of about 5 to 8km of the 660 km discontinuity. The same approach is also applied at deep events result, but this correcion is not larger than 2km in the disconinuity depth, which can be neglected.

The 660 km discontinuity in both AA' and BB' shows a similar characteristic that typically becomes deeper near the slab. This is because a coder subducting slab material makes the 660 km discontinuity deeper as is expected for the endothermic post-spinel phase transition from ringwoodite to perovskite + ferro-periclase. The discontinuity becomes shallower gradually away from the slab core, which is consistent with the difference between a colder subducting lithosphere and warmer pyrolite mantle.

The 660-km discontinuity does not have a large depression at the mantle where the subducted slab does not exist. This corresponds to the mantle where the seismic waves propagate away from the slab to the US. Such absence of depression is expected because this region does not have a rapid temperature change in lateral direction.
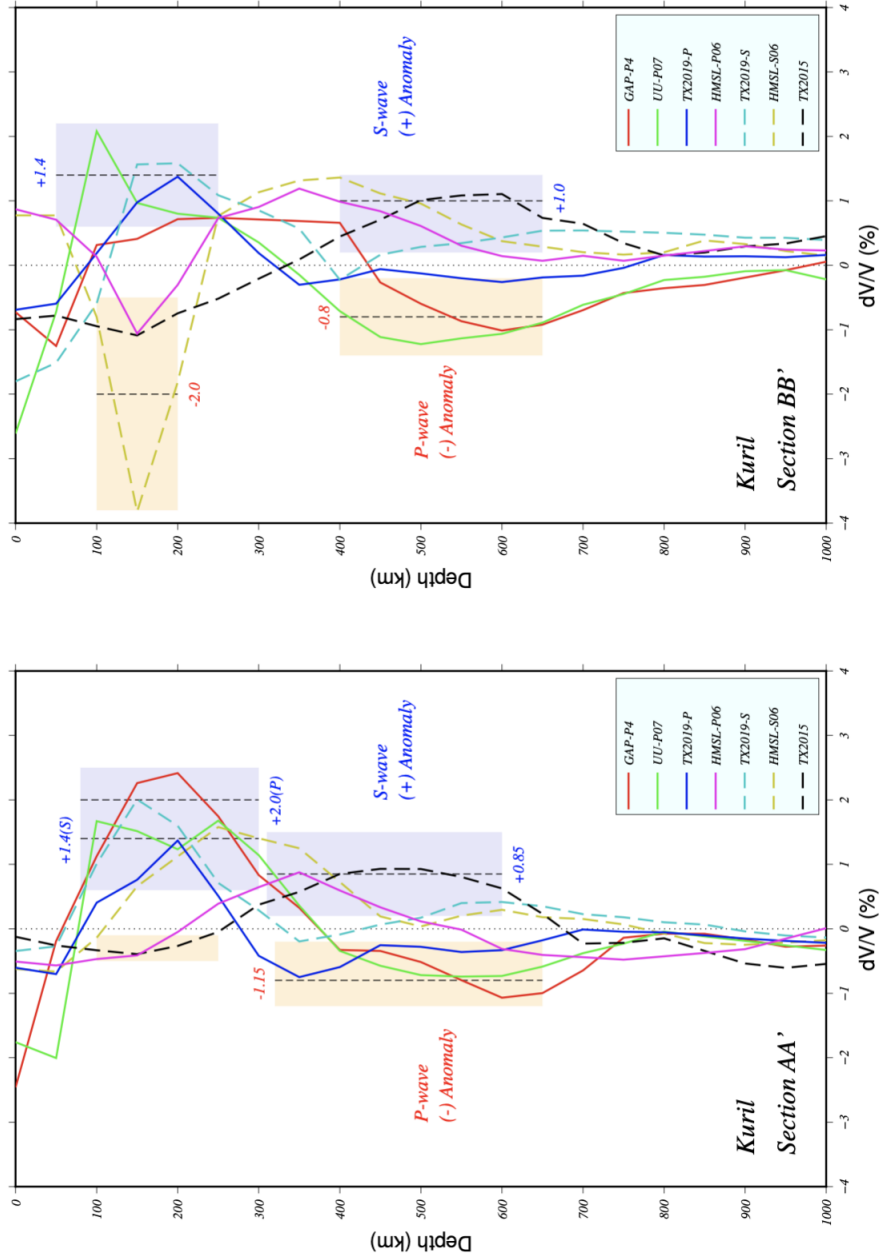
Figure 15: Tomographic Correction of Kurile. Tomography models used in our study and their representation are shown in the legend. High-speed and low-speed anamolies generally concentrate in the depth range of 100∼200 and 400∼600 km which marked by purple and orange squares.
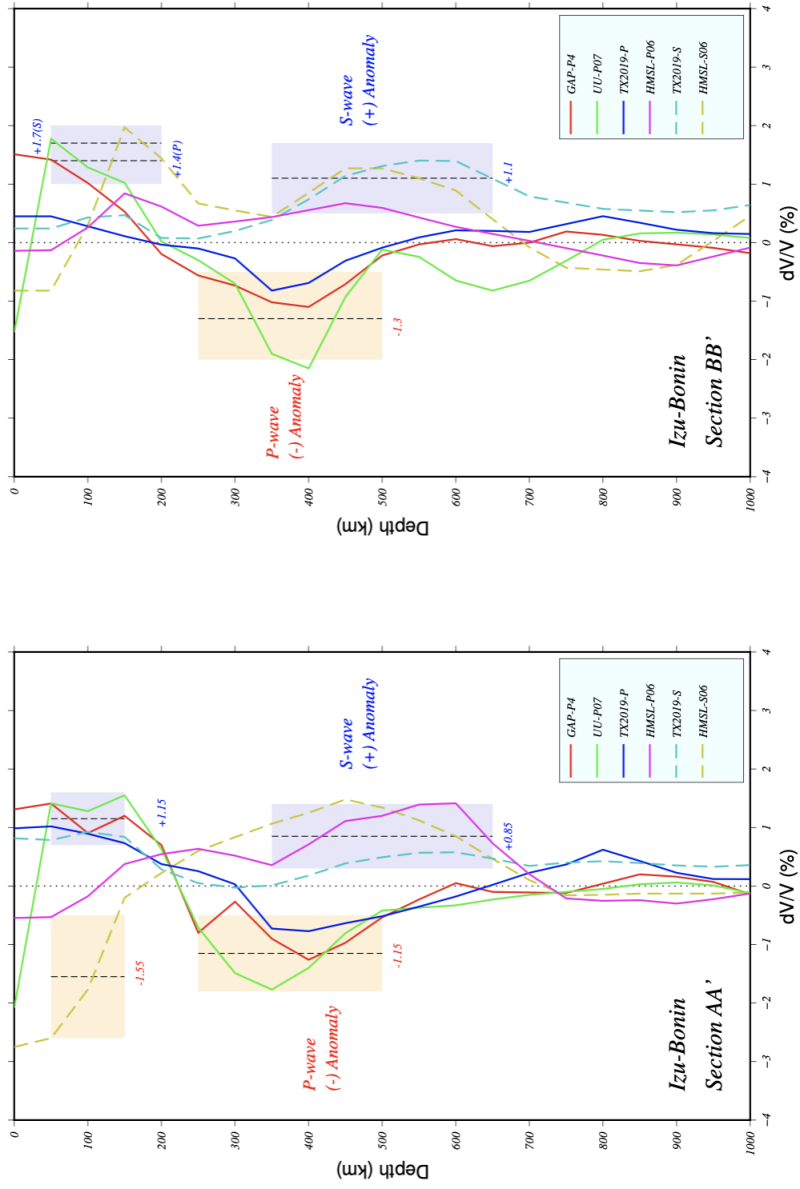
Figure 16: Tomographic Correction of Izu-Bonin.

Kurile Cross-section A-A'

(a)

Kurile Cross-section B-B'
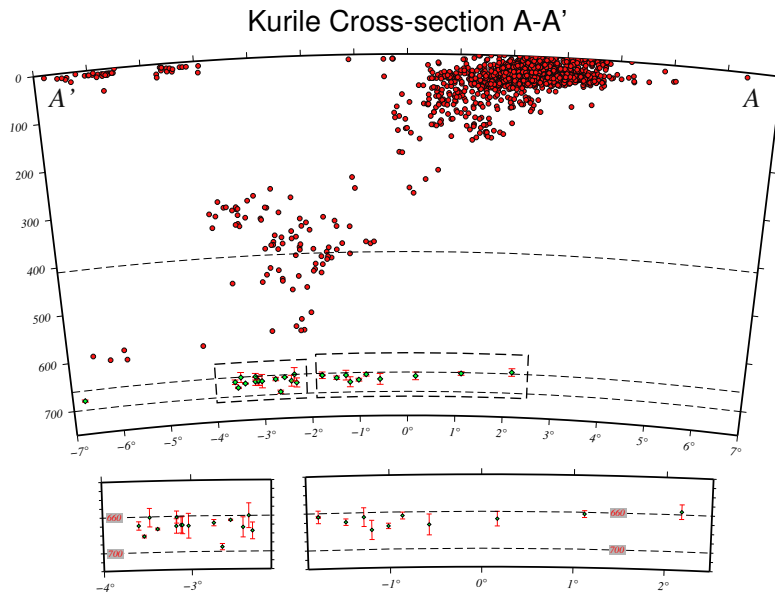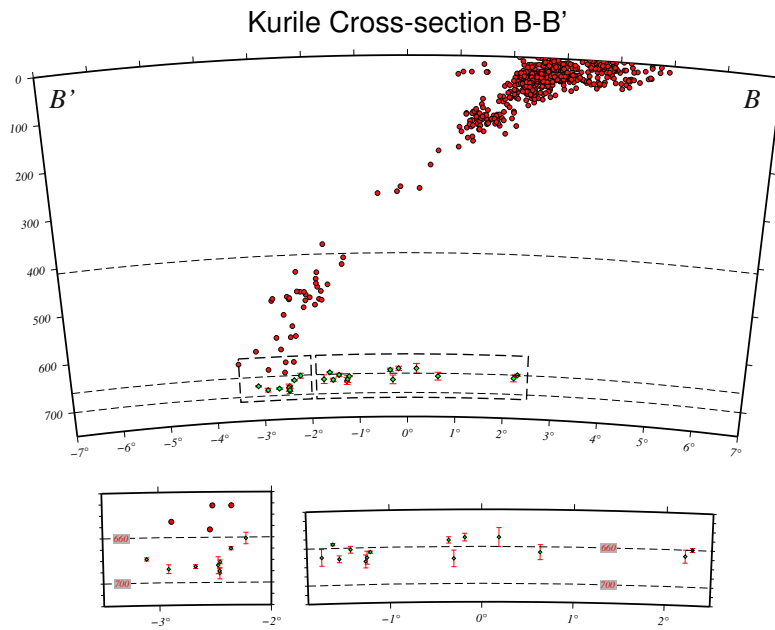
(b)

Figure 17: Cross sections with error-bars in Kurile region.

42
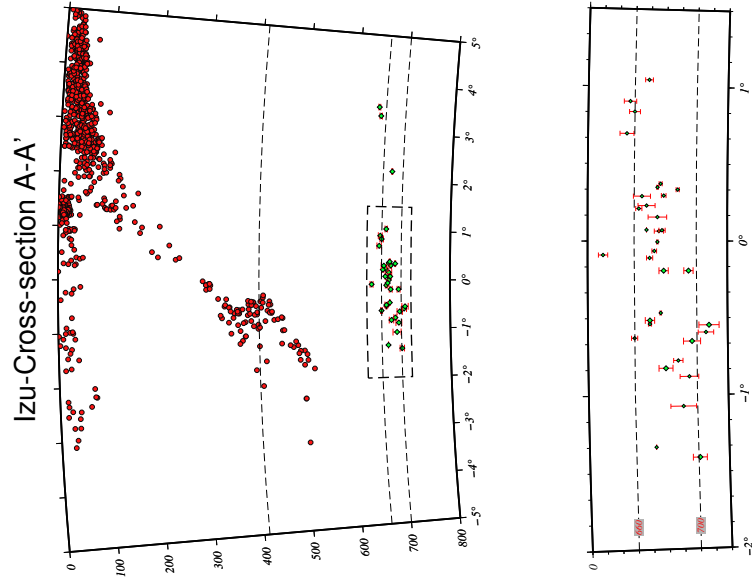
(a)
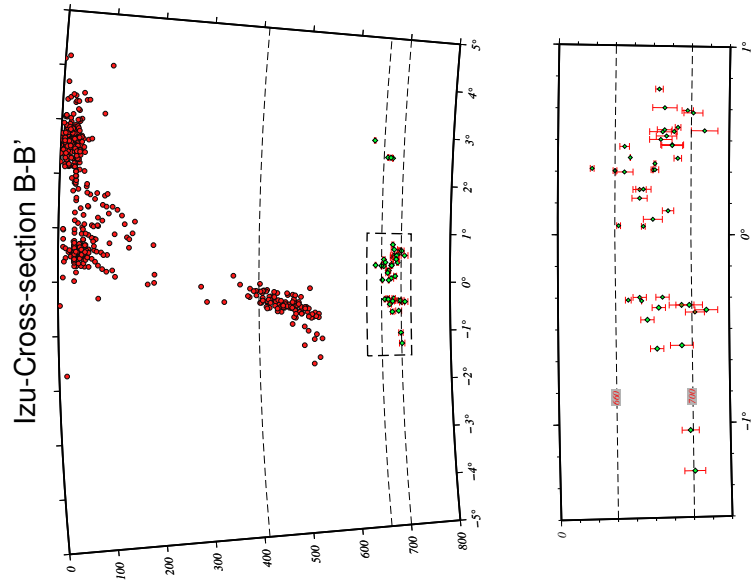
(b)

Figure 18: Cross sections with error-bars in Izu-Bonin region.

5 Discussion

1. S660P observed for shallower events

The histogram in Figure 19 shows the number of events which S660P are observed in the Kurile (top) and Izu-Bonin (bottom) regions and the distribution of their focal depth respectively. In the Kurile region, clusters of events are mainly divided into two parts: the shallower one with focal depths between 100 and 200 km and the deeper one with those between 300 and 500 km. For the Izu-Bonin region, most of the S660P are observed for the events with focal depth between 350 and 550 km, and only a few events (number less than 10) with focal depth between 100 and 200 km show S660P. This feature is consistent with the distribution shown in figure 6 that more shallower earthquakes (between 100 and 200km) for the Kurile region while more deeper ones (between 300 and 500 km) for the Izu-Bonin region.

On the other hand, the ratios between the numbers of the events with S660P observations and the total numbers of the earthquakes analyzed are 64/125 for the Kurile region and 80/116 for the Izu-Bonin region. By comparing these ratios, we find that the deeper events generally show a higher efficiency in observing the S660P. Their higher probability is because of quieter P coda, which makes weak later phases easier to be identified after stacking as also reported in previous studies (Richards & Wicks Jr, 1990) (Castle & Creager, 1997) (Castle & Creager, 1998). However, we also find S660P by using shallower data especially for the Kurile region, although the S660P have sometimes weaker amplitude which hinders us to distinguish them from the background to some extent or tend to be covered by strong major signals such as pP. We attempted to analyze shallower events as much as possible for observing S660P by using shallower events, those with focal depths in the range from 100 to 200 km. These events are located near the trench of Kuril subducted slab, and their ray paths toward the US should interact with the discontinuities with the S660P conversion points located away from the slab. This indicates the shallower events have the potential for investigating the structure of the 660 km discontinuity which rarely mentioned in previous studies.

2. The uncertainty of our results

The error bars shown in Figures 17 and 18 mainly come from the relocation of focal depth, typically showing an error of $\sim$5 to 10 km. Some events, however, show a relatively large error up to about 20 km mainly due to the following situation: the waveform polarity of pP are defficult to determine, which is somewhat related to its focal mechanism. The waveform of pP also sometimes show a duration of 10 to 20 s with a series of waves that prevents from picking the first pP arrival.

An S660P usually appears as effectively the only noticeable phase in the vespagram near the theoretical time and slowness obtained from the velocity model with the slowness anomaly generally in a range of the slowness resolution about ±0.05 s/deg, which represent the depth of '660' km discontinuity shallower or deeper than the average value. However sometimes other phases with similar order of amplitude appear in the vicinity of the S660P in the vespagram which derived by modified velocity model. (shown for the event array pairs: Izu-1995-10-01-UW; izu-2007-04-01-TU; izu-2008-10-01-UW; izu-2012-01-01-EU; izu-2012-10-23-NCSN and AK; izu-2016-08-25 in Appendix). In such situations, the error-bar will be about ±5 km corresponding to the arrival time of S660P of ±1s.

Both earthquake depth relocations and tomographic corrections used 1-D velocity model in our study can cause the error in the S660P depth. As for earthquake epicenter locations, the epicentral errors proposed by ISC-EHB are 0.1 degree which translate to an error in travel time less than 0.1s, which does not affect our results. The 1-D correction used in this study is sufficient for deep events but may be insufficient for intermediate events since the velocity structure may change laterally in the direction perpendicular to the section. However, the validity of the correction for tomography models itself is not necessarily warranted, considering possibly large uncertainty in the tomography models themselves. and more tomographic cross sections should be taken into account.

3. Comparison with previous research

In this section we thoroughly compare our results with previous studies in terms of

two aspects: one is the topography of the 660km discontinuity and the other is it the lateral mantle temperature anomaly it suggests under the assumption of the Clapeyron slope. (Houser, 2016) investigated the global topography of the 660km discontinuity by using the long-period SS precursors. In the Kurile region, at the Southern part, the 660km discontinuity is uplifted to a depth between 640 and 650km at the area away from the slab, which is similar to our short-period result. On the other hand, (Shearer & Masters, 1992) revealed that at the southern part of Kurile the 660km discontinuity is depressed to the depth about 670 km with a width about 8 degree directly below the deepest earthquakes, while our result shows a depression of 100 to 250km wide, suggesting that our short-period S-P conversion data have a better resolution in investigating the small scale (order of about 100 km) topography of the 660km discontinuity than long-period approaches.

In the Izu-Bonin region, the 660 discontinuity in the area away from the slab is uplifted to a depth of 640 to 650km, which is shallower than that reported by (Houser, 2016) with depth about ~655 and 660km. At the northern part (AA'), our data set samples the area that nearly 1°behind the deepest earthquakes in the vicinity of lateral position of about 0°. In the southern part (BB'), the 660 discontinuity is depressed to about 690 km depth beneath the deepest events with a width about 1.5 deg (~200 km), which is narrower than the result of (Wicks & Richards, 1993). Near the horizontal position at 1°, the depths of the conversion points appear quite different around the same location in the cross sections. This is because the cross-sections cover a rather wide area parallel to the arc with significantly different modes of the slab subduction, which might change in this direction as shown in figure 11.

Temperature-pressure conditions should significantly affect the topography of the 660 discontinuity representing the boundary of the post-spinel phase transition. The value of the Clapeyron slope of this boundary proposed by previous studies mentioned before widely varies from -0.5~-4 MPa/K. The large uncertainty in the Clapeyron slope hampers detailed interpretations of the 660 km discontinuity topography in terms of temperature. We thus discuss about the thermal structure of the slabs tentatively

assuming a value for the slope as is done in most previous studies. At the southern part (AA') of the Kurile region, the 660 discontinuity is depressed to about 675 km depth at the horizontal position of about -3° and to 680 km depth beneath the deepest event at the horizontal location about -7°, which corresponds to an temperature anomaly of ∼300℃ around the slab by using the Clapeyron slope of -2.5 MPa/K. At the northern part (BB'), beneath the deepest earthquakes the 660 discontinuity is depressed to 690 km depth at the horizontal location of about 2.5° , which corresponds to a 600℃ anomaly in the center of the slab. This would be the clearest cases so far about the depression of the topography near the likely coldest places in a subducting slab.

At the Izu-Bonin region, the northern (AA') and southern (BB') parts show that the 660 km discontinuity is depressed to 685 km depth near the horizontal location about -1° at AA' and to 690 km depth near the horizontal location near -0.5° at BB', corresponding to a ∼500℃ and ∼600℃ anomalies in the vicinity of the slab respectively, when an equilibrium phase transition with the Clapeyron slope of -2.5 MPa/K is assumed. Such temperature anomalies should occur near the core of the slab rather than around it, so that they cannot readily interpreted by realistic thermal structure of the slab. A possible situation is that the non-equilibrium metastable transformation exists beneath the Izu-Bonin slab, similar to the situation proposed for (Kubo, Kaneshima, Torii, & Yoshioka, 2009) Mariana. The N-type phase due to the nucleation kinetics of the post-spinel transformation may exist at the area where the Izu-Bonin slab is descending across the 660 km discontinuity while the bulk of the slab is being bended to horizontal upon the 660 km discontinuity. It would not be easy, however, to envisage the 660 discontinuity depressed to such depth at the oceanward side of the slab.

4. Relative amplitudes of S410P and S660P

In our data set the S410P phase is also observed for some of the intermediate events. S410P propagates from the source to the 410 km discontinuity as an S wave and is converted to a P wave until the receiver. This phase can be used to compare the nature of the 410 km and 660 km discontinuities, since the S410P and S660P are emitted from

the source toward similar directions so that the radiation of the S waves relative to direct P waves should be similar to each other. The amplitude ratios between them for the events for which both of they are observed at the same time (such as Kurile event 2016-01-11-US as shown in appendix) are not greater than 0.6. This imply the 410 km discontinuity is not as sharp as the 660 km since the olivine spinel phase transformation for the 410 km discontinuity occurs within a wider than the post spinel transformation, leading to a smaller visibility in short-period data.
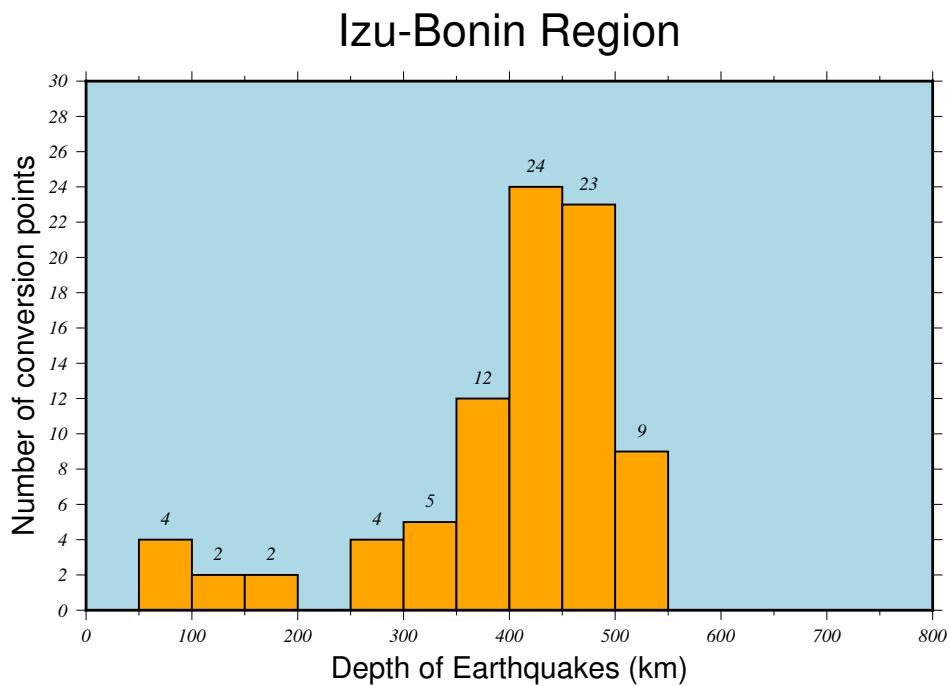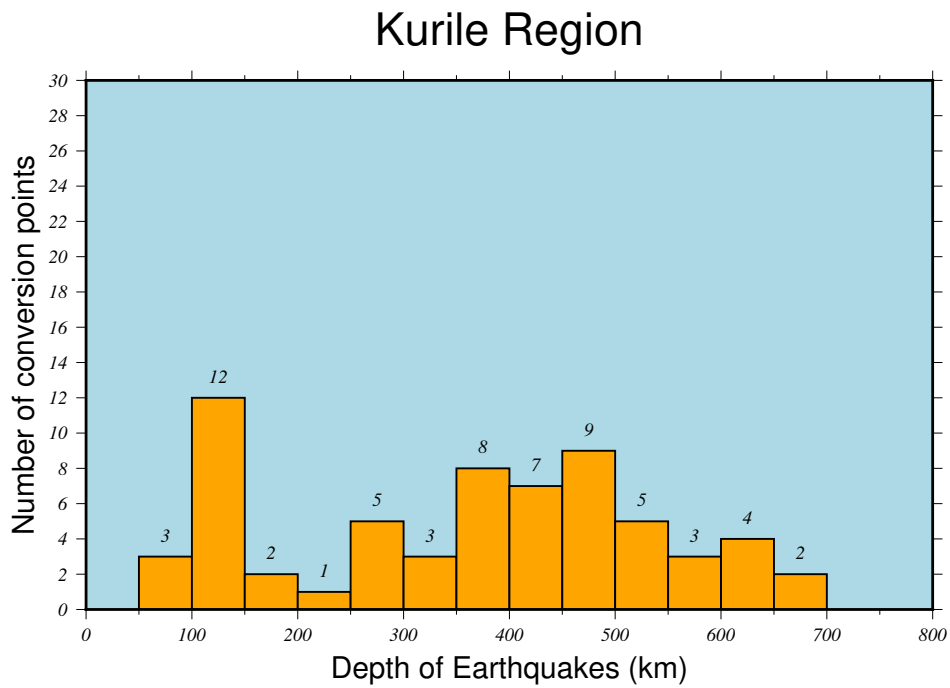
Figure 19: The distribution of the focal depth which S660P are observed in the Kurile (top) and Izu-Bonin (bottom) regions respectively.

6 Conclusion

We analyzed over 200 seismic data with focal depth from 50 to 650 km, for deep and intermediate earthquakes that occurr between 1985 to 2020 at he Kurile and Izu-Bonin subduction zones and are recorded by arrays located at United States, Alaska, China, West Asia, and Europe (German, Italy, Turkey). We observed hundreds of short-period S-to-P conversion points for the Kurile and Izu-Bonin regions and delineated the topography of the 660 discontinuity beneath them. For the Kurile region the topography of the 660 km discontinuity was delineated clearly for the first time. In the northern Kurile region, the 660 km discontinuity is depressed to about 690 km depth directly under the deepest events with a width of about 150 km. For a Clapeyron slope of -2.5 MPa/K of the post spinel transformation the depression corresponds to a temperature anomaly of -600 ℃ near the center of the slab.

Observations for the Izu-Bonin region show that the 660 km discontinuity is descended to about 685 and 690 km depths away from the deepest event by about 100 to 200 km towards the trench direction both in the northern and southern parts. For the Clapeyron slope of -2.5 MPa/K, it suggests a temperature anomaly of ∼500 to 600 ℃ in the vicinity of the slab. We confirmed the results from the previous studies and investigated a wider range by using some shallower seismic data which are able to know the topography of discontinuity far away from the slab.

For the Clapeyron slope of -2.5 MPa/K, there is no major contradiction between the discontinuity depressions and lateral temperature anomalies due to the slab for the Kurile region, but for the Izu-Bonin it is difficult to explain the relationship between the topography of the discontinuity and plausible temperature anomaly in the vicinity of the slab.

7   Acknowledgement

Table1: Data of Kurile Region

Date Y/M/D	Lat. (deg.)	Long. (deg.)	Depth (km)	Mw.	Net.	Distance (deg.)	'660' (km)	S-to-P Point Long.	Lat.
1982 11 27	50.1130	147.7390	619.4	5.6	UW	56.5184	691	148.0459	50.3181
1984 04 20	50.0380	148.7490	577.4	6.0	EU	74.3298	—	—	
1984 04 20	50.0360	148.7490	577.4	6.0	UW	56.0666	681	149.2455	50.2688
1984 04 23	47.4190	146.7140	399.0	6.0	EU	76.5229	—	—	
1984 04 23	47.4190	146.7140	399.0	6.0	UW	58.9094	679	147.9657	48.0572
1985 10 18	46.2320	146.2530	254.3	5.9	EU	60.0298	673	145.4704	47.2914
1985 10 18	46.2320	146.2530	254.3	5.9	UW	77.5457	674	145.4704	47.1521
1986 07 19	47.2380	151.0930	136.0	5.9	EU	77.6593	—	—	
1987 05 18	49.2060	147.6790	545.6	6.8	UW	56.7949	685	148.3956	49.5653
1987 07 14	49.6160	147.8070	578.5	5.9	EU	74.5508	—	—	
1987 07 14	49.6160	147.8070	578.5	5.9	UW	56.8998	669	148.3052	49.8513
1990 05 12	48.9840	141.8590	602.5	7.2	EU	73.0366	—	—	
1990 08 20	46.0350	142.2820	324.2	5.9	UW	62.0202	661	143.4927	46.8010
1991 07 05	47.9090	145.8080	442.7	5.6	EU	75.5229	—	—	
1991 07 05	47.9090	145.8080	442.7	5.6	UW	58.9224	677	146.7838	48.4538
1992 03 27	47.8790	147.1520	417.4	5.5	EU	75.9581	—	—	
1992 03 27	47.8790	147.1520	417.4	5.5	UW	57.8247	665	148.1959	48.4066
1992 06 16	45.6360	142.2720	313.6	6.0	UW	62.4816	670	143.6028	46.4109
1992 06 16	45.6360	142.2720	313.9	6.0	WUS	75.3064	671	143.4382	46.3229
1992 10 11	50.4590	153.1740	282.5	5.6	EU	75.2706	—	—	
1992 10 11	50.4590	153.1740	282.5	5.6	UW	53.0782	666	155.0894	51.1912
1994 08 02	52.4330	158.0300	138.4	5.9	EU	74.3183	662	157.1740	53.7181
1994 08 02	52.4330	158.0300	138.3	5.9	UW	50.0332	662	160.8301	53.2403
1994 08 02	52.4330	158.0300	138.4	5.9	WUS	57.3323	—	—	
1995 02 18	46.6730	145.8960	335.2	5.6	UW	59.7092	—	—	

Date	Lat	Lon	Depth	Mag	Region	Value			
1995 08 04	52.8490	152.8630	519.5	5.5	EU	72.2914	—		—
1995 11 30	44.2770	145.6370	134.6	5.9	WUS	71.545	—		—
1996 02 01	44.8450	146.2890	153.4	6.2	EUS	84.6172	—		—
1996 02 22	45.2800	148.5150	100.2	6.3	EU	78.2837	—		—
1996 08 30	52.2980	151.4890	580.0	5.5	UW	53.8381	—		—
1996 08 30	52.2980	151.4890	580.0	5.5	WUS	60.3183	—		—
1996 08 30	52.2980	151.4890	580.5	5.5	WUS	72.4076	—		—
1997 11 15	43.8530	144.9850	158.0	6.1	EU	78.6622	—		—
1997 11 28	47.1080	145.6060	390.6	5.5	EU	75.5839	670	145.0274	47.8138
1997 12 20	53.4300	152.7300	605.0	5.9	EU	72.1626	688	152.5470	53.6713
2000 07 10	46.8300	145.3960	352.7	5.8	TA	76.259	664	146.4562	47.3669
2000 07 10	46.8300	145.3960	352.7	5.8	EU	75.9833	661	144.7523	47.6297
2000 12 22	44.8300	147.1470	144.8	6.2	TA	73.8973	662	148.8177	45.6378
2000 12 22	44.8300	147.1470	144.8	6.2	EU	79.9114	664	146.3349	45.9511
2001 02 14	48.5660	153.2080	146.8	5.6	WUS	64.1366	—		—
2001 02 26	46.7870	144.4920	383.2	6.1	WUS		—		—
2001 10 03	47.0770	148.6050	277.1	5.9	EU	77.5739	—		—
2001 10 03	47.0770	148.6050	277.1	5.9	TA	64.741	660	150.2602	47.6455
2002 05 21	44.4810	146.5710	148.1	5.5	EU	78.3864	675	145.7368	45.5708
2002 07 17	48.5600	153.1890	145.5	5.5	EU	78.1708	650	152.4337	49.6936
2002 10 16	51.9260	157.2850	123.3	6.2	EU	76.4925	650	156.4104	53.1468
2002 10 16	51.9260	157.2850	123.3	6.2	TA	54.5606	—		—
2002 11 17	47.9080	146.2020	483.9	5.8	EU	76.0569	671	145.5847	48.2744
2002 11 17	47.9080	146.2020	456.4	5.8	EU	75.7466	—		—
2002 11 17	47.9080	146.2020	483.9	5.8	TA	84.5279	660	146.4185	48.1467
2002 11 17	47.9080	146.2020	456.4	5.8	WUS	61.2796	—		—
2003 06 16	55.4780	159.9920	182.1	6.9	EU	73.2745	—		—
2003 06 16	55.4780	159.9920	182.1	6.9	WUS	49.5489	659	162.8695	56.1313

2004 06 10	42.4050	143.0310	187.4	6.8	EU	72.1732	—		—
2004 07 08	47.2050	151.3550	123.2	6.3	EU	76.6959	—		—
2005 09 21	43.9320	146.2070	102.2	6.0	EU	79.627	—		—
2005 11 23	50.0450	147.7400	629.2	5.5	WUS	63.2646	681	147.9854	50.1582
2006 05 22	54.3070	158.4930	190.1	6.2	TA	73.0113	—		—
2006 05 22	54.3070	158.4930	190.1	6.2	EU	73.0708	—		—
2006 06 22	45.4400	149.3970	106.1	6.0	EU	77.8981	—		—
2007 05 30	52.1600	157.2830	122.3	6.4	EU	74.33	—		—
2007 05 30	52.1600	157.2830	122.3	6.4	WUS	55.7509	—		—
2007 08 28	49.7040	154.3610	119	5.6	EU	75.7996	—		—
2007 09 03	45.8210	150.1340	100.6	6.2	WUS	64.5581	657	152.2691	46.5877
2009 04 18	46.0890	151.4530	51.0	6.6	EU	78.7185	—		—
2009 04 21	50.8290	155.0390	157.2	6.2	EU	79.8474	653	154.3597	51.8668
2009 04 21	50.8290	155.0390	157.2	6.2	WUS	56.6554	—		—
2009 10 10	47.8880	152.5080	133.5	5.9	EU	77.8543	673	151.6805	49.1089
2009 10 10	47.8880	152.5080	133.5	5.9	WUS	55.8897	667	154.9071	48.7786
2009 12 10	53.4350	152.7300	653.2	6.3	EU	71.5207	686	152.7182	53.5025
2009 12 10	53.4350	152.7300	653.2	6.3	WUS	53.2607	682	152.9804	53.4557
2010 07 25	49.7050	154.7020	134.1	5.6	EU	75.5813	—		—
2010 07 25	49.7050	154.7020	134.1	5.6	WUS	67.4344	660	156.7715	50.5356
2011 07 18	52.7560	153.0570	503.0	5.5	AK	32.6096	—		—
2011 07 18	52.7560	153.0570	503.0	5.5	EU	75.3713	692	152.7716	53.2514
2011 08 04	48.8210	154.8550	50.5	6.1	EU	76.8214	—		—
2011 10 21	43.8560	142.5330	189.1	6.2	TA	81.1329	—		—
2011 12 09	46.9860	144.6160	383.4	6.2	TA	84.8861	665	145.4359	47.4547
2012 07 29	47.3410	139.0950	506.4	5.7	WUS	66.6759	681	139.8321	47.7748
2013 04 19	46.1770	150.8770	109.1	6.1	WUS	64.2726	—		—
2013 05 24	52.2150	151.4740	632.7	6.7	EU	74.613	—		—

2013 05 24	52.2150	151.4740	632.7	6.7	TA	81.0351	685	151.7493	52.2493
2013 08 04	46.9330	145.2950	374.6	5.8	EU	74.5948	674	144.4097	47.5933
2013 08 04	46.9330	145.2950	374.6	5.8	WUS	68.9224	664	146.4923	47.4027
2013 08 31	47.9640	148.1230	388.4	5.7	AK	38.2937	—		—
2013 10 01	53.1560	152.8650	578.4	6.7	EU	73.3832	—		—
2013 10 01	53.1560	152.8650	578.1	6.7	TA	79.9601	661	153.1656	53.3143
2013 11 12	41.6870	139.3450	60.5	6.5	WUS	53.5164	678	165.7821	55.2052
2014 07 20	44.6500	148.7630	61.4	6.3	AK	40.7592	657	151.0047	46.3337
2014 07 20	44.6500	148.7630	61.4	6.3	EU	78.2852	668	147.8492	46.0093
2014 09 18	50.5870	150.1590	501.9	5.6	EU	68.0808	679	149.6995	51.0991
2014 09 18	50.5870	150.1590	501.9	5.6	TA	80.5638	670	150.6287	50.9652
2014 10 02	52.3670	157.9900	147.6	5.8	EU	74.2418	664	157.1466	53.5901
2015 07 07	43.9830	148.0180	51.1	6.3	AK	41.8295	—		—
2015 10 16	55.6510	159.1090	285.1	5.6	EU	74.2981	670	158.5231	56.6388
2016 01 11	44.4580	141.1170	238.8	6.2	TA	80.1631	659	142.2084	45.2234
2016 01 30	54.0200	158.4980	163.2	7.2	EU	72.1571	—		—
2016 07 23	47.7110	146.9550	408.0	5.8	AK	37.2111	670	148.1268	48.6146
2016 07 23	47.7110	146.9550	408.0	5.8	EU	74.8606	695	146.3219	48.4754
2018 01 18	52.5662	152.9795	447.6	5.7	AK	29.4634	662	154.2876	53.3021
2018 07 01	46.9713	144.9613	387.7	5.6	EU	75.8045	682	144.3375	47.7368
2018 07 01	46.9713	144.9613	388.0	5.6	TA	85.0709	—		—
2018 10 13	52.8549	153.2429	461.0	6.7	UW	55.6791	675	154.4216	53.2067
2018 10 13	52.8549	153.2429	461.0	6.7	AK	33.1244	672	154.4267	53.6166
2018 10 13	52.8549	153.2429	461.0	6.7	AUST	77.6786	—		—
2018 10 13	52.8549	153.2429	461.0	6.7	CI	63.1998	671	154.3583	53.1214
2018 10 13	52.8549	153.2429	461.0	6.7	TA	76.9495	670	153.8491	53.3095
2018 10 13	52.8549	153.2429	461.0	6.7	EU	71.5112	—		—
2018 10 13	52.8549	153.2429	470.1	6.7	Thai	54.9894	690	152.0435	52.525

2018 11 02	47.8166	146.7181	431.9	5.9	AK	41.2854	—		—
2018 11 02	47.8166	146.7181	431.9	5.9	EU	74.9539	668	146.1371	48.4236
2018 11 02	47.8166	146.7181	431.9	5.9	TA	83.0871	—		—
2018 11 02	47.8166	146.7181	431.9	5.9	Asia	50.6454	—		—
2018 11 02	47.8166	146.7181	431.9	5.9	WUS	64.076	—		—
2019 07 09	47.4283	145.0471	437.3	5.5	AK	37.4238	—		—
2019 07 09	47.4283	145.0471	437.3	5.5	EU	76.7996	670	144.5495	48.0336
2019 11 20	53.1633	153.6851	486.8	6.3	AUST	81.1163	656	153.4272	52.7125
2019 11 20	53.1633	153.6851	486.8	6.3	CI	62.9347	665	154.6839	53.3965
2020 11 30	48.2521	140.7971	589.0	6.4	ITA	75.3974	671	140.6041	48.4550
2020 11 30	48.2521	140.7971	589.0	6.4	GR	73.2688	683	140.5702	48.5013
2020 11 30	48.2521	140.7971	589.0	6.4	CI	72.2932	—		—
2020 11 30	48.2521	140.7971	589.0	6.4	UW	61.8513	—		—
2020 11 30	48.2521	140.7971	589.0	6.4	AK	41.1012	—		—

Table 2: Data of Izu-Bonin Region

Date Y/M/D	Lat. (deg.)	Long. (deg.)	Depth (km)	Mw.	Net.	Distance (deg.)	'660' (km)	S-to-P Point Long.	Lat.
1985 04 03	28.2620	139.5490	473.3	6.5	UW	75.7189	681	140.0454	28.7170
1985 09 10	27.2050	139.9390	513.5	6.4	UW	76.1639	675	140.2612	27.5440
1988 09 07	30.2870	137.4530	457.0	6.7	UW	75.4244	691	137.9944	30.7529
1989 06 16	31.8250	138.0980	365.9	6.4	UW	73.9115	677	138.8965	32.4968
1992 08 29	33.2360	138.1340	301.3	6.2	UW	73.0016	669	139.0641	34.0012
1993 10 11	32.0320	137.9470	364.1	6.8	EU	85.7803	—		—
1993 10 11	32.0320	137.9470	366.1	6.8	UW	75.9613	688	138.7734	32.7243
1995 07 07	33.9890	137.2720	340.1	5.9	UW	73.0731	675	138.0734	34.6902
1995 10 01	29.2700	139.1210	458.5	6.1	NCSN	79.7534	690	139.7348	29.6880
1995 10 01	29.2700	139.1210	459.5	6.1	UW	75.5566	690	139.6917	29.7907
1996 02 14	29.2400	140.5590	155.5	5.8	NCSN	78.7563	674	141.8780	30.0173
1996 02 14	29.2400	140.5590	151.5	5.8	UW	74.4346	668	141.7837	30.2288
1996 03 16	28.9720	138.9960	478.6	6.7	EU	89.0959	—		—
1996 03 16	28.9720	138.9960	482.6	6.7	UW	75.6166	662	139.4207	29.3546
1996 06 26	27.6890	139.9130	471.0	6.3	EU	90.6996	—		—
1996 06 26	27.6890	139.9130	473.0	6.3	UW	76.0088	660	140.3251	28.1022
1998 01 01	23.9680	142.0710	94.7	6.3	NCSN	80.1148	654	143.2156	24.7723
1998 01 01	23.9680	142.0710	95.7	6.3	UW	77.3313	—		—
1999 01 12	26.7320	140.3110	450.0	5.9	BKCI	83.0189	680	140.8042	27.0883
1999 01 12	26.7320	140.3110	450.0	5.9	FL	75.5604	674	139.9251	27.3321
1999 01 12	26.7320	140.3110	451.0	5.9	NCSN	79.8457	681	140.8249	27.1217
1999 01 12	26.7320	140.3110	454.0	5.9	UW	76.5172	693	140.8051	27.2329
1999 07 03	26.3180	140.5930	438.0	6.1	BKCI	82.7469	—		—
1999 07 03	26.3180	140.5930	435.0	6.1	EU	92.1839	—		—
1999 07 03	26.3180	140.5930	438.0	6.1	NCSN	79.7259	691	141.1957	26.7313

1999 07 03	26.3180	140.5930	432.0	6.1	UW	76.5594	693	141.1648	26.8490
1999 12 05	29.9440	138.7980	431.6	5.7	NCSN	78.8604	668	139.3788	30.2965
1999 12 05	29.9440	138.7980	433.6	5.7	UW	75.3312	—	—	
2000 06 09	30.4560	137.7740	484.0	6.2	NCSN	78.9328	688	138.2873	30.8161
2000 10 27	26.2630	140.6240	384.6	6.1	EU	92.2787	667	140.0904	26.9875
2000 10 27	26.2630	140.6240	387.6	6.1	UW	76.5780	—	—	
2002 08 02	29.2250	139.1030	420.0	6.2	BKCI	83.1609	648	139.6680	29.5380
2002 08 02	29.2250	139.1030	420.0	6.2	NCISP	21.8593	—	—	
2003 11 12	33.3050	136.9740	388.0	6.3	BKCI	80.7923	—	—	
2003 11 12	33.3050	136.9740	380.0	6.3	NCSN	78.7527	—	—	
2003 11 12	33.3050	136.9740	396.0	6.3	UW	73.8119	—	—	
2005 04 19	29.6340	138.9860	432.0	5.9	NCSN	78.8188	701	139.7313	30.1073
2005 04 19	29.6340	138.9860	426.0	5.9	UW	75.1189	698	139.6916	30.2210
2006 03 28	31.7040	137.8230	413.3	5.9	NCSN	78.8717	673	138.5480	32.1794
2006 03 28	31.7040	137.8230	414.3	5.9	UW	77.2904	670	138.4794	32.2364
2007 03 08	29.9200	140.2860	143.4	6.1	NCSN	78.4024	—	—	
2007 03 08	29.9200	140.2860	144.4	6.1	TU	81.8658	675	139.1043	30.8224
2007 03 08	29.9200	140.2860	143.5	6.1	UW	74.287	678	141.4217	30.9796
2007 04 01	32.3440	137.6650	384.9	5.7	BK	78.2741	678	138.4228	32.9158
2007 04 01	32.3947	137.6601	383.9	5.7	CN	21.8098	680	135.8588	32.8387
2007 04 01	32.3440	137.6650	380.9	5.7	TU	78.8186	673	136.9240	32.9236
2007 04 01	32.3440	137.6650	386.9	5.7	UW	3.9855	676	138.3834	33.0080
2007 09 28	21.9990	142.7590	260.3	7.5	XC	81.1145	675	143.5390	22.7442
2008 07 20	27.7820	139.7320	484.9	5.8	XC	79.7128	673	140.1441	28.1472
2008 10 01	30.1600	138.8360	411.6	5.7	UW	74.9456	679	139.4570	30.7319
2008 10 01	30.1634	138.8033	427.6	5.7	W-CN	35.2735	670	137.5371	30.5534
2009 08 09	33.1580	138.0550	296.3	7.1	BKCI	82.1927	660	138.9571	33.6902
2009 08 09	33.1580	138.0550	302.3	7.1	EU	84.9896	677	137.4830	33.9298

2009 08 09	33.1473	138.0594	307.3	7.1	EU	81.6712	695	137.2781	33.9360
2009 08 09	33.1580	138.0550	294.3	7.1	TA	83.6232	655	138.7572	33.8262
2009 08 09	33.1473	138.0594	307.3	7.1	TU	79.9045	679	137.1147	33.7654
2009 08 09	33.1580	138.0550	295.3	7.1	UW	73.7564	657	138.9659	33.8617
2009 08 12	32.7970	140.4380	62.4	6.6	TA	82.0590	—		—
2009 08 12	32.7970	140.4380	63.4	6.6	XC	75.1265	—		—
2010 05 03	29.6490	141.0870	110.0	6.1	EU	89.5791	—		—
2010 05 03	29.6490	141.0870	93.0	6.1	TA	83.9611	—		—
2011 01 12	26.9640	139.9790	528.7	6.5	AK	58.7694	688	140.3760	27.4942
2011 01 12	26.9669	140.0155	535.7	6.5	C-ASIA	54.4064	682	139.4562	27.3048
2011 01 12	26.9640	139.9790	512.7	6.5	WUS	80.3438	680	140.4177	27.2968
2012 01 01	31.4510	138.1200	354.0	6.8	EU	86.1013	695	137.6763	32.1898
2012 01 01	31.4682	138.1833	390.0	6.8	TU	79.4677	697	137.3901	32.0139
2012 05 26	26.9015	140.1681	484.6	6.0	EU	90.3133	—		—
2012 05 26	26.9015	140.1681	472.6	6.0	AK	81.1877	—		—
2012 10 23	29.0656	139.2767	431.0	5.9	AK	57.4416	686	139.8732	29.8650
2012 10 23	29.0656	139.2767	433.0	5.9	CI-BHZ	83.8961	687	139.8978	29.4572
2012 10 23	29.0656	139.2767	436.0	5.9	CI-EHZ	83.7207	684	139.8814	29.4483
2012 10 23	29.0655	139.2767	449.8	5.9	CN	30.5645	683	138.0410	29.3142
2012 10 23	29.0656	139.2767	440.0	5.9	NCSN	78.7220	686	139.9171	29.4942
2012 10 23	29.0656	139.2767	430.0	5.9	UW	77.3599	685	139.8682	29.5737
2012 11 12	29.7082	138.0196	499.1	5.9	CN	29.2961	701	136.8351	29.9246
2013 04 21	29.9644	138.9741	441.0	6.1	EU	87.0653	706	138.5821	30.5411
2013 04 21	29.9643	138.9741	431.3	6.1	TU	83.6354	—		—
2013 09 04	29.9768	138.8376	411.4	6.5	TU	82.6529	708	138.1333	30.5103
2014 06 30	28.3906	138.8727	534.0	6.2	AK	58.6770	685	139.2233	28.8818
2014 06 30	28.3906	138.8727	524.4	6.2	GR	88.3339	699	138.5678	28.8322
2014 06 30	28.3906	138.8727	523.0	6.2	US	78.4603	—		—

2014 09 21	27.9979	139.5537	487.3	5.5	TU	82.2482	695	139.0564	28.3578
2015 06 23	27.6882	139.7885	462.0	6.5	EU	90.2486	702	139.4494	28.2083
2016 08 04	24.9447	142.8141	515.0	6.3	AK	58.5632	683	142.3725	25.4977
2016 08 04	24.9447	142.0140	510.0	6.3	TU	86.7536	—	—	
2016 08 04	24.9447	142.8141	541.0	6.3	UW	76.8698	689	142.3641	25.2659
2016 08 25	30.6151	137.8462	454.0	5.9	AK	56.7739	670	138.3583	31.3172
2016 08 25	30.6151	137.8462	452.0	5.9	NCSN	79.2938	660	138.3877	30.9709
2016 11 23	27.1549	140.0256	485.0	5.7	NCSN	80.3147	675	140.5091	27.4772
2016 11 23	27.1549	140.0256	484.0	5.7	UW	76.7712	673	140.4707	27.5554
2017 09 07	27.7829	139.8040	456.0	6.1	AK	54.8265	665	140.2968	28.4667
2017 09 07	27.7829	139.8040	453.0	6.1	TU	83.5575	677	139.2725	28.1485
2018 09 01	27.9556	139.9130	439.0	5.6	AK	54.3927	683	140.4942	28.7662
2019 04 05	30.4490	138.6343	400.0	5.8	AK	57.0675	665	139.2542	31.2763
2019 04 05	30.4490	138.6343	393.0	5.8	BKCI	81.3181	663	139.3124	30.8817
2019 04 05	30.4490	138.6344	400.0	5.8	UW	75.2762	668	139.2842	31.0163
2019 06 04	29.0623	139.2931	431.0	6.3	EU	87.7265	—	—	
2019 06 04	29.0622	139.2931	437.3	6.3	GR	88.1115	695	138.9320	29.5935
2019 06 04	29.0622	139.2931	440.3	6.3	TU	82.8395	699	138.6630	29.5092
2019 07 27	33.1460	137.3250	379.0	6.3	AK	54.3996	675	138.0951	34.0665
2019 07 27	33.1460	137.3250	373.0	6.3	BKCI	79.8444	640	138.0094	33.5845
2020 04 18	27.1230	140.1330	471.0	5.7	AK	58.1359	—	—	
2020 04 18	27.1220	140.1330	446.0	5.7	EU	91.0782	673	139.8379	27.5627
2020 04 18	27.2030	140.0720	465.0	5.7	UW	76.6221	665	140.5411	27.6235

References

Amaru, M. (2007). *Global travel time tomography with 3-d reference models* (Vol. 274). Utrecht University.

Barley, B., Hudson, J., & Douglas, A. (1982). S to p scattering at the 650 km discontinuity. *Geophysical Journal International*, *69*(1), 159–172.

BINA, C. (1991). Mantle discontinuities. *Reviews of Geophysics Supplement*, *29*, 783–793.

Bina, C. R., & Helffrich, G. (1994). Phase transition clapeyron slopes and transition zone seismic discontinuity topography. *Journal of Geophysical Research: Solid Earth*, *99*(B8), 15853–15860.

Bock, G., & Ha, J. (1984). Short-period sp conversion in the mantle at a depth near 700 km. *Geophysical Journal International*, *77*(2), 593–615.

Castle, J. C., & Creager, K. C. (1997). Seismic evidence against a mantle chemical discontinuity near 660 km depth beneath izu-bonin. *Geophysical research letters*, *24*(3), 241–244.

Castle, J. C., & Creager, K. C. (1998). Topography of the 660-km seismic discontinuity beneath izu-bonin: Implications for tectonic history and slab deformation. *Journal of Geophysical Research: Solid Earth*, *103*(B6), 12511–12527.

Collier, J. D., & Helffrich, G. R. (1997). Topography of the "410" and "660" km seismic discontinuities in the izu-bonin subduction zone. *Geophysical research letters*, *24*(12), 1535–1538.

Collier, J. D., Helffrich, G. R., & Wood, B. J. (2001). Seismic discontinuities and subduction zones. *Physics of the Earth and Planetary Interiors*, *127*(1-4), 35–49.

Crotwell, H. P., Owens, T. J., & Ritsema, J. (1999). The taup toolkit: Flexible seismic travel-time and ray-path utilities. *Seismological Research Letters*, *70*(2), 154–160.

Dziewonski, A. M., & Anderson, D. L. (1981). Preliminary reference earth model. *Physics of the earth and planetary interiors*, *25*(4), 297–356.

Engdahl, E. R., van der Hilst, R., & Buland, R. (1998). Global teleseismic earthquake relocation with improved travel times and procedures for depth determination. *Bulletin of the Seismological Society of America*, *88*(3), 722–743.

Fei, Y., Van Orman, J., Li, J., Van Westrenen, W., Sanloup, C., Minarik, W., ... Funakoshi, K.-i. (2004). Experimentally determined postspinel transformation boundary in mg2sio4 using mgo as an internal pressure standard and its geophysical implications. *Journal of Geophysical Research: Solid Earth*, *109*(B2).

Flanagan, M. P., & Shearer, P. M. (1998). Global mapping of topography on transition zone velocity discontinuities by stacking ss precursors. *Journal of Geophysical Research: Solid Earth*, *103*(B2), 2673–2692.

Fukao, Y., & Obayashi, M. (2013). Subducted slabs stagnant above, penetrating through, and trapped below the 660 km discontinuity. *Journal of Geophysical Research: Solid Earth*, *118*(11), 5920–5938.

Ghosh, S., Ohtani, E., Litasov, K. D., Suzuki, A., Dobson, D., & Funakoshi, K. (2013). Effect of water in depleted mantle on post-spinel transition and implication for 660 km seismic discontinuity. *Earth and Planetary Science Letters*, *371*, 103–111.

Gurrola, H., Minster, J., & Owens, T. (1994). The use of velocity spectrum for stacking receiver functions and imaging upper mantle discontinuities. *Geophysical Journal International*, *117*(2), 427–440.

Hayes, G. P., Wald, D. J., & Johnson, R. L. (2012). Slab1. 0: A three-dimensional model of global subduction zone geometries. *Journal of Geophysical Research: Solid Earth*, *117*(B1).

Helffrich, G. (2000). Topography of the transition zone seismic discontinuities. *Reviews of Geophysics*, *38*(1), 141–158.

Hirose, K. (2002). Phase transitions in pyrolitic mantle around 670-km depth: Implications for upwelling of plumes from the lower mantle. *Journal of Geophysical Research: Solid Earth*, *107*(B4), ECV–3.

Houser, C. (2016). Global seismic data reveal little water in the mantle transition zone. *Earth and Planetary Science Letters*, *448*, 94–101.

Houser, C., Masters, G., Shearer, P., & Laske, G. (2008). Shear and compressional velocity models of the mantle from cluster analysis of long-period waveforms. *Geophysical Journal International*, *174*(1), 195–212.

Houser, C., & Williams, Q. (2010). Reconciling pacific 410 and 660 km discontinuity topography, transition zone shear velocity patterns, and mantle phase transitions. *Earth and Planetary Science Letters*, *296*(3-4), 255–266.

Irifune, T., Nishiyama, N., Kuroda, K., Inoue, T., Isshiki, M., Utsumi, W., . . . others (1998). The postspinel phase boundary in mg2sio4 determined by in situ x-ray diffraction. *Science*, *279*(5357), 1698–1700.

Ito, E., & Takahashi, E. (1989). Postspinel transformations in the system mg2sio4-fe2sio4 and some geophysical implications. *Journal of Geophysical Research: Solid Earth*, *94*(B8), 10637–10646.

Julian, B. R., & Anderson, D. L. (1968). Travel times, apparent velocities and amplitudes of body waves. *Bulletin of the Seismological Society of America*, *58*(1), 339–366.

Kanasewich, E., Hemmings, C., & Alpaslan, T. (1973). Nth-root stack nonlinear multichannel filter. *Geophysics*, *38*(2), 327–338.

Kaneshima, S. (2016). Seismic scatterers in the mid-lower mantle. *Physics of the Earth and Planetary Interiors*, *257*, 105–114.

Kaneshima, S. (2019). Seismic scatterers in the lower mantle near subduction zones. *Geophysical Journal International*, *219*(Supplement_1), S2–S20.

Kaneshima, S., & Helffrich, G. (1998). Detection of lower mantle scatterers northeast of the marianna subduction zone using short-period array data. *Journal of Geophysical Research: Solid Earth*, *103*(B3), 4825–4838.

Kaneshima, S., Kubo, T., & Yoshioka, S. (2012). Geophysical and mineralogical constraints on the post-spinel transformation for the tonga slab. *Physics of the Earth and Planetary Interiors*, *196*, 23–31.

Katsura, T., & Ito, E. (1989). The system mg2sio4-fe2sio4 at high pressures and temperatures: Precise determination of stabilities of olivine, modified spinel, and

spinel. *Journal of Geophysical Research: Solid Earth*, *94*(B11), 15663–15670.

Katsura, T., Yamada, H., Nishikawa, O., Song, M., Kubo, A., Shinmei, T., . . . others (2004). Olivine-wadsleyite transition in the system (mg, fe) 2sio4. *Journal of Geophysical Research: Solid Earth*, *109*(B2).

Kennett, B., & Engdahl, E. (1991). Traveltimes for global earthquake location and phase identification. *Geophysical Journal International*, *105*(2), 429–465.

Kennett, B. L., Engdahl, E., & Buland, R. (1995). Constraints on seismic velocities in the earth from traveltimes. *Geophysical Journal International*, *122*(1), 108–124.

Krischer, L., Megies, T., Barsch, R., Beyreuther, M., Lecocq, T., Caudron, C., & Wassermann, J. (2015). Obspy: A bridge for seismology into the scientific python ecosystem. *Computational Science & Discovery*, *8*(1), 014003.

Kubo, T., Kaneshima, S., Torii, Y., & Yoshioka, S. (2009). Seismological and experimental constraints on metastable phase transformations and rheology of the mariana slab. *Earth and Planetary Science Letters*, *287*(1-2), 12–23.

Lay, T., Williams, Q., & Garnero, E. J. (1998). The core–mantle boundary layer and deep earth dynamics. *Nature*, *392*(6675), 461–468.

Litasov, K., Ohtani, E., Sano, A., Suzuki, A., & Funakoshi, K. (2005b). In situ x-ray diffraction study of post-spinel transformation in a peridotite mantle: implication for the 660-km discontinuity. *Earth and Planetary Science Letters*, *238*(3-4), 311–328.

Litasov, K. D., Ohtani, E., Sano, A., Suzuki, A., & Funakoshi, K. (2005a). Wet subduction versus cold subduction. *Geophysical Research Letters*, *32*(13).

Lu, C., Grand, S. P., Lai, H., & Garnero, E. J. (2019). Tx2019slab: a new p and s tomography model incorporating subducting slabs. *Journal of Geophysical Research: Solid Earth*, *124*(11), 11549–11567.

Niu, F., & Kawakatsu, H. (1995). Direct evidence for the undulation of the 660-km discontinuity beneath tonga: Comparison of japan and california array data. *Geophysical research letters*, *22*(5), 531–534.

Niu, F., & Kawakatsu, H. (1997). Depth variation of the mid-mantle seismic disconti-

nuity. *Geophysical Research Letters*, *24*(4), 429–432.

Niu, F., Levander, A., Ham, S., & Obayashi, M. (2005). Mapping the subducting pacific slab beneath southwest japan with hi-net receiver functions. *Earth and Planetary Science Letters*, *239*(1-2), 9–17.

Obayashi, M., Yoshimitsu, J., Nolet, G., Fukao, Y., Shiobara, H., Sugioka, H., . . . Gao, Y. (2013). Finite frequency whole mantle p wave tomography: Improvement of subducted slab images. *Geophysical Research Letters*, *40*(21), 5652–5657.

Okino, K., Ando, M., Kaneshima, S., & Hirahara, K. (1989). The horizontally lying slab. *Geophysical Research Letters*, *16*(9), 1059–1062.

Revenaugh, J., & Jordan, T. H. (1987). Observations of first-order mantle reverberations. *Bulletin of the Seismological Society of America*, *77*(5), 1704–1717.

Revenaugh, J., & Jordan, T. H. (1989). A study of mantle layering beneath the western pacific. *Journal of Geophysical Research: Solid Earth*, *94*(B5), 5787–5813.

Richards, M. A., & Wicks Jr, C. W. (1990). Sp conversions from the transition zone beneath tonga and the nature of the 670 km discontinuity. *Geophysical Journal International*, *101*(1), 1–35.

Ringwood, A., & Major, A. (1966). High-pressure transformations in pyroxenes. *Earth and Planetary Science Letters*, *1*(5), 351–357.

Shearer, P. M. (1990). Seismic imaging of upper-mantle structure with new evidence for a 520-km discontinuity. *Nature*, *344*(6262), 121–126.

Shearer, P. M. (1991). Constraints on upper mantle discontinuities from observations of long-period reflected and converted phases. *Journal of Geophysical Research: Solid Earth*, *96*(B11), 18147–18182.

Shearer, P. M. (1993). Global mapping of upper mantle reflectors from long-period ss precursors. *Geophysical Journal International*, *115*(3), 878–904.

Shearer, P. M., & Flanagan, M. P. (1999). Seismic velocity and density jumps across the 410-and 660-kilometer discontinuities. *Science*, *285*(5433), 1545–1548.

Shearer, P. M., & Masters, T. G. (1992). Global mapping of topography on the 660-km discontinuity. *Nature*, *355*(6363), 791–796.

Shen, Y., Solomon, S. C., Bjarnason, I. T., & Wolfe, C. J. (1998). Seismic evidence for a lower-mantle origin of the iceland plume. *Nature*, *395*(6697), 62–65.

Simmons, N. A., Forte, A. M., & Grand, S. P. (2009). Joint seismic, geodynamic and mineral physical constraints on three-dimensional mantle heterogeneity: Implications for the relative importance of thermal versus compositional heterogeneity. *Geophysical Journal International*, *177*(3), 1284–1304.

Wessel, P., & Smith, W. H. (1995). New version of the generic mapping tools. *Eos, Transactions American Geophysical Union*, *76*(33), 329–329.

Wicks, C. W., & Richards, M. A. (1993). A detailed map of the 660-kilometer discontinuity beneath the izu-bonin subduction zone. *Science*, *261*(5127), 1424–1427.

Wood, B. J. (1989). Mineralogical phase change at the 670-km discontinuity. *Nature*, *341*(6240), 278–278.

8 Appendix

Events figures (vespagrams) which S660P are observed in Kurile Region:
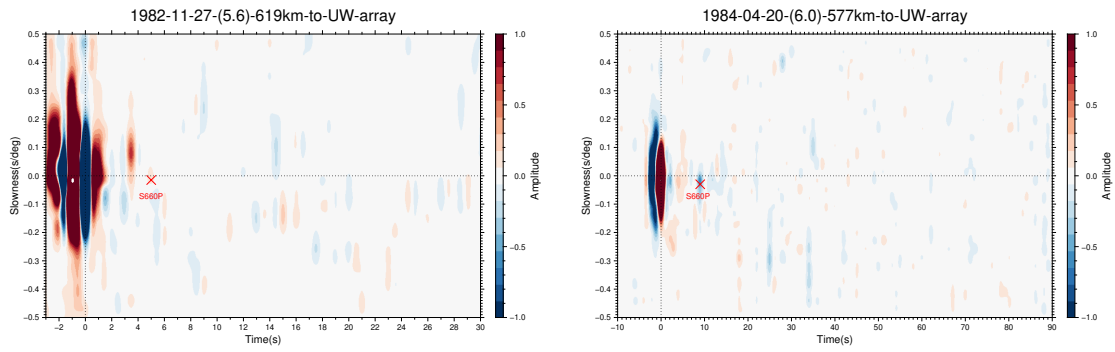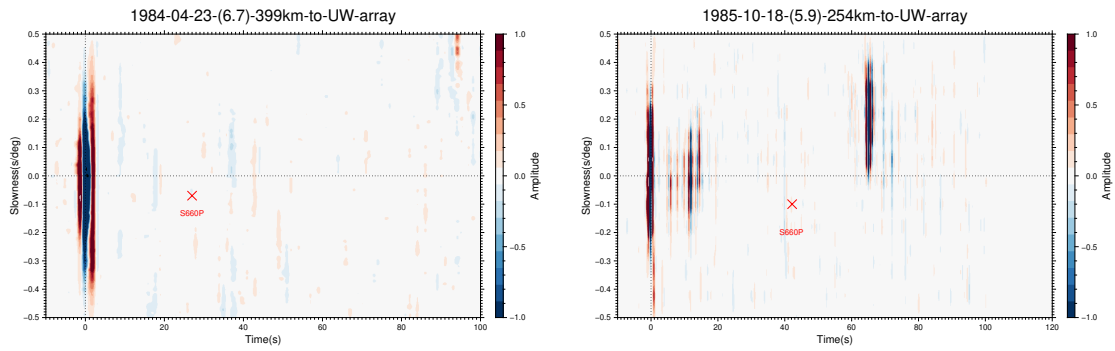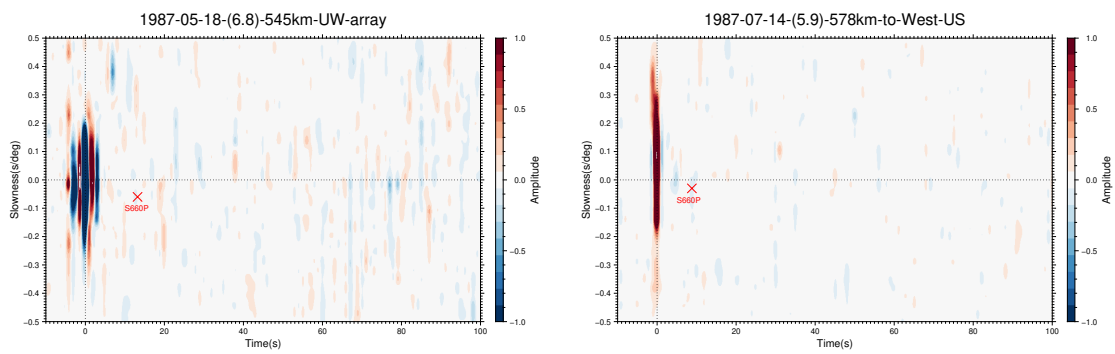
Figure 20: Events which S660P are observed in Kurile region.
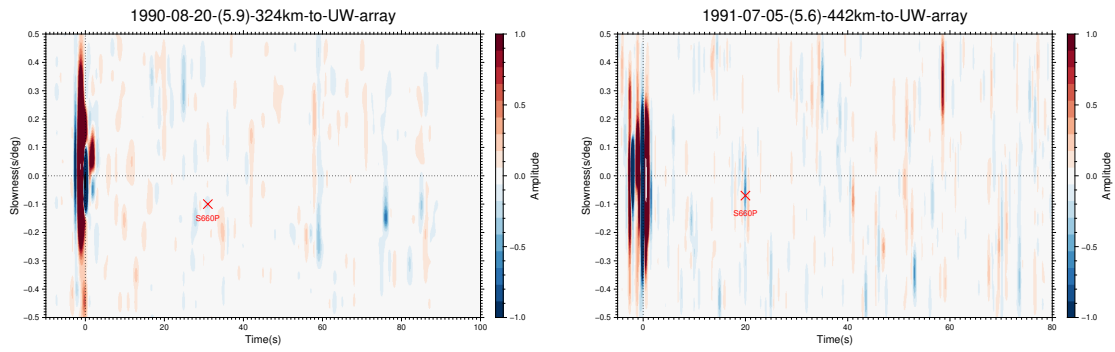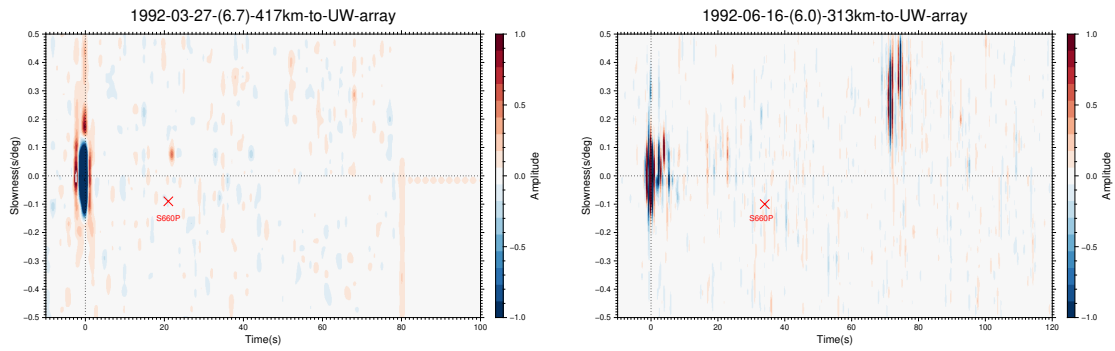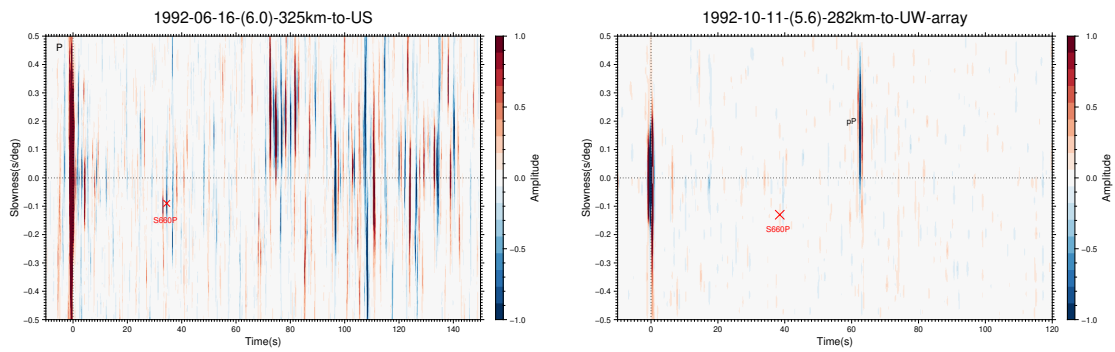
Figure 21: Events which S660P are observed.(Continue)
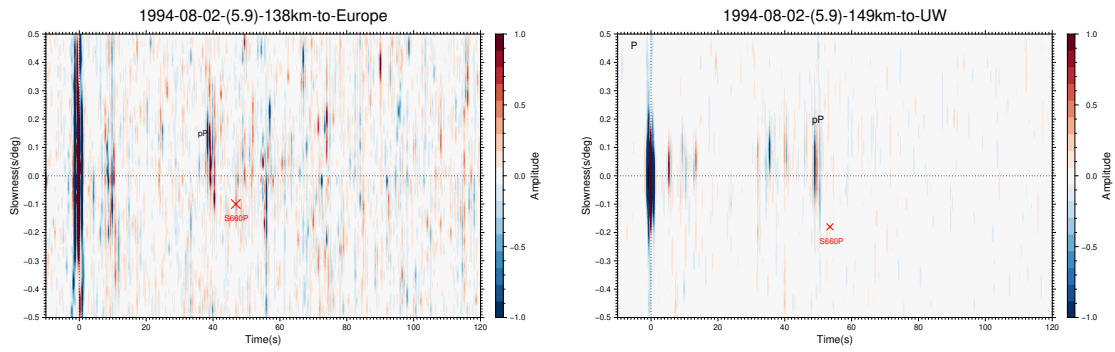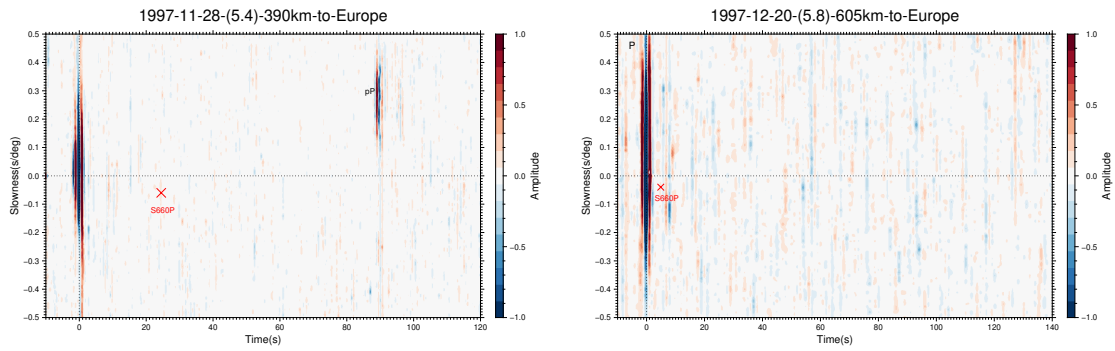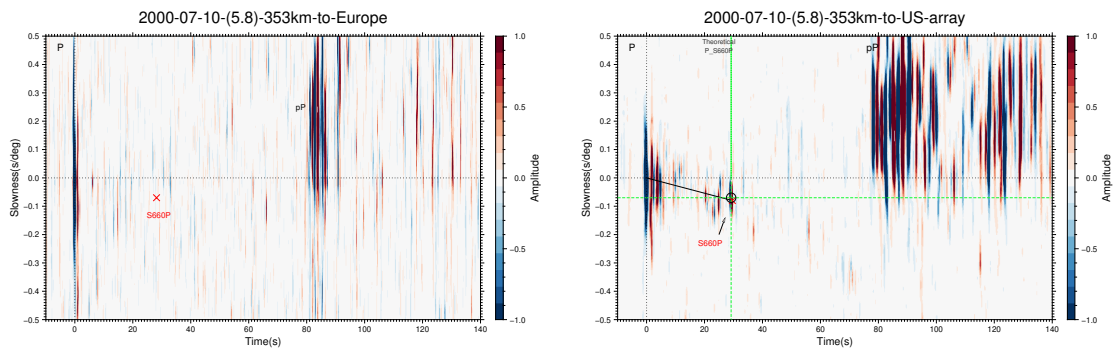
Figure 22: Events which S660P are observed.(Continue)
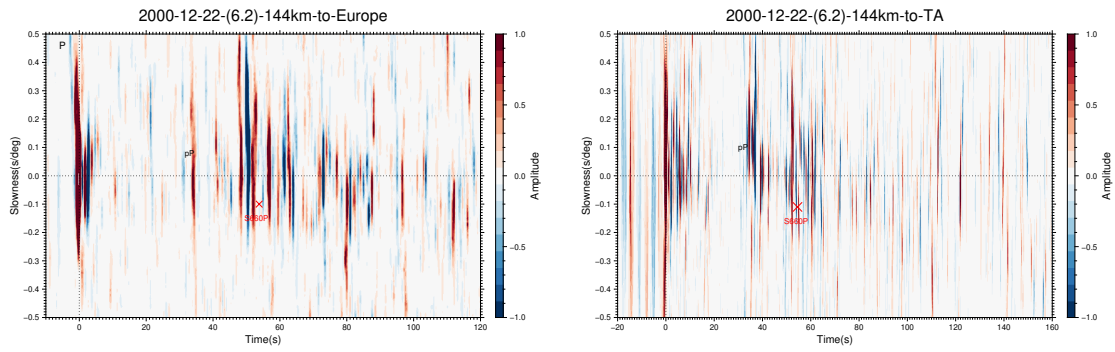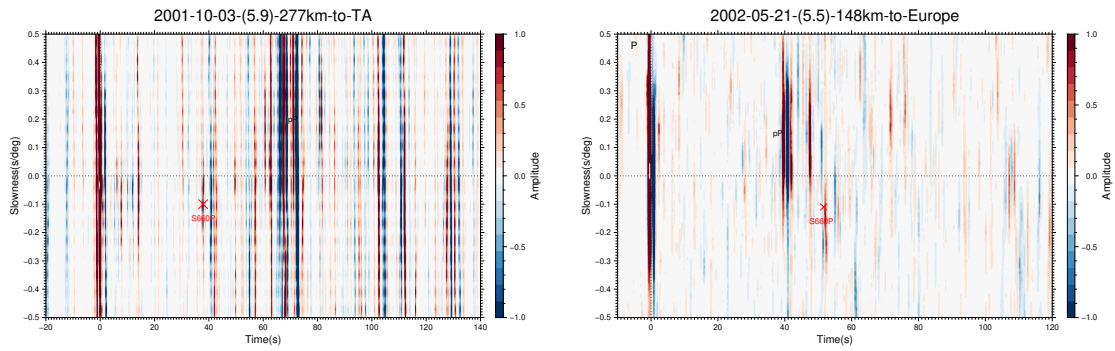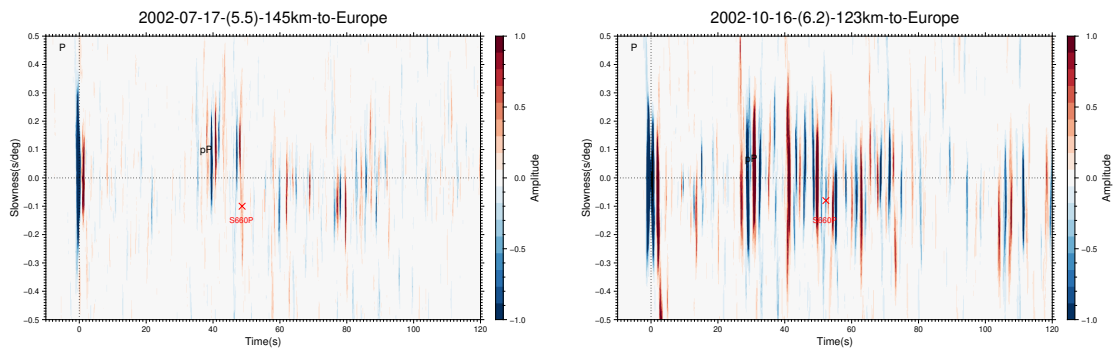
Figure 23: Events which S660P are observed.(Continue)
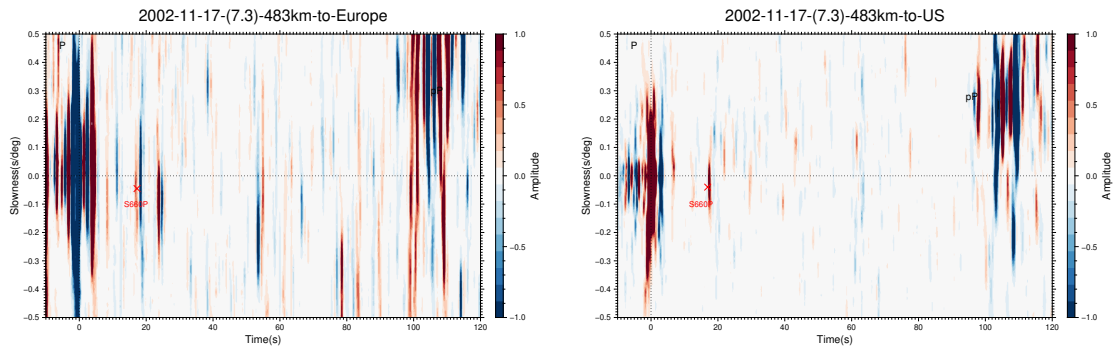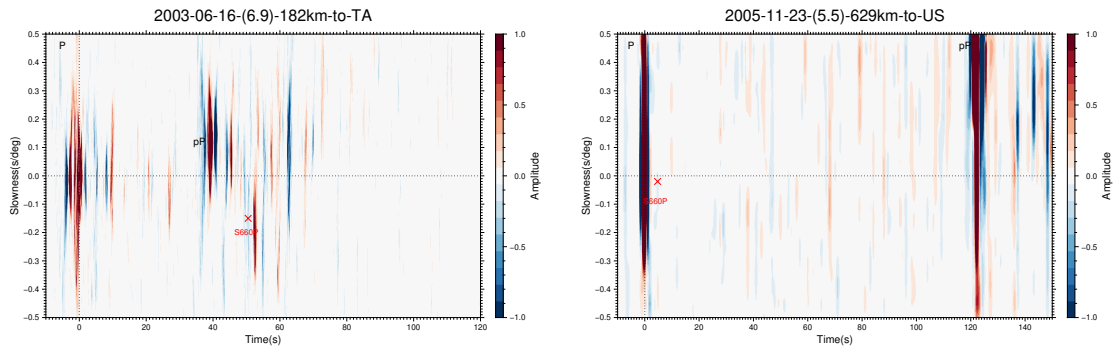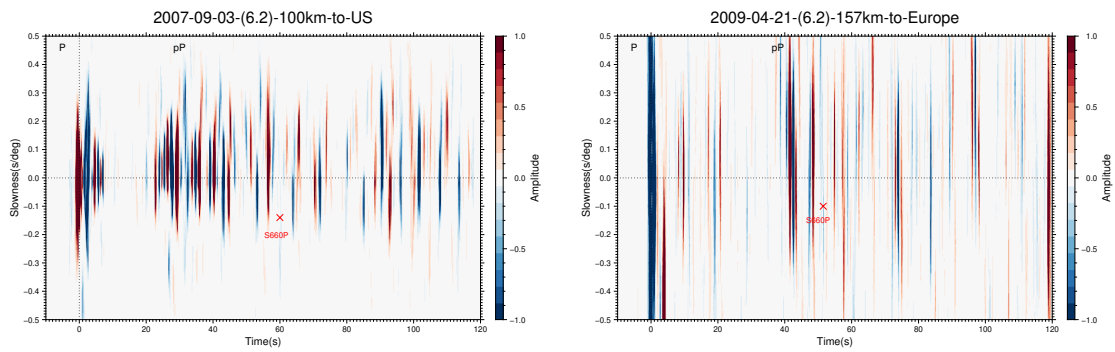
Figure 24: Events which S660P are observed.(Continue)
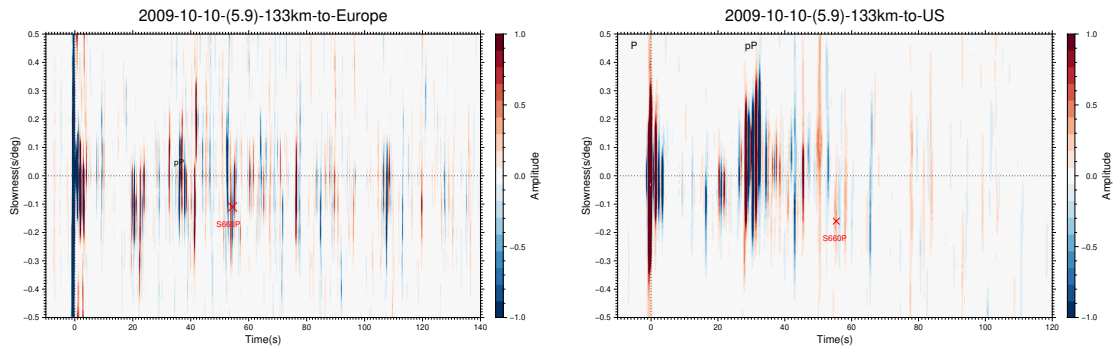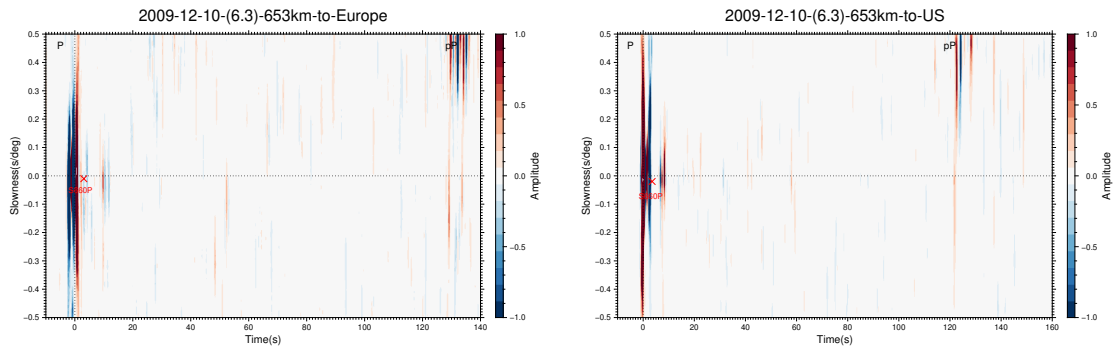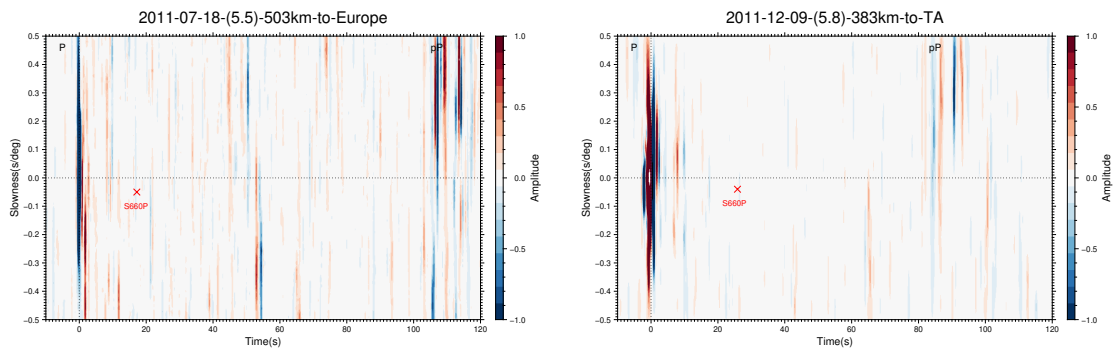
Figure 25: Events which S660P are observed.(Continue)
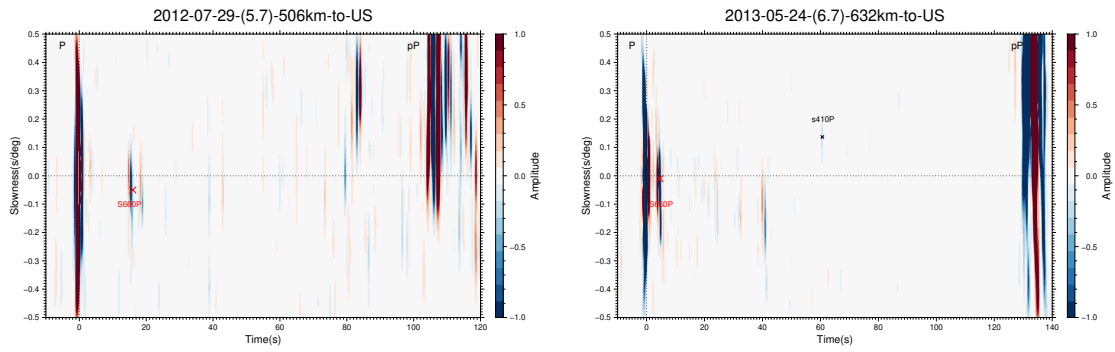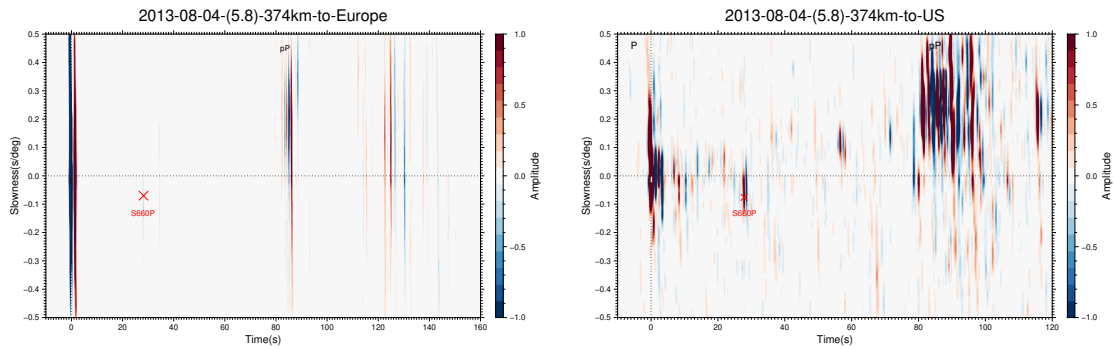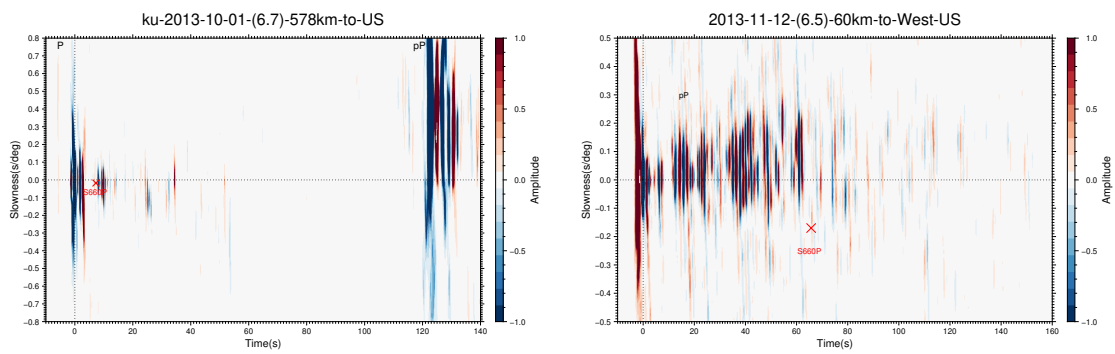
Figure 26: Events which S660P are observed.(Continue)

74
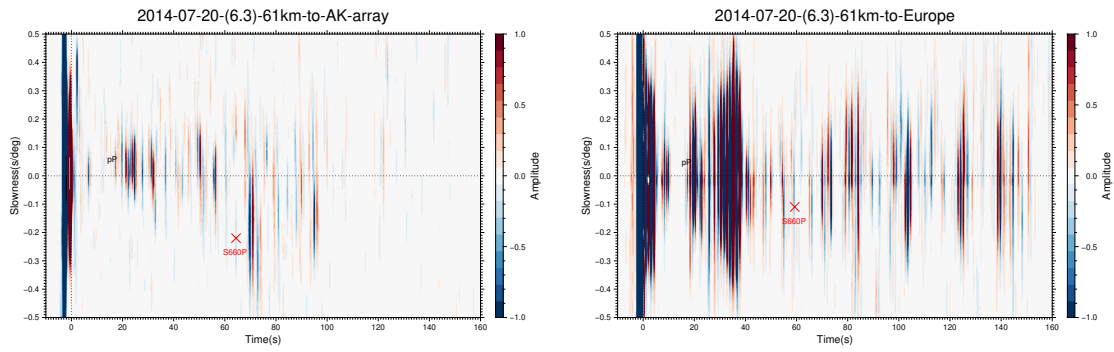
(a)
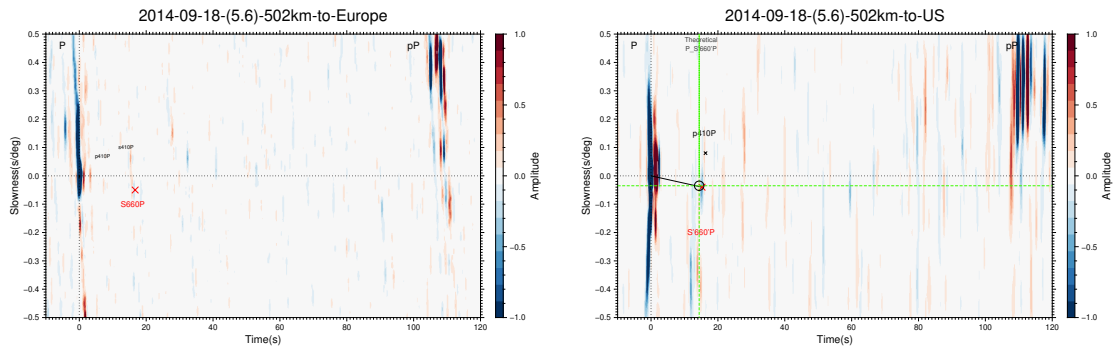
(b)
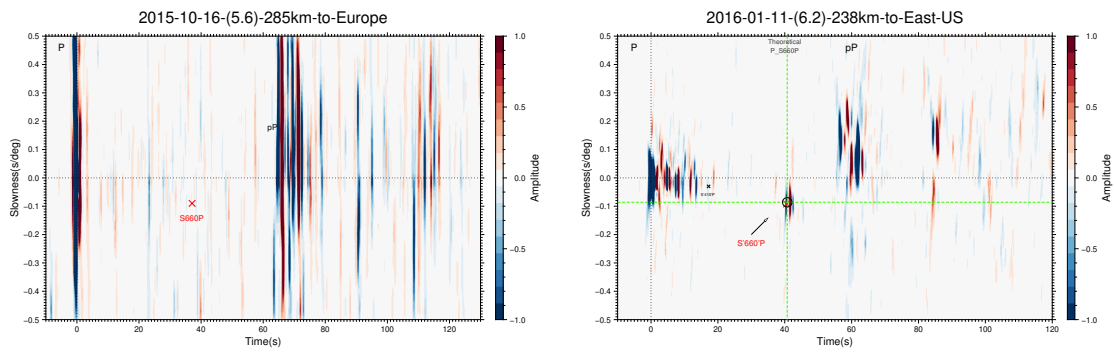
(c)

Figure 27: Events which S660P are observed.(Continue)
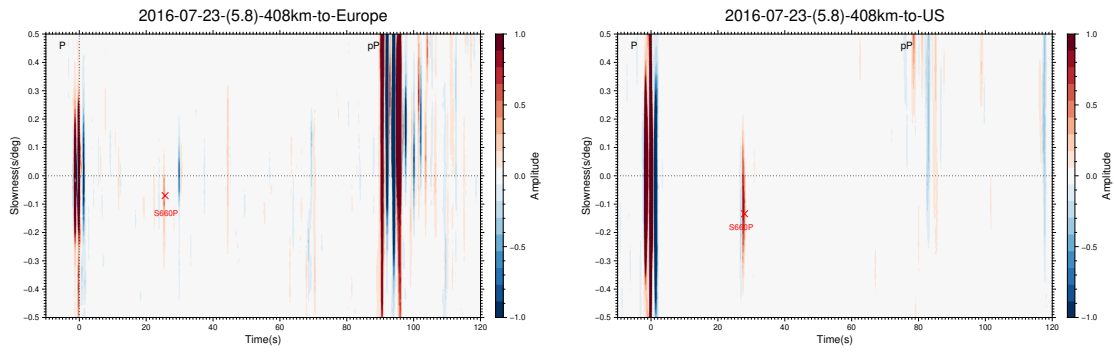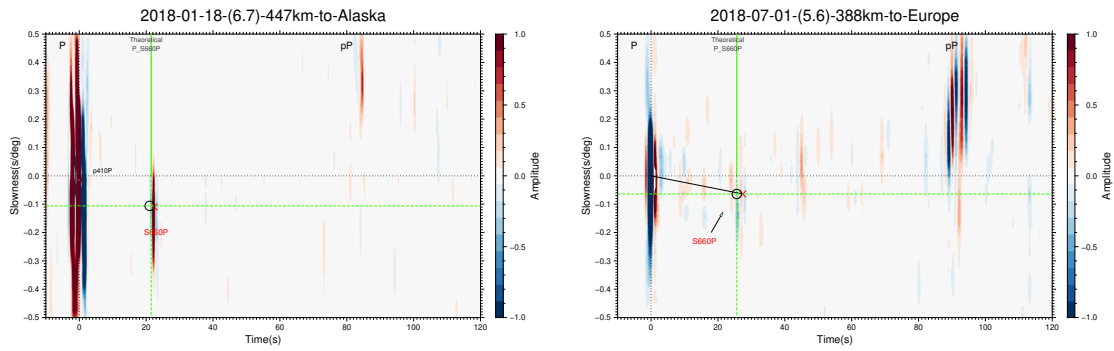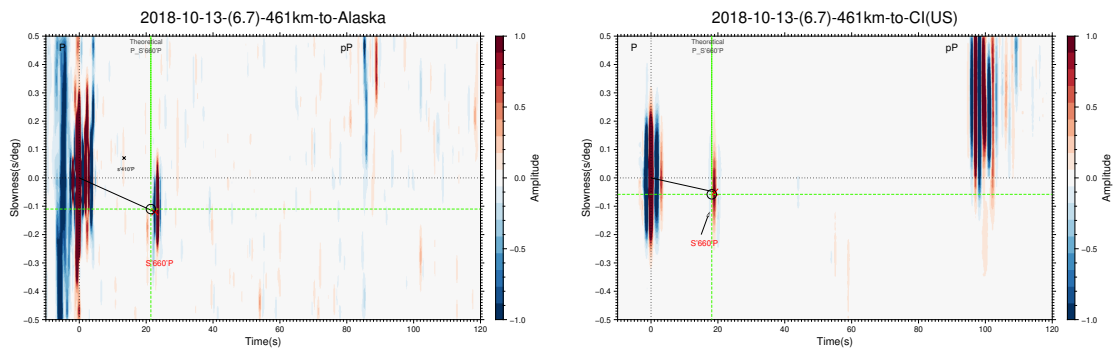
Figure 28: Events which S660P are observed.(Continue)
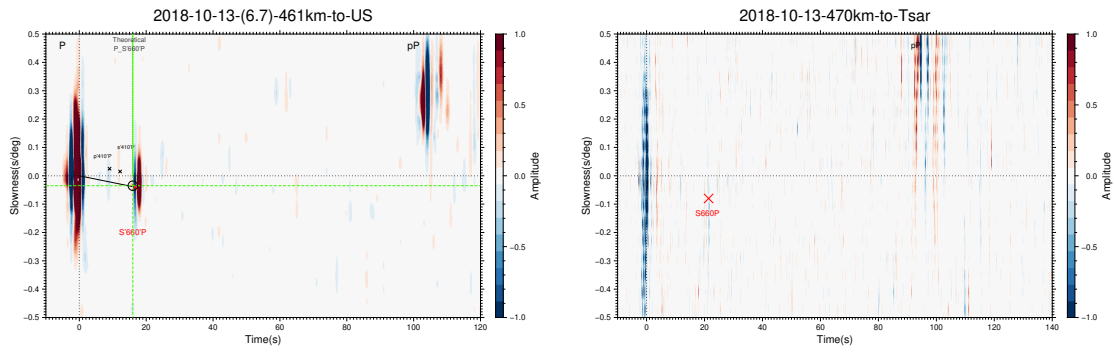
(a)
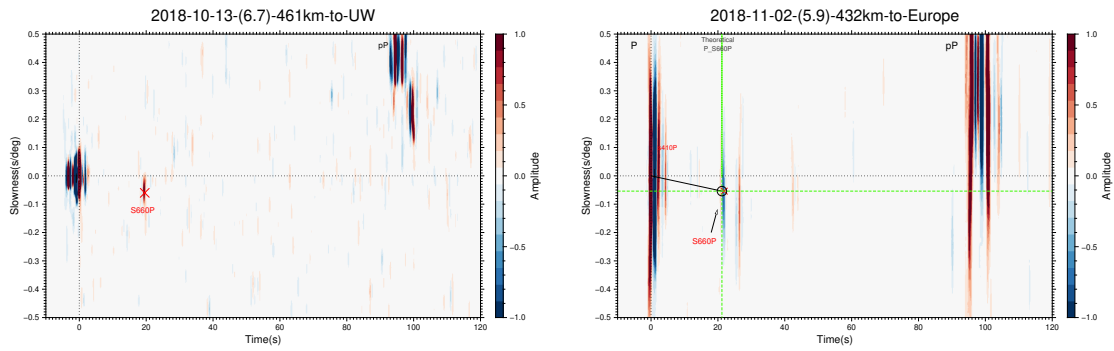
(b)
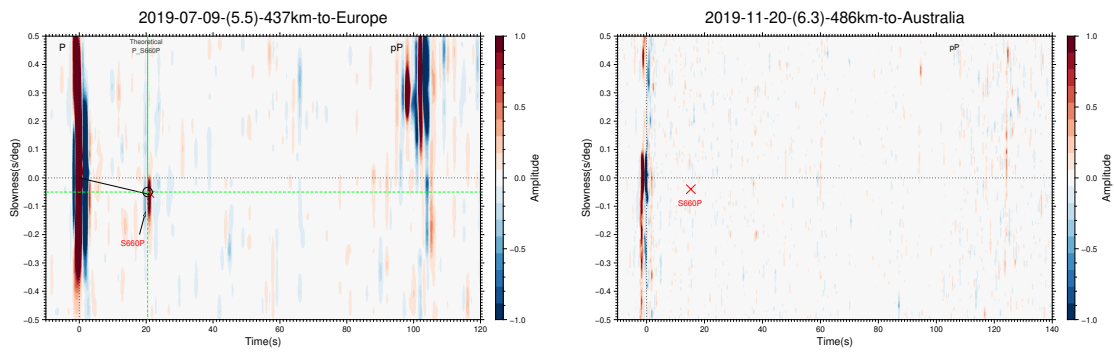
(c)

Figure 29: Events which S660P are observed.(Continue)
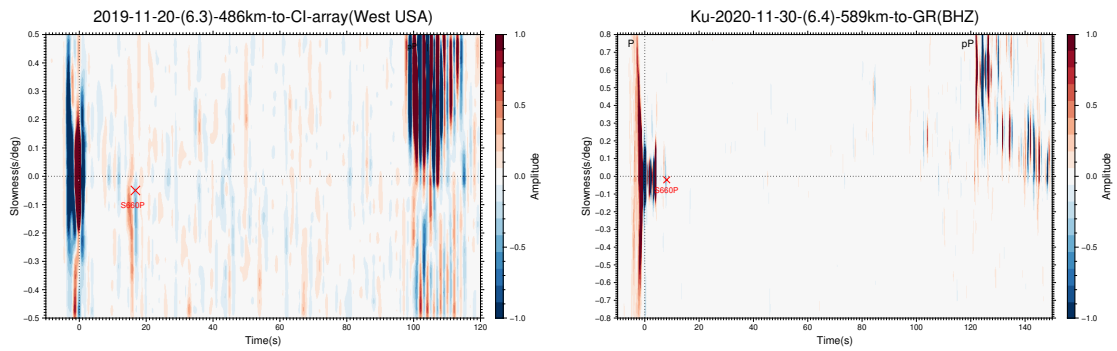
(a)
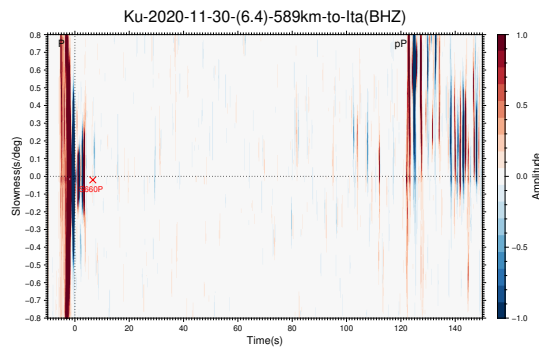
(b)

Figure 30: Events which S660P are observed.(Continue)

Events figures (vespagrams) which S660P are observed in Izu-Bonin Region:
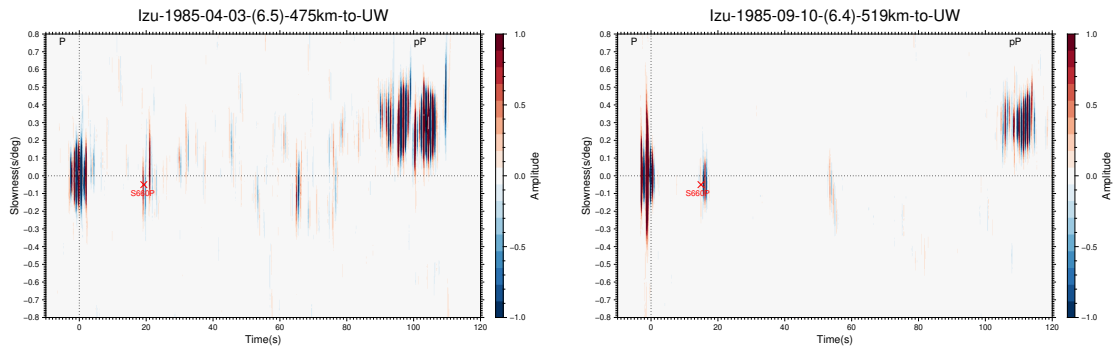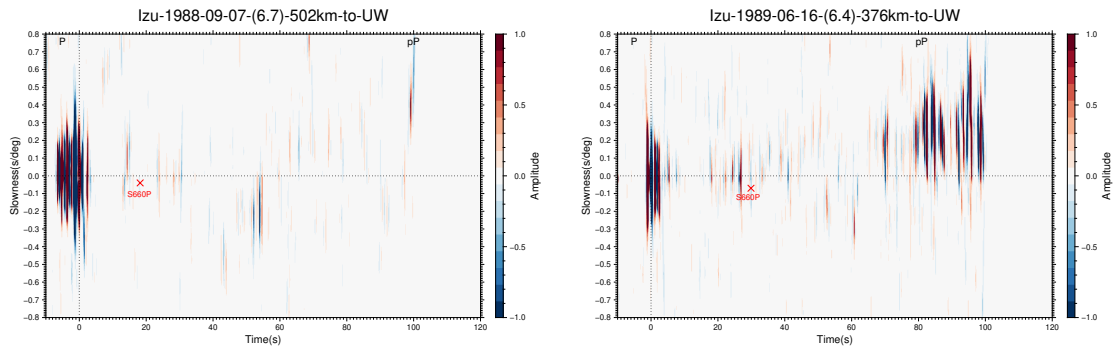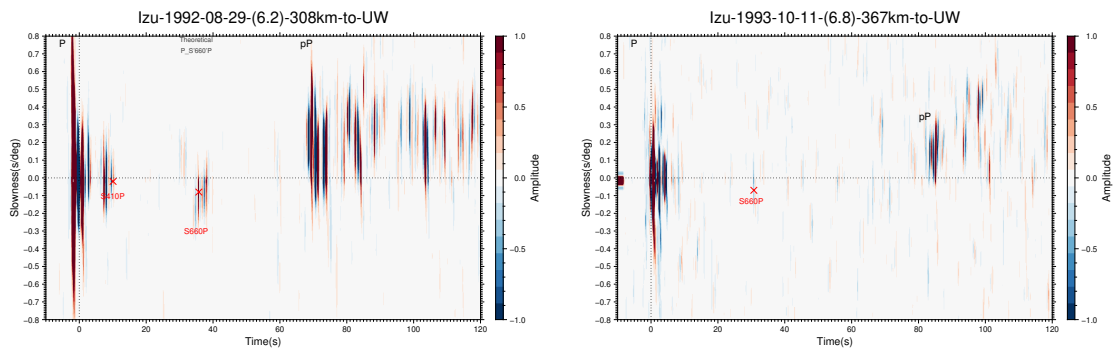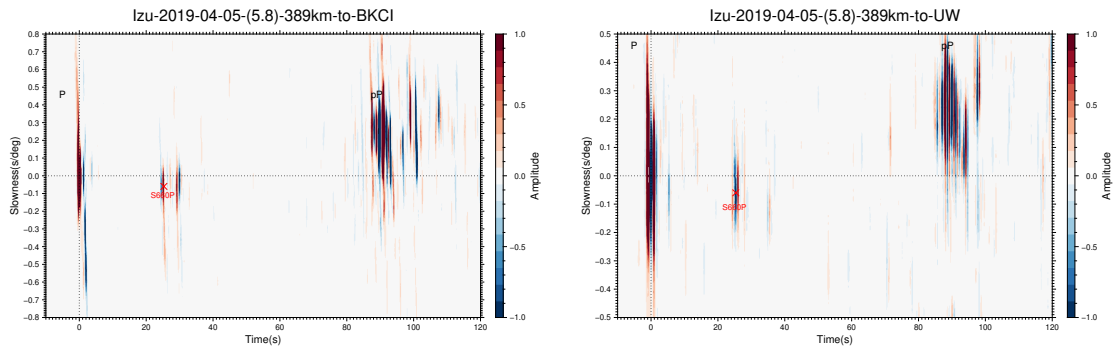
Figure 31: Events which S660P are observed in Izu-Bonin region.
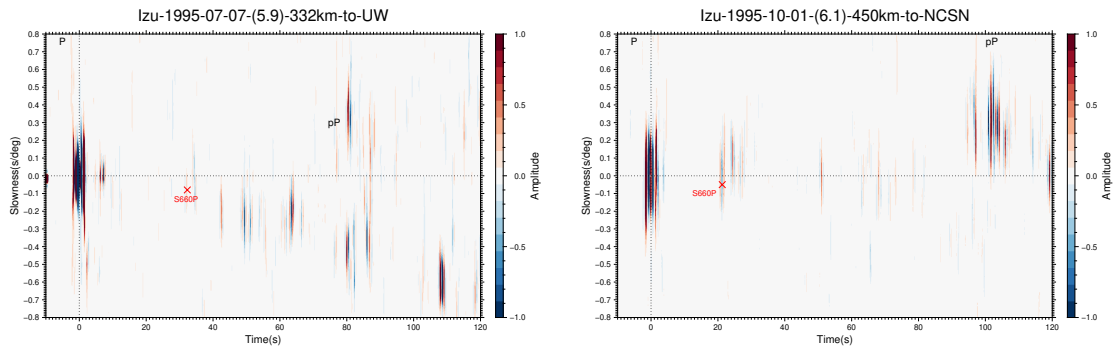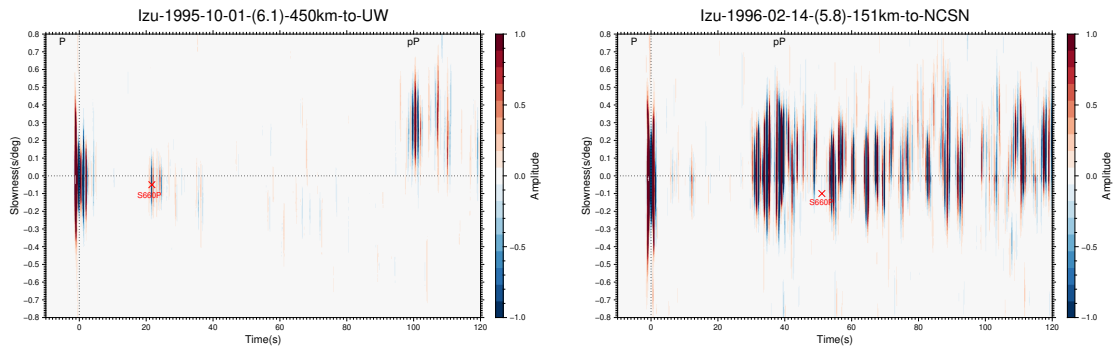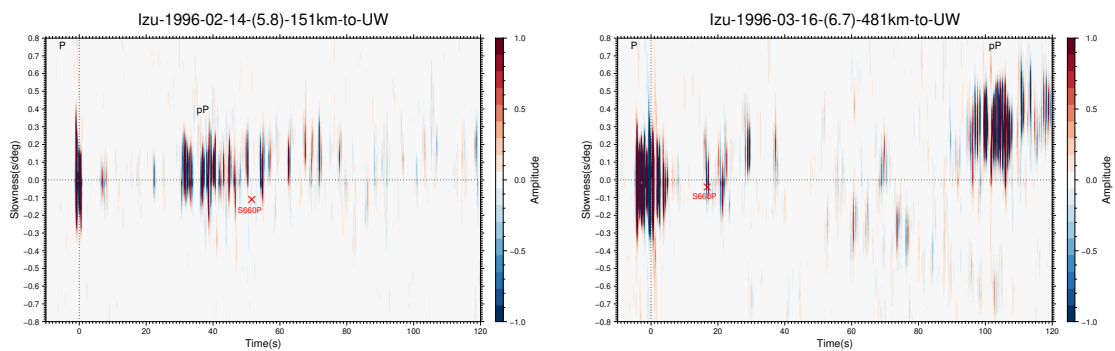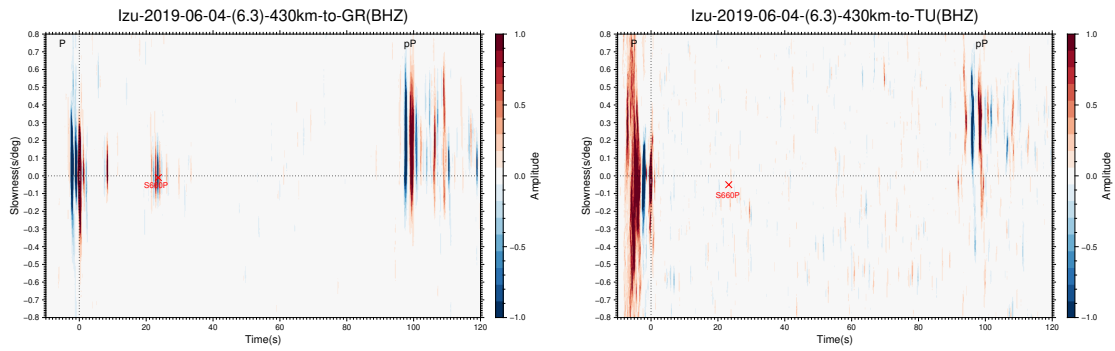
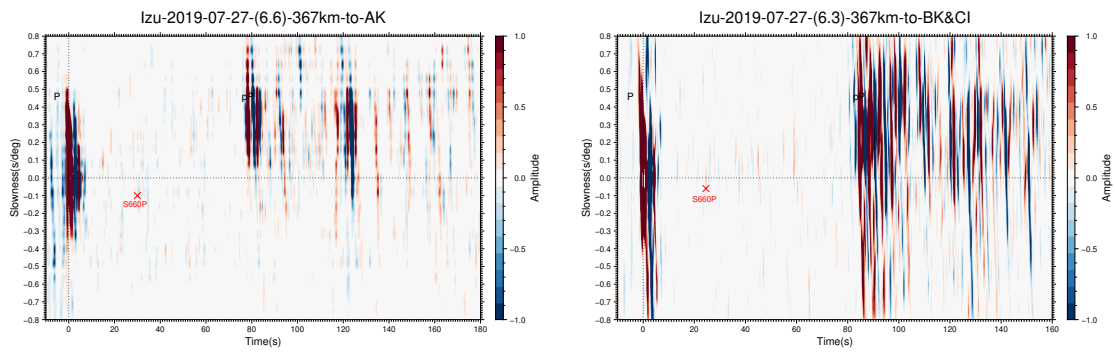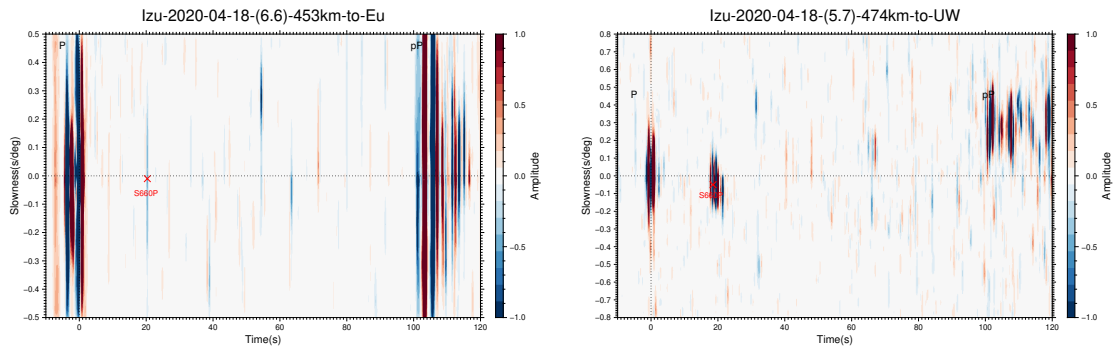Figure 32: Events which S660P are observed in Izu-Bonin region.(Continued)
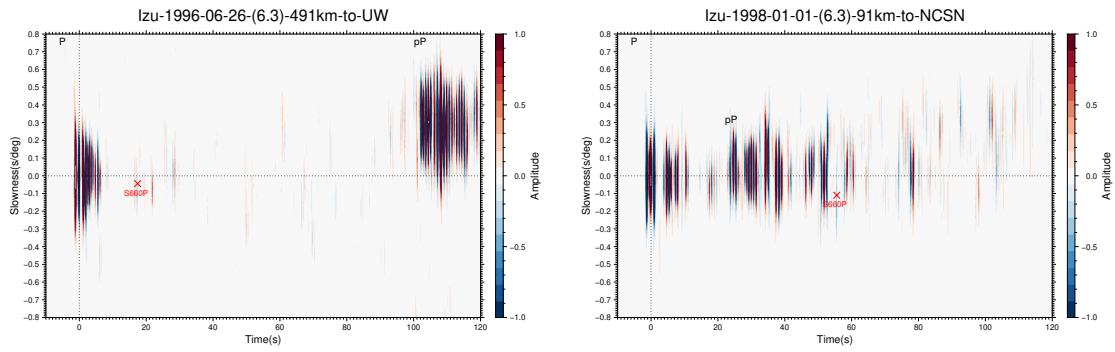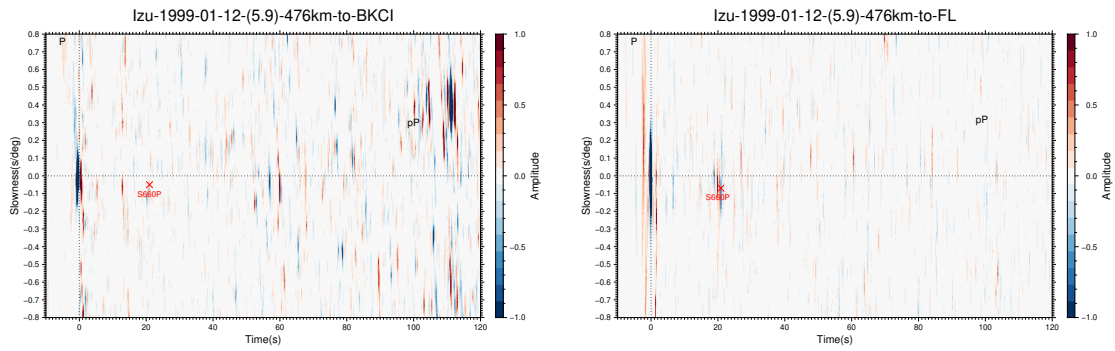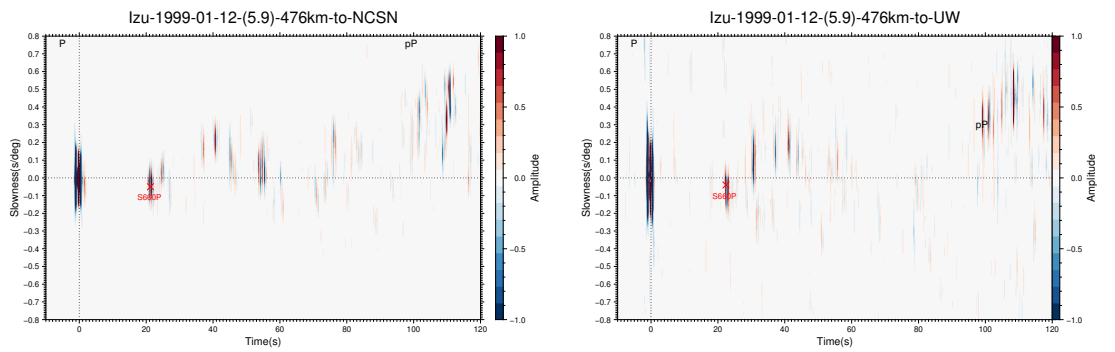
Figure 33: Events which S660P are observed in Izu-Bonin region.(Continued)
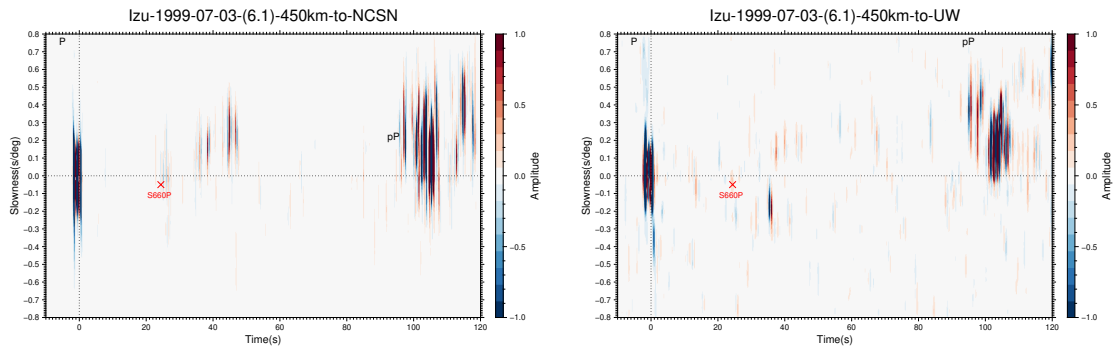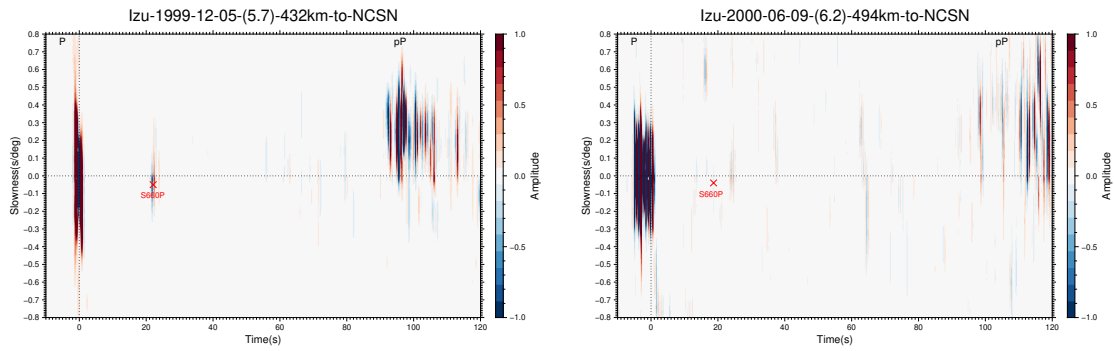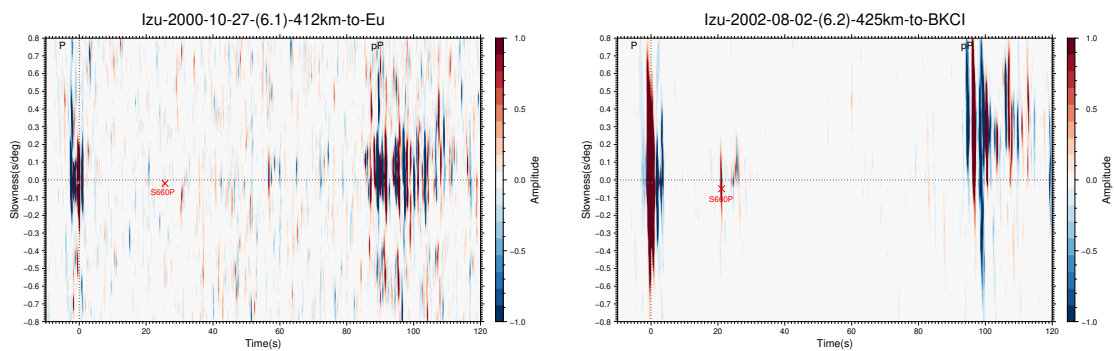
Figure 34: Events which S660P are observed in Izu-Bonin region.(Continued)
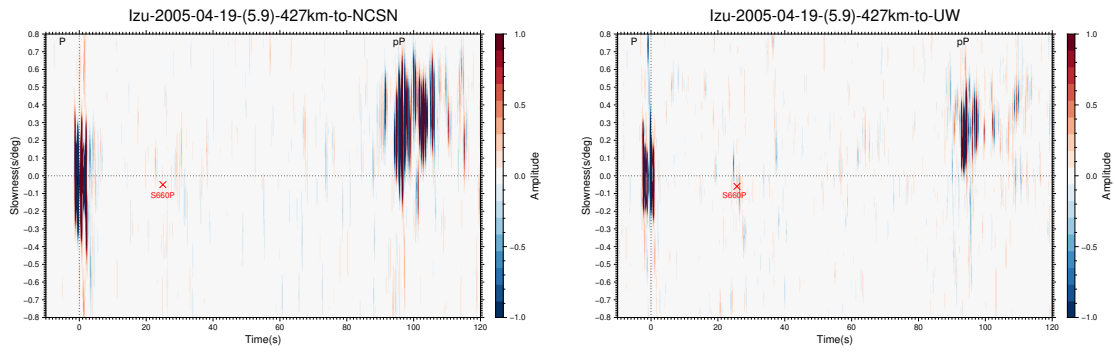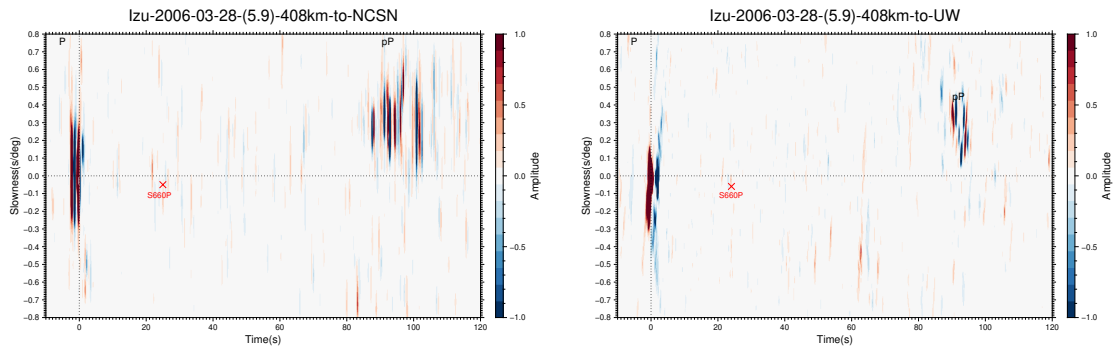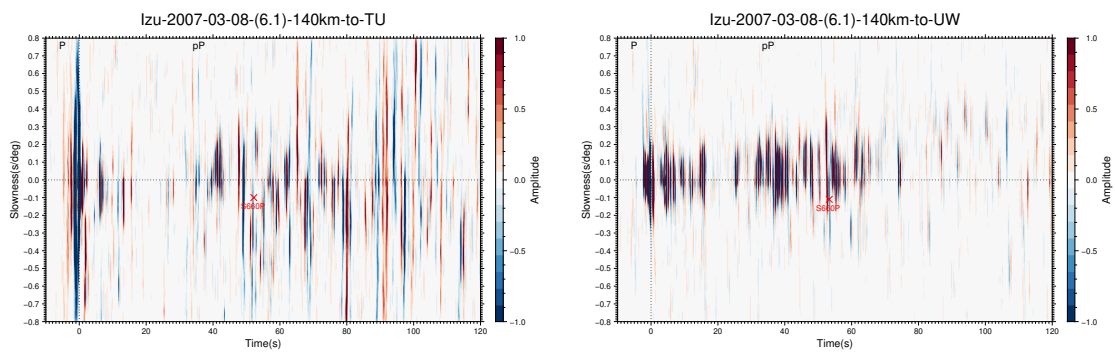
Figure 35: Events which S660P are observed in Izu-Bonin region.(Continued)
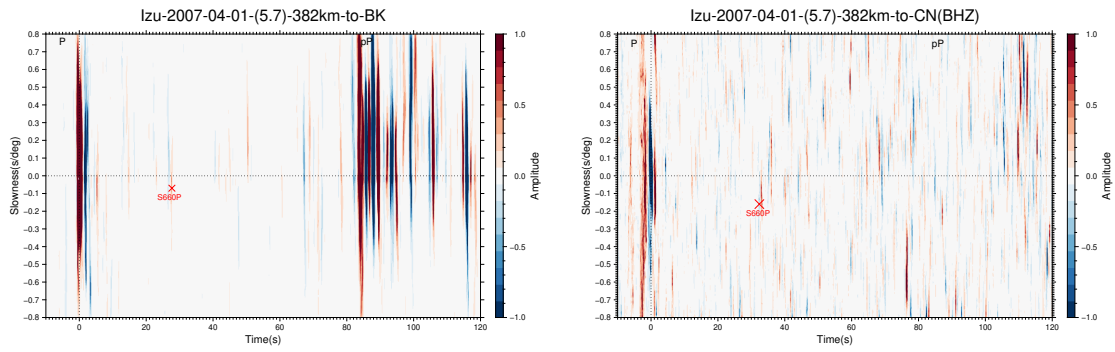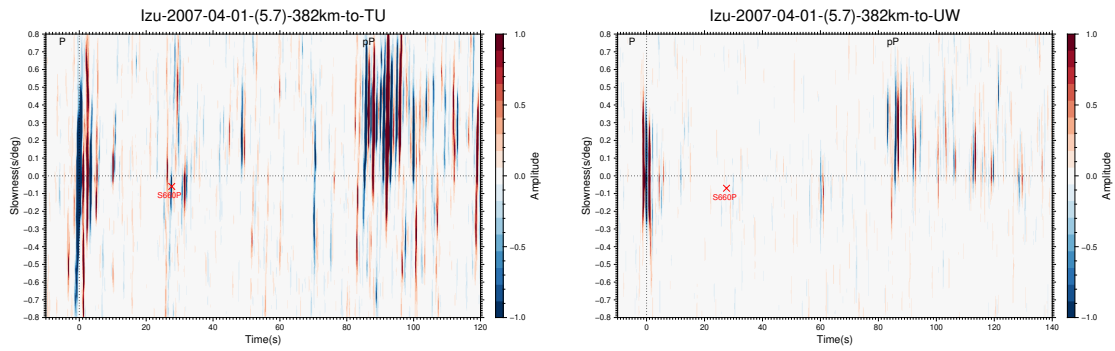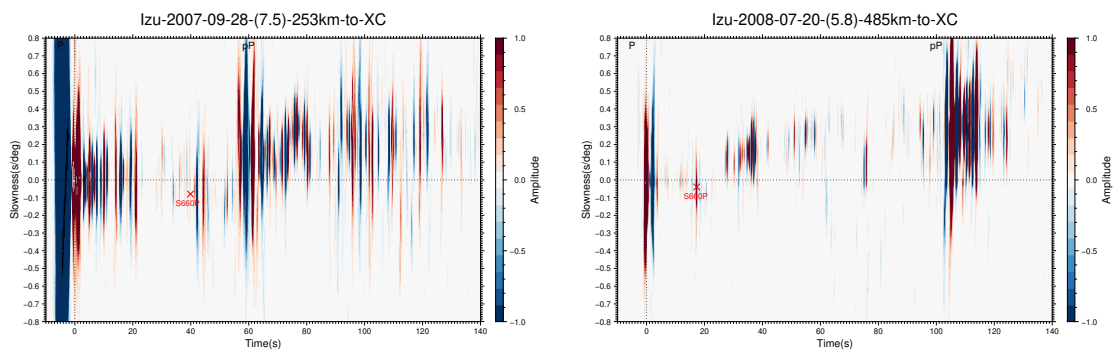
Figure 36: Events which S660P are observed in Izu-Bonin region.(Continued)
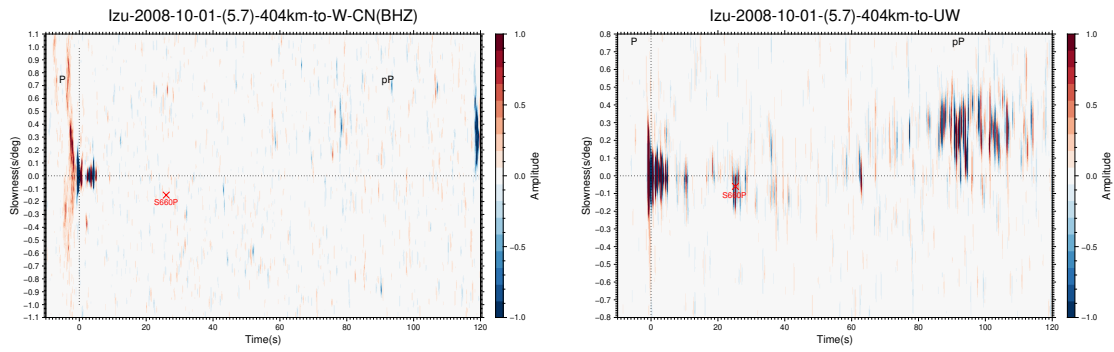
(a)
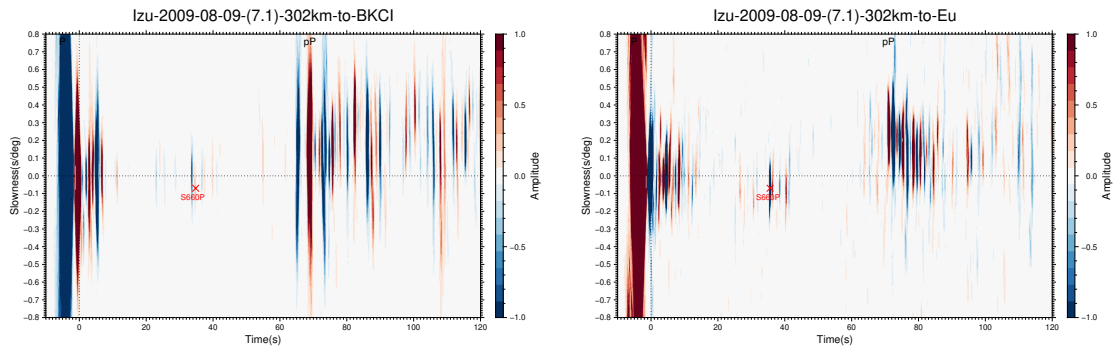
(b)
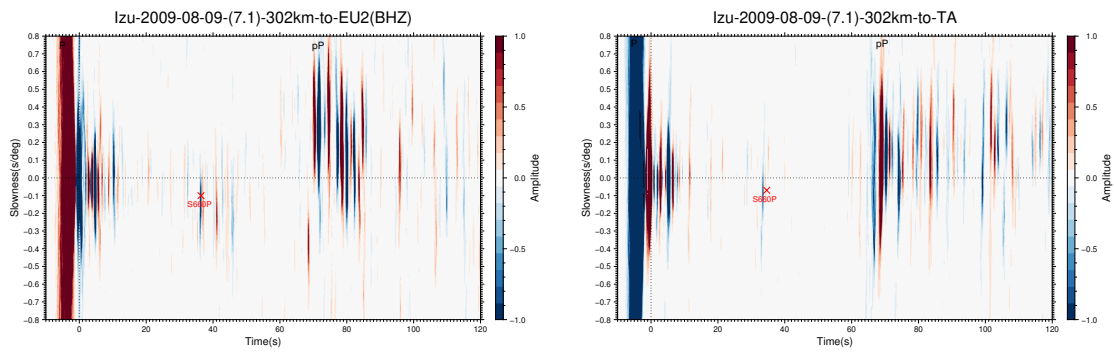
(c)

Figure 37: Events which S660P are observed in Izu-Bonin region.(Continued)
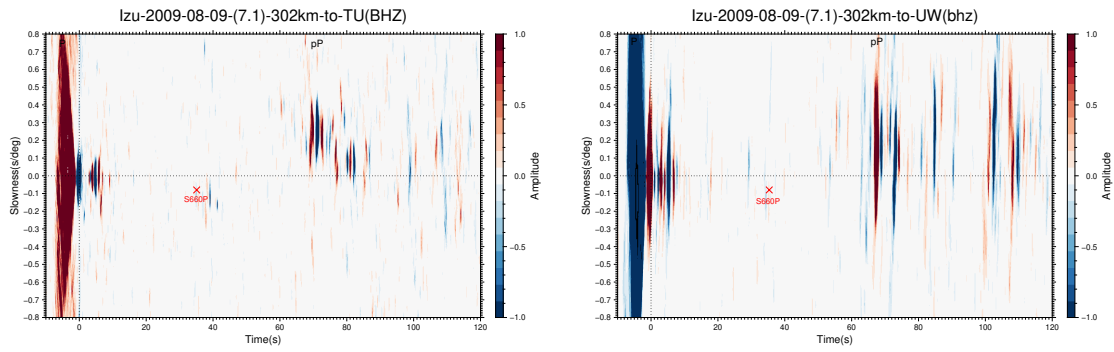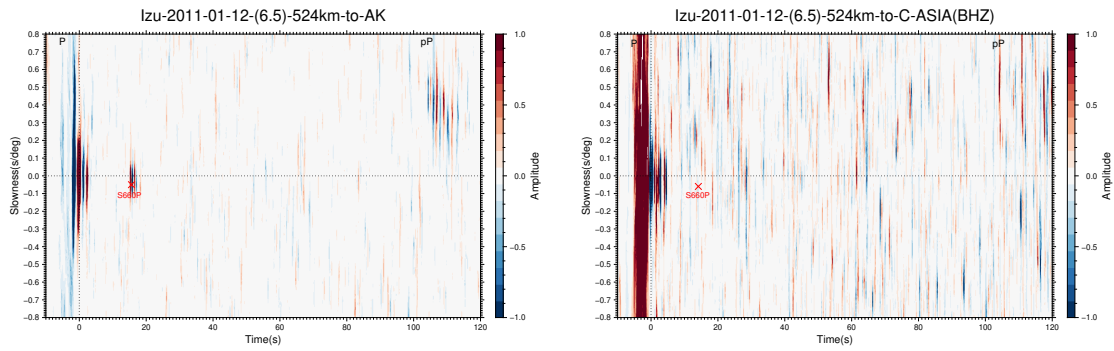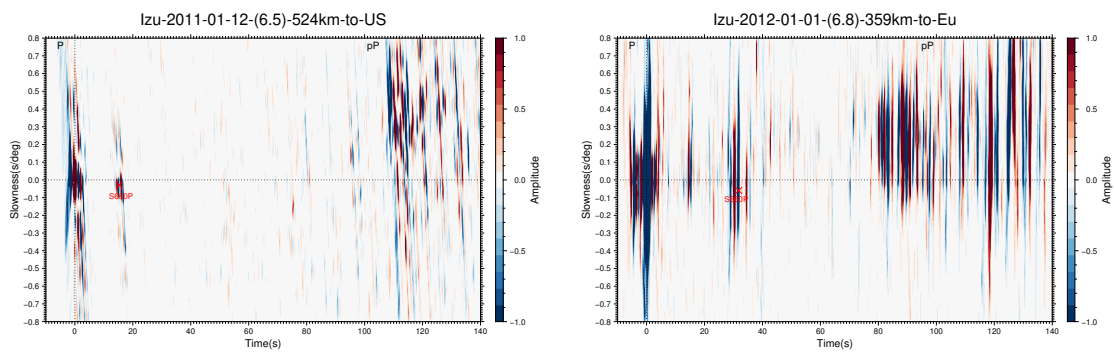
Figure 38: Events which S660P are observed in Izu-Bonin region.(Continued)
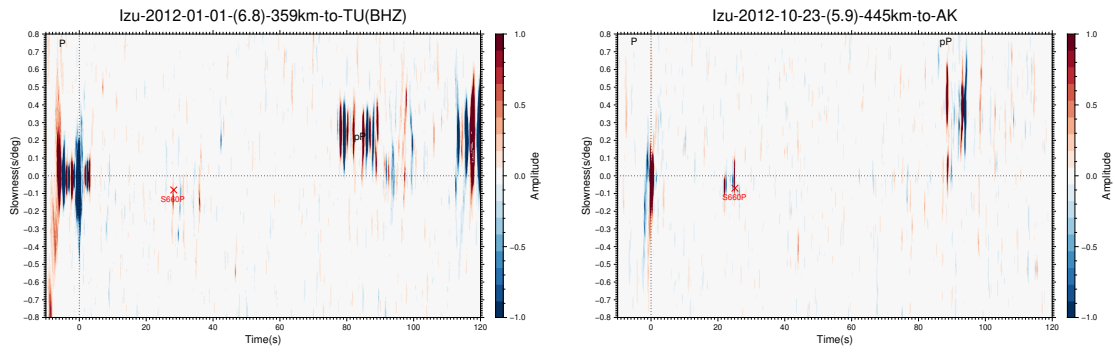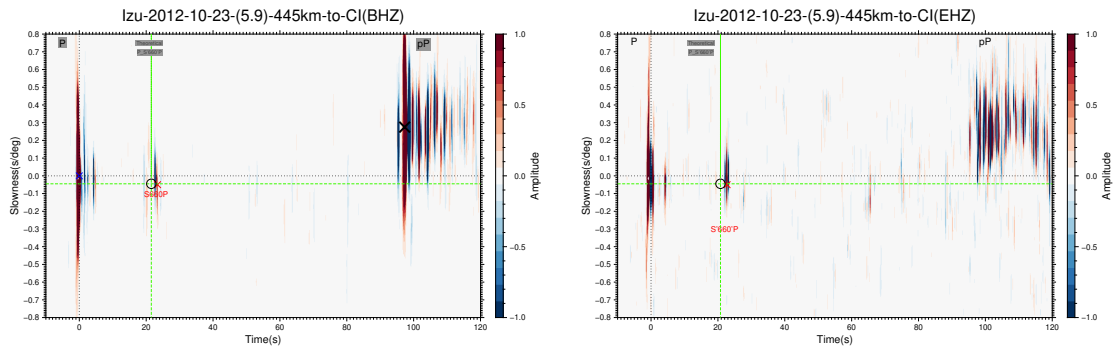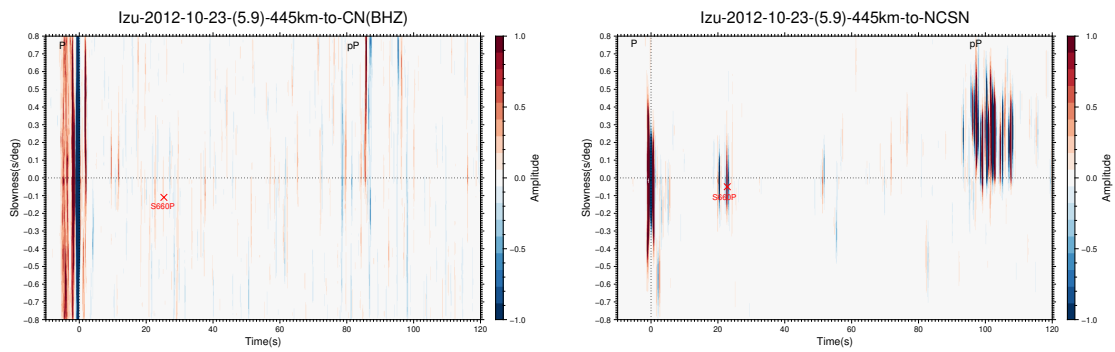
Figure 39: Events which S660P are observed in Izu-Bonin region.(Continued)
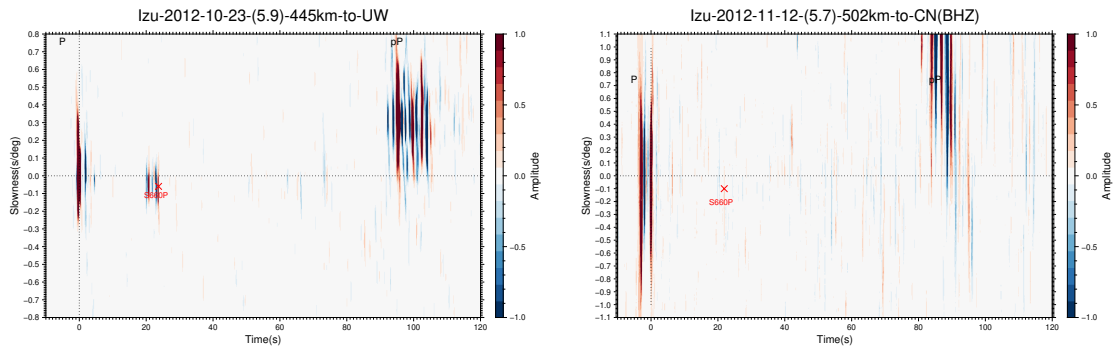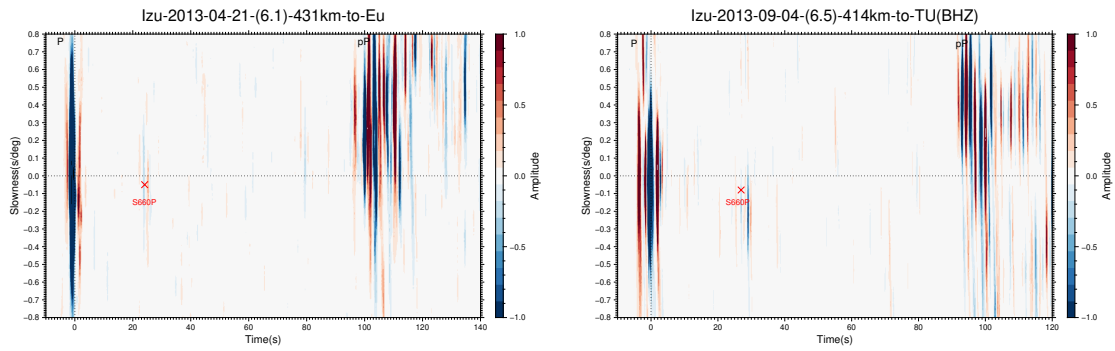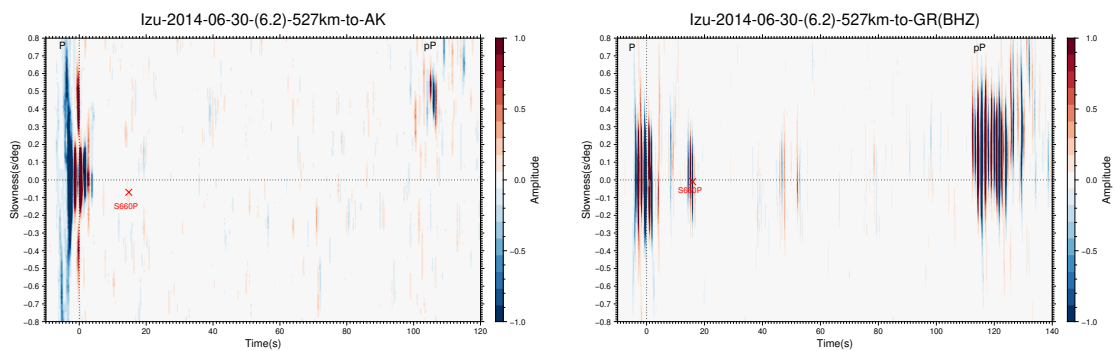
Figure 40: Events which S660P are observed in Izu-Bonin region.(Continued)
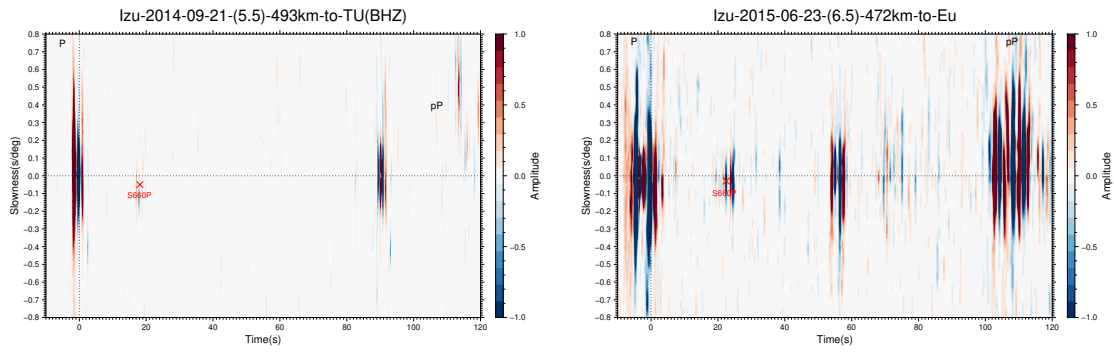
(a)
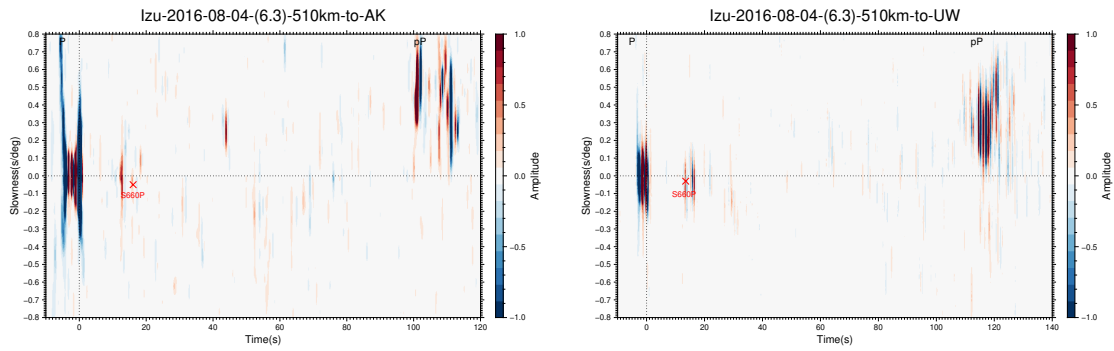
(b)
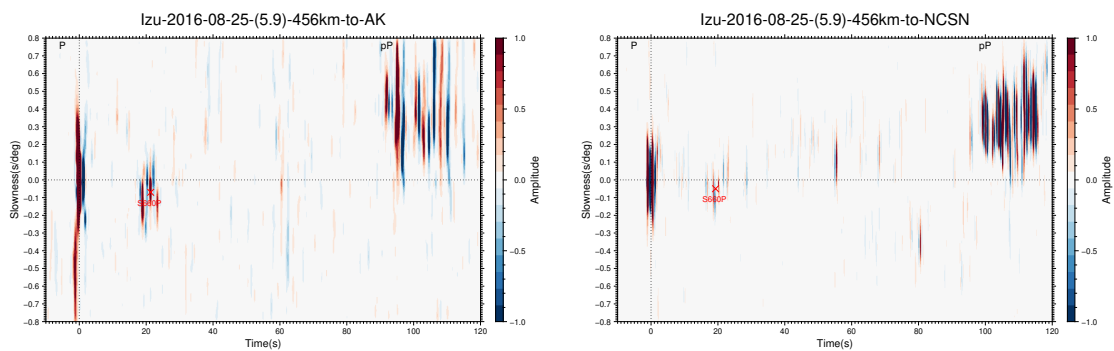
(c)

Figure 41: Events which S660P are observed in Izu-Bonin region.(Continued)
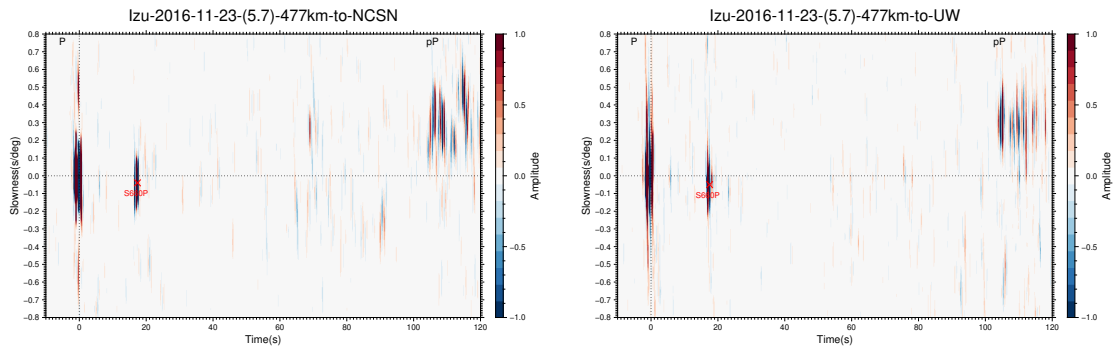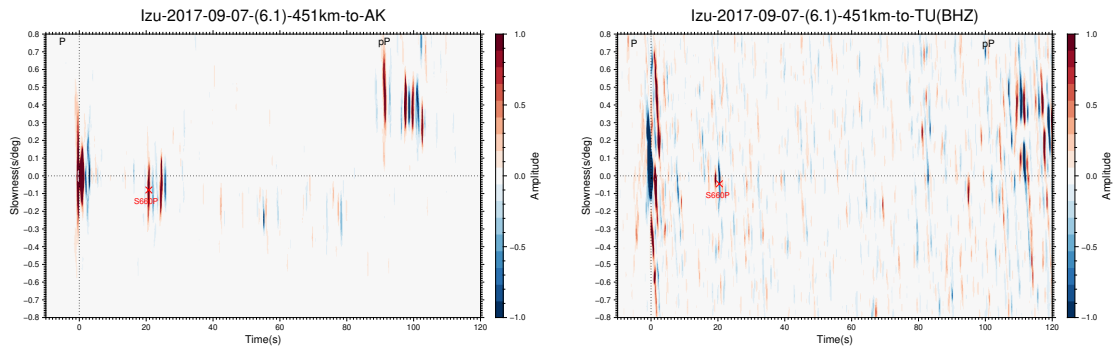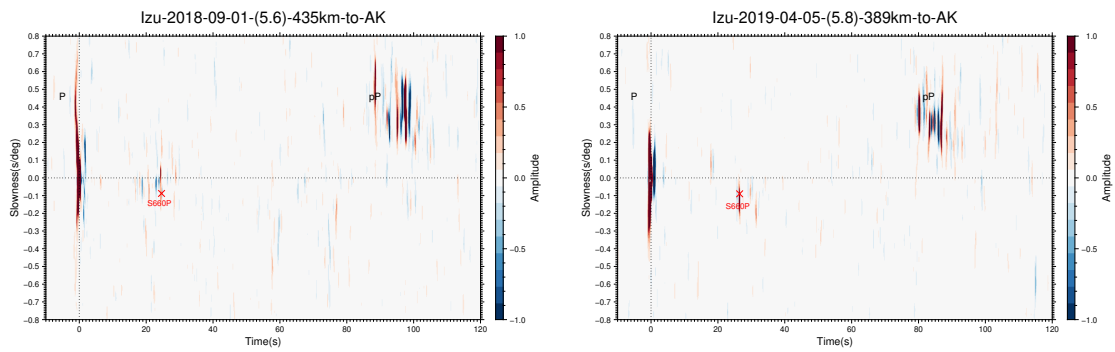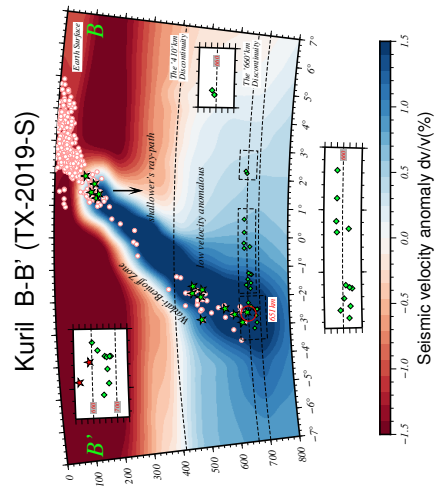
Figure 42: Events which S660P are observed in Izu-Bonin region.(Continued)

Figure 43: Events which S660P are observed in Izu-Bonin region.(Continued)

Figure 44: Events which S660P are observed in Izu-Bonin region.(Continued)
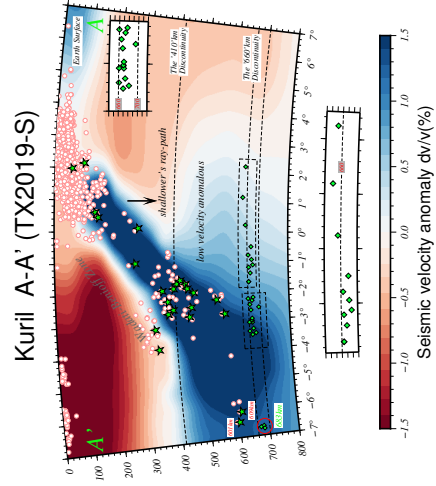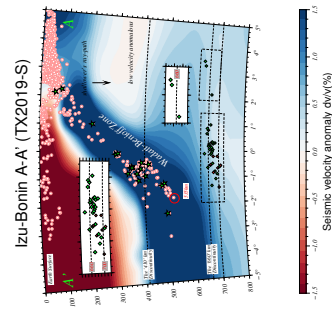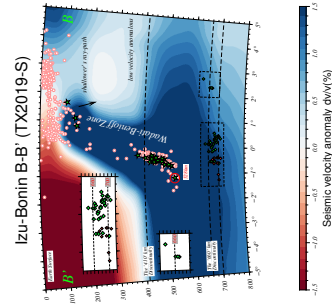
(a)

(b)

Figure 45: S-wave tomography model TX-2019-Slab-S [Lu et al.,2019]

(a)

(b)

Figure 46: S-wave tomography model TX-2019-Slab-S [Lu et al.,2019]